

Bulk Metallic Glasses: Atomic Modeling and Spark Plasma Sintering Synthesis

A Thesis

Presented to
the faculty of the School of Engineering and Applied Science
University of Virginia

in partial fulfillment
of the requirements for the degree

Master of Science

by

Alexander S. Petersen

August

2015

APPROVAL SHEET

The thesis
is submitted in partial fulfillment of the requirements
for the degree of
Master of Science


AUTHOR

The thesis has been read and approved by the examining committee:

Joe Poon

Advisor

Gary Shiflet

Petra Reinke

Accepted for the School of Engineering and Applied Science:



Dean, School of Engineering and Applied Science

August
2016

Abstract:

The focus of this study was on further understanding bulk metallic glasses through the twofold path of theoretical modeling to predict elastic properties and experimental creation of large bulk metallic glass systems.

In order to accurately predict the elastic properties of bulk metallic glass systems a reliable mathematical model had to be created. Existing elastic models for crystalline systems were explored with a focus given to the Voigt and Reuss models. The method selected for further investigation was the Coherent Potential Approximation (CPA) which proved to more accurately predict the elastic moduli. Beyond this, the short and medium range order was modeled and predicted based on the efficient packing of atomic clusters, as discussed by Miracle and others. In addition to geometric cluster modeling bonding priority and atomic arrangement were considered to predict the probable locations of specific elements during the metallic glass synthesis process. Through this adjustment the CPA model was allowed to reach a coefficient of determination in excess of 0.89 on a collection of 117 select experimental bulk metallic glass systems.

The experimental creation was done on a variety of Nickel and Tungsten based systems with the goal of creating high density, highly compact, high hardness, and fairly ductile amorphous systems. This was done through optimization of amorphous system creation via synthesis of amorphous powder precursors and compaction. The sample compaction was conducted through the use of a spark plasma sintering system to ensure rapid temperature transitions, high pressure, and high compaction. The optimal path combined amorphous powders synthesized through a combination of methods including arc melting, melt spinning, annealing, and ball milling. The optimal systems created were Ni-based alloys constructed through a combination of multiple methods that retained their amorphous structure while demonstrating a hardness of 12.6 GPa, a density in excess of 11 g/cc, and ductility demonstrated through shear banding.

Table of Contents

MODELING OF AMORPHOUS METALLIC SYSTEMS	7
1.1 INTRODUCTION TO AMORPHOUS METALLIC SYSTEMS	7
1.2 EARLY MODELING OF MECHANICAL PROPERTIES.....	9
1.3 HASHIN-SHTRIKMAN BOUNDS	18
1.4 APPLICATION OF ATA MODEL	20
1.5 CPA MODEL	23
1.6 DEM MODEL	24
ATOMIC STRUCTURING.....	28
2.1 INFLUENCE OF ATOMIC STRUCTURE.....	28
2.2 CRYSTALLINE MODELING.....	29
2.3 CLUSTER MODELING.....	31
2.4 CLUSTER ATOMIC SITES	35
2.5 APPLICATION OF CLUSTER MODEL	36
2.6 <i>Modeling using cluster method</i>	43
2.7 METALLIC BONDING AND BINARY SYSTEMS	46
2.8 AMORPHOUS METALLIC ELASTIC MODULI SUMMARY.....	52
BULK METALLIC GLASSES	53
3.1 INTRODUCTION TO BULK METALLIC GLASSES	53
3.2 CREATION OF BMGS	54
3.3 COMPARISON OF BMG TO CRYSTALLINE SYSTEMS	55
3.4: CREATION TOOLS FOR BULK METALLIC GLASS SYSTEMS.....	58
3.5 SPARK PLASMA SINTERING METHODOLOGY.....	61
3.5.1 SPS TEMPERATURE	61
3.5.1.1 <i>Differential Thermal Analysis</i>	62
3.5.1.2 <i>SPS Dwell temperature</i>	62
3.5.1.3 <i>SPS Heating and Cooling rate</i>	63
3.5.1.4 <i>SPS Pressure</i>	63
3.6 SPARK PLASMA SINTERING SYNOPSIS.....	65
3.7 SPARK PLASMA SINTERING SAMPLE PREPARATION	67
3.7.1 <i>Ball Milling</i>	67
3.7.2 <i>Melt Spinning</i>	69
3.8 VICKERS HARDNESS.....	70
EXPERIMENTAL RESULTS	71
4.1 WCoB METALLIC GLASS SYSTEMS	71
4.2 NiCoTa METALLIC GLASS SYSTEMS	80
4.3 NiCoTaNb METALLIC GLASS SYSTEMS.....	86

LIST OF FIGURES

MODELING OF AMORPHOUS METALLIC SYSTEMS	7
1.1 INTRODUCTION TO AMORPHOUS METALLIC SYSTEMS.....	7
Figure 1.1-Atomic arrangements in solid material systems [3]	8
1.2 EARLY MODELING OF MECHANICAL PROPERTIES	9
Figure 1.2-Iso-strain force (left) and iso-stress force (right) applied to a system of two distinct phases.....	12
Figures 1.6- Bulk modulus for 117 experimental systems calculated using Reuss model from equations (4). 16	
1.3 HASHIN-SHTRIKMAN BOUNDS.....	18
Figure 1.7- Example system bounds: Voigt, Reuss, and Hashin-Sthrikman. H-S bounds contained within others due to constraints placed on energy deviation limit [18]	19
1.4 APPLICATION OF ATA MODEL	20
1.5 CPA MODEL	23
1.6 DEM MODEL.....	24
Figure 1.10- Shear modulus for 117 experimental systems calculated using CPA and DEM methods through equations (11,12) and (9,10) respectively.	25
Figure 1.11- Bulk modulus for 117 experimental systems calculated using CPA and DEM methods through equations (11,12) and (9,10) respectively.	26
ATOMIC STRUCTURING.....	28
2.1 INFLUENCE OF ATOMIC STRUCTURE	28
2.2 CRYSTALLINE MODELING	29
2.3 CLUSTER MODELING	31
Figure 2.1- Miracle Model coordination number and atomic structure based on radii ratio [41]	34
2.4 CLUSTER ATOMIC SITES	35
Figure 2.2- 2-D and 3-D representations of atomic ordering in Miracle cluster model with pink being Ω , blue being α , purple being β , and orange being γ [40]	35
2.5 APPLICATION OF CLUSTER MODEL	36
Figure 2.3- Atomic fraction of solute versus solvent. Demonstration of solute rich versus lean and cluster formation [41]	38
Figures 2.4 and 2.5- Heat of formation of the demonstrated binary systems in kJ/mol for Zirconium and Calcium binaries respectively.	40
Figures 2.6 and 2.7- Heat of formation of the demonstrated binary systems in kJ/mol for Iron and Magnesium binaries respectively.	41
Figure 2.8- Heat of formation of the demonstrated binary systems in kJ/mol for Lanthanum binaries.	42
2.6 Modeling using cluster method.....	43
2.7 METALLIC BONDING AND BINARY SYSTEMS.....	46
Figures 2.11 and 2.12- Delta plots with experimental data as blue points. Lines are best fit curves to predict properties of binary based on atomic ratio of elements present.....	48
Figures 2.13 and 2.14: Bulk and Shear moduli predictions of ternary composition WTaB through the use of M_{ab} model.	50
Figures 2.15-2.18: M_{ab} plots for WB and TaB binary shear and bulk moduli.....	51
2.8 AMORPHOUS METALLIC ELASTIC MODULI SUMMARY	52
BULK METALLIC GLASSES	53
3.1 INTRODUCTION TO BULK METALLIC GLASSES	53
3.2 CREATION OF BMGS.....	54

Figure 3.1- Representation of Glass and Crystallization regions with respect to temperature and time. Path 1 demonstrates rapid quenching while Path 2 represents powder metallurgy.	55
3.3 COMPARISON OF BMG TO CRYSTALLINE SYSTEMS.....	55
Figure 3.2- Comparison of Tensile strength and Young's modulus for BMG and crystalline metals [8].....	56
Figure 3.3- Demonstration of wear resistance and deformation on gear teeth comparing metallic glasses to steels [8].....	57
3.4: CREATION TOOLS FOR BULK METALLIC GLASS SYSTEMS.....	58
Figure 3.4- Current pathway under Spark Plasma Sintering compaction [46].....	59
Figure 3.5- Thermal Technologies SPS 10-4 device. Hydraulic and Vacuum pumps are located behind the device.	60
3.5 SPARK PLASMA SINTERING METHODOLOGY.....	61
Figure 3.8- Demonstration of temperature and pressure as a function of time during Spark Plasma Sintering system compaction [45].....	61
3.5.1 SPS TEMPERATURE.....	61
3.5.1.1 Differential Thermal Analysis.....	62
3.5.2 SPS Dwell temperature.....	62
3.5.3 SPS Heating and Cooling rate.....	63
3.5.4 SPS Pressure.....	63
Figure 3.9-Compaction density as a function of pressure and particle size for ZrO_2 in SPS[44].....	64
3.6 SPARK PLASMA SINTERING SYNOPSIS.....	65
Figure 3.10- Compressive stress versus strain for $Zr_{55}Cu_{30}Al_{10}Ni_5$ demonstrating importance of high compaction and low porosity in BMG creation [47].....	66
3.7 SPARK PLASMA SINTERING SAMPLE PREPARATION.....	67
3.7.1 Ball Milling.....	67
Figure 3.11- Ball mill vial rotation diagram[49].....	68
3.7.2 Melt Spinning.....	69
Figure 3.12- Melt Spinner system for creation of amorphous metallic ribbons.....	70
3.8 VICKERS HARDNESS.....	70
EXPERIMENTAL RESULTS.....	71
4.1 WCoB METALLIC GLASS SYSTEMS.....	71
Figure 4.1- Phase diagram of Fe-B binary [50].....	72
Figure 4.2- X-Ray Diffraction diagram of W-based ball milled systems.....	73
Figure 4.3- Iron contamination during ball milling for W-based systems.....	75
Figure 4.4- Differential Thermal Analysis on $W_{40}Co_{30}B_{30}$ base system post milling.	76
Figure 4.5-DTA results for W-systems showing T_x decrease due to Fe contamination.....	76
Figure 4.6- $W_{19}Co_{13}B_{13}Fe_{48}Cr_7$ SPS disk images using optical microscope.....	79
4.2 NiCoTa METALLIC GLASS SYSTEMS.....	80
Figure 4.7- X-ray diffraction on select NiCoTa based systems milled for 15 hours.....	80
Figure 4.8- X-ray diffraction on $Ni_{45}Co_{20}Ta_{35}$ ball milled systems at various times.....	81
Figure 4.9- Demonstration of typical melt spun ribbons, shown is $Ni_{45}Co_{10}Ta_{25}Nb_{20}$	82
Figure 4.10- Optical image of $Ni_{45}Co_{20}Ta_{35}$ SPS disk created via milled melt spun ribbon. Red lines demonstrate porous regions.....	84
Figure 4.11- X-ray diffraction of $Ni_{45}Co_{20}Ta_{35}$ ribbons at various anneal times and temperatures.....	85
Figure 4.12-X-ray diffraction of $Ni_{45}Co_{20}Ta_{35}$ ribbons and disks once SPSed.....	86
4.3 NiCoTaNb METALLIC GLASS SYSTEMS.....	86
Figure 4.13- DTA results on $Ni_{45}Co_{10}Ta_{25}Nb_{20}$ ribbons.....	87
Figure 4.14- SEM imaging of ball milled NiCoTaNb ribbons.....	88
Figure 4.15- X-ray diffraction of $Ni_{45}Co_{10}Ta_{25}Nb_{20}$ SPS disks made using milled ribbons.....	89

Figure 4.16 (above)- SPS 43 optical image of polished surface	90
Figure 4.17 (below)- SPS 44 optical image of polished surface	90
Figure 4.18 (above)- SPS 43 optical image of polished surface	91
Figure 4.19 (below)- SPS 44 optical image of polished surface	91
Figure 4.20- Optical images of SPS 102 exhibiting nearly perfect compaction. Note: small "pore" on the right is a microscope lens scratch.	93
Figure 4.21- X-ray diffraction compilation of $\text{Ni}_{45}\text{Co}_{10}\text{Ta}_{25}\text{Nb}_{20}$ systems under distinct creation methods.	95
Impact of particle size demonstrated in SPS 101, 102, 106 and 131 due to crystallization.	95
Figure 4.22 (above)- SPS 134 optical image of polished surface	96
Figure 4.23 (below)- SPS 145 optical image of polished surface	96
Figure 4.24 (above)- SPS 134 optical image of polished surface	97
Figure 4.25 (below)- SPS 145 optical image of polished surface	97
Figure 4.26-XRD on $\text{Ni}_{45}\text{Co}_{10}\text{Ta}_{25}\text{Nb}_{20}$ powders sintered at 575C for 10 minutes.	99
Figure 4.27-Percent relative densities of $\text{Ni}_{45}\text{Co}_{10}\text{Ta}_{25}\text{Nb}_{20}$ spark plasma sintered systems for iso-pressure and iso-ratio configurations	100

LIST OF TABLES

MODELING OF AMORPHOUS METALLIC SYSTEMS	7
Table 1.1- R^2 correlation using select mathematical model on BMG systems shown in appendix [1]......	27
ATOMIC STRUCTURING.....	28
Table 2.1- Elastic Moduli Accuracy of 17 Crystalline Metallic Systems.....	30
Table 2.2- Coordination numbers (N) and the corresponding radii ratio RN^* , reproduced from Miracle [#10].....	32
Table 2.3- Elastic Moduli Accuracy using Cluster Style Modeling	44
EXPERIMENTAL RESULTS	71
Table 4.1- Experimental parameters of SPS creation of BMG Tungsten Alloys	77
Table 4.2- Experimental and Theoretical properties of BMG Tungsten Alloys created through SPS compaction.....	78
Table 4.3- Experimental results for early SPS BMG Alloys	83
Table 4.4- Select $Ni_{45}Co_{10}Ta_{25}Nb_{20}$ SPS procedures and experimental results .	98

Chapter 1

Modeling of Amorphous Metallic Systems

1.1 Introduction to amorphous metallic systems

The amorphous structure of a metallic system is best considered as a hybrid between two of the fundamental states of matter: liquid and solid. Typical crystalline solids can be thought of as rigid, non-moving structures that consist of a regular, repetitive geometric lattice. In a perfectly formed crystalline solid the lattice can be broken into a unit cell that, when repeated, can describe the position of each atom present in the system. This can be considered as long-range order as the position of each atom can be considered as influenced by other atoms or structures present in the system. A liquid has no defined shape and can flow to fit the shape of its container, with the long-range order greatly diminished. The atoms have no defined location or pattern within a liquid, though they still retain the short-range order also found in solids that consists of atomic bonding and interaction on the much smaller scale.

It is between these two states of matter that amorphous metals may be found as they are solid in that they resist shear motion and remain rigid but resemble a liquid in their structure as they only possess short-range order. Amorphous metallic systems were first discovered in 1960 through the creation of a Au-Si alloy quenched at a rate of over 10^6 K/sec [1]. This rapid solidification created a system called a metallic glass (MG) in which the atomic structure of the liquid was preserved yielding a class of alloys with short and medium range order but a lack of any defined long range structuring [2]. As demonstrated by the rapid temperature drop called critical cooling rate it was initially difficult to freeze the atoms in their disordered state. From the energetic view of the system if the cooling rate used is quick enough the atoms become locked into their disordered liquid positions and lack the energy necessary to reorganize into the more repetitive crystalline lattice structure. If the cooling rate is too slow small regions of the system may have the time and energy to form local regions with a crystalline pattern as shown in Figure 1.1. This structure is known as a polycrystalline system shown in the

center of the figure and if the cooling rate is far too slow even a single crystal state can be created as shown on the left. The crystalline structure is the most stable low energy structure for this particular solid as all the atoms fall into repetitive, organized patterns in which the location of a single atom can predict and determine the location of its adjacent atoms. In the polycrystalline state there are localized regions of an organized lattice, but the regions themselves do not fit together into long-range ordering. This can be considered as medium-range ordering for nano-scale systems as the short-range order is determining the neighboring atoms but long-range ordering is not fully present. Within the few nanometer regime there is limited repetition of the atomic bonding but there is no repeatable pattern describing the arrangement applicable to the system as a whole. The ideal amorphous structure on the right is purely disordered with no repetitive pattern present and only the interatomic bonding (short range order) playing a defining role in atom locations.

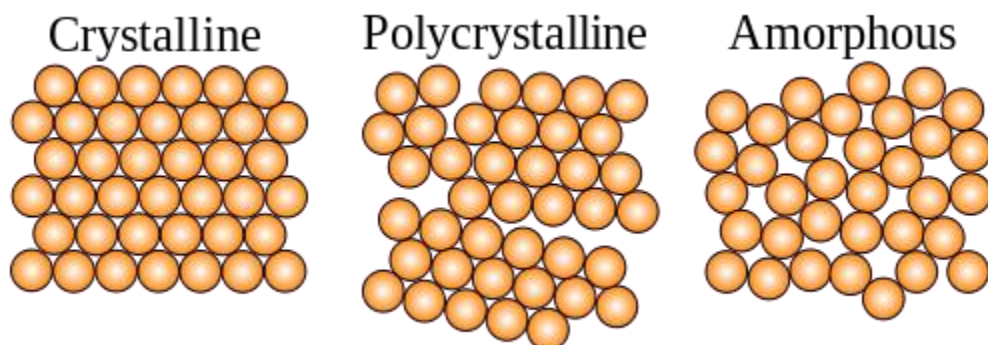


Figure 1.1-Atomic arrangements in solid material systems [3]

When considering metallic systems it is often important to consider the atomic arrangement of the elements present to fully understand the material. This involves the understanding of the metallic and directional bonding as well as the lattice structure of the atoms present, requiring careful procedures in system creation to avoid disorder or multiple phases from forming. With this in mind in 1960 Klement, Willens, and Duwez [1] at Caltech produced the first metallic glass alloy consisting of $\text{Au}_{75}\text{Si}_{25}$ cooled at an extremely fast rate (over 1,000,000 K/s) in order to prevent the atoms from crystallizing and forming a single uniform crystalline phase. This extremely high critical cooling rate, and the cooling rate of most other amorphous metallic systems found in the first few

decades forced the systems to be created in small and thin amounts, usually in the forms of foils, ribbons, films, and wires. This sparked a search for new compositions that could be made with a much lower critical rate, in addition to new methods of sample creation to allow for faster heat dissipation. Since then many new systems have been found with much lower critical cooling rates that enabled much larger samples to be created, some in excess of 1 millimeter in diameter or depth. These new systems are referred to as Bulk Metallic Glasses (BMG), and are a subject of research for creating even larger samples and their applications in multiple scientific fields[4-7].

The primary focus for creating and maintaining the amorphous metallic glass structure lies in the ability to create systems with varying mechanical properties. Exploiting the glass like structure it is possible to create alloys that have higher tensile strength, high elastic strain limits, and fracture toughness when compared to crystalline materials [8]. Amorphous structures also allow certain systems to have higher wear and corrosion resistance [8,9]. It is the exploitation of these structural properties that is a driving force for BMG creation and study over typical crystalline metallic alloys.

1.2 Early modeling of mechanical properties

When designing metallic alloys to meet specific mechanical or chemical properties modeling numerous metallic systems is often a reasonable way to select both initial compositions and to make modifications to existing systems. Due to the disordered structure of metallic glasses the field of modeling has experienced difficulty in predicting the mechanical properties of the systems. As many of the metallic glass systems have a high solvent-solute ratio the solute atoms are often isolated within the system. Due to this isolation it was suggested by Ma *et al.* that the dominance of the solvent atom could be used to determine the elastic moduli values of the metallic glass as a whole [10]. In order to fully understand metallic glasses the elastic moduli, specifically Young's modulus is sought. Elastic moduli are material properties that do not take into account the dimensions of the system and are representative of how the material withstands stress and strain. Young's modulus specifically describes the ratio of stress to strain during which the system deforms elastically and is of high interest when exploring metallic glasses. In an effort to predict the Young's modulus, this solvent-solvent model

was applied on a select set of 24 bulk metallic glasses consisting of both RE and transition metal solvent atoms. The model demonstrated a mean ratio of metallic glass/solvent Young's modulus of 0.97 with a standard deviation of 0.07 and ratio of 0.96 with a standard deviation of 0.07 for the Bulk modulus [10]. The results of this model serve as a stepping stone for further investigation into the impact of solute atoms to the elastic moduli of the material as a system due to the preferential selection of metallic glasses used to demonstrate the model. This must be taken with a caveat however, as the selected systems were often solvent dominant. As explored later in this work metallic glasses mechanical properties vary dramatically with minor compositional changes even when the solvent atomic percentage remains constant.

To create a more refined model the next step undertaken was to understand the potential influence of the solute-solvent and solute-solute interactions to the system on a long range scale. When investigating Pd-Ni-P BMG systems the elastic moduli of the glass as a whole was found to be a rough average of the constituent elements [11]. This sparked interest in consideration of the metallic glass systems as a composition of elements analogous to a combination of two or more distinct crystalline materials in a composite. The reason for this application to metallic glasses was in the local short range order exhibiting similar properties to the atomic configurations of the metallic components [11]. Elastic moduli of elements and compositions can be predicted and accurately modeled using the energy present in the atomic bonding. If the short range order in an amorphous system exhibited similar bonding (and by consequence elastic moduli) to their pure metallic and crystalline alternate phases potential crossover of mechanical properties becomes a possibility. If the atoms present in the amorphous configuration demonstrate similar bonding to a pure element crystalline phase they would then demonstrate the elastic moduli of that specific structure. This implies that the elemental elastic moduli could potentially serve to predict the properties of the system as a whole due to the presence of predictable short and medium range order despite the lack of long range order [11].

To represent the combination of the elements in the metallic glass system the method suggested by Wang *et al.* was in the use of the rule of mixtures (as explored later

in this work) [11-13]. While this method is typically only applied to composite based systems it was suggested that in the metallic glass configuration it was possible to model each element as though it was acting as a unique and distinct composite material. The use of the rule of mixtures consisting of only the elemental values was not without fault as metallic glasses exhibited a wide range of elastic properties for only minor changes in composition. This is often corrected for in additional terms present in the equations for the rule of mixtures beyond volume ratios of the constituent systems. Beyond this, rare earth metallic glasses such as $\text{Ce}_{70}\text{Al}_{10}\text{Ni}_{10}\text{Cu}_{10}$ exhibited far lower Young's and Bulk moduli than were predicted using the rule of mixtures as they often exhibited moduli below the value of any involved element. This is believed to be due to the glass like structure even on the short range order scale allowing for ease with which the system exhibits viscous like behavior [11].

To properly model the mechanical properties of metallic systems it is essential to know both the mechanical properties of all the individual elements, as well as how they interact as alloys. Once combined into composite compounds, the systems often have properties that do not resemble the individual elements or systems. The focus of the modeling in this work has primarily been in exploring the mechanical properties of metallic alloys with a high focus on shear and bulk moduli. Using these moduli it is possible to calculate Young's modulus, E , of the metallic glass and through that it is often possible to predict the tensile fracture strength σ_{fracture} ($E/\sigma_{\text{fracture}} \approx 50$) and hardness value H_v ($E/H_v \approx 20$). In addition, it is also possible to predict the relationship between shear stress at yielding (τ_y) and the shear modulus (G) as $\tau_y = \gamma_c G$ where $\gamma_c = 0.0268$ [13, 14].

In an effort to begin modeling from the very basics the first model used was the rule of mixtures. The rule of mixtures seeks to combine the mechanical properties of the elements present in a system based on their ratios, without any additional assumptions made. Through this method the properties of the base elements, such as the shear modulus, were combined to simulate the properties of the combined alloy. The system can be considered using two cases, or bounds, with the upper bound being called the Voigt model [15] and the lower bound being referred to as Reuss model [16]. This upper bound can be created using the model shown in equations 1 and 2:

$$G = \sum_i \phi_i \cdot G_i^a \quad (1)$$

$$K = \sum_i \phi_i \cdot K_i^a \quad (2)$$

where G and K are the shear and bulk modulus respectively, a is a set constant (typically set to 1), and ϕ is the volume fraction of each element. This model uses the basic mechanical properties of the elements involved to predict the properties of the system created. In the case of the Voigt average the system can be considered to be under a uniform strain. This iso-strain model can be considered as each element (or atom) in the system being subject to the same force. To obtain the properties of the system as a whole it is possible to think of the compression in terms of springs. For the Voigt average the system can be thought of as a set of springs in parallel where in order to compress the system the force required must exceed the requirements of the strongest element before buckling. This is shown on the left side of Figure 1.2 where each element must yield before the full system collapses. Another perspective is shown in the right side of Figure 1.2 where the system is subject to iso-stress. This can be considered similar to a system of springs in series where the weakest spring determines when compression occurs.

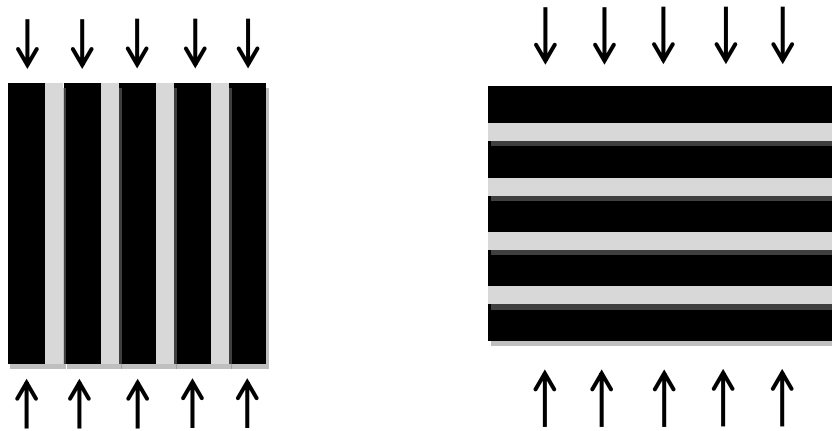


Figure 1.2-Iso-strain force (left) and iso-stress force (right) applied to a system of two distinct phases

When considered as a set of springs arranged in either parallel or series it is possible to consider which is most applicable to each elastic property. The bulk modulus is a measurement of what force is required to compress the system from all directions,

resulting in a compression of all elements present. This could be considered a combination of springs in both parallel and series as depending on the arrangement of phases and the structure of the system both styles may exist. In this manner it is how to combine the two views that makes the bulk modulus challenging to model. As for the shear modulus it is a measurement of the force required to cause displacement in a single direction. This can be considered most similar to a set of springs in series as movement begins as soon as any of the springs begins to yield. As the atomic system has a force being applied in an iso-stress method each of the elements experiences the same force, but it only takes one phase or system yielding to cause the whole system to effectively move.

To more accurately model the iso-stress method a value of $a=-1$ was selected by Reuss [16] creating a reciprocal sum to combine the elemental values. This was referred to as either the Reuss method or the reciprocal sum approach (RSA) and altered the way in which the elemental values for the elastic moduli influenced the system as a whole. This model is shown in equations #3 and 4, and through these extreme situations (selection of a as 1 or -1) to obtain a rough estimation for the extreme boundaries of the shear and bulk moduli of the metallic systems. In this way the Voigt model prioritizes the strongest elements with the highest moduli while the Reuss model prioritizes the weakest. In an effort to combine the two extremes a third model was created, called the Voigt-Reuss-Hill method which simply averages the two models directly to get a rough idea for modeling the actual elastic properties by averaging the extreme boundaries.

$$\frac{1}{G} = \sum_i \frac{\phi_i}{G_i} \quad (3)$$

$$\frac{1}{K} = \sum_i \frac{\phi_i}{K_i} \quad (4)$$

In order to gauge the effectiveness of the models for mechanical properties a selection of 117 different metallic glass compositions was selected and the model was applied to those systems (chart of systems in appendix 1) [10-13]. This large arrangement of metallic glass compositions was selected to account for inaccuracies

created where specific compositions may be accurately modeled but overall the model was inaccurate. The model's accuracy was determined by the R^2 value (coefficient of determination) determined by comparing the calculated results to the experimental values obtained using equation #5.

$$R^2 = 1 - \sqrt{\frac{\sum \frac{(Exp-Calc)^2}{Exp^2}}{Number\ of\ Systems}} \quad (5)$$

To begin, the Voigt model was used on the metallic glass systems with volume fraction for ϕ_i and elemental shear and bulk values for G_i and K_i respectively. For this first model the $R^2=0.773$ for Shear and $R^2=0.833$ for Bulk, with Figures 1.3 and 1.4 showing the experimental data obtained for those systems compared to the predicted properties. The line labeled "Calc=Exp Ref." is for reference and demonstrates the desired 1:1 correlation for calculated to experimental results. The R^2 values are mathematically determined through comparison of each system to the line representing perfect correlation. This line is carried forward for each model employed serving the same function. Volume fraction was used as the fraction ratio as stress and strain are determined by the force applied to each component, which is a function of the area or volume occupied. Following this the Reuss model was used on the same collection of systems and is shown in Figures 1.5 and 1.6 with R^2 values were 0.889 for shear and 0.853 for bulk. Given this accuracy, the model showed potential promise for modeling the moduli of the compositions if proper assumptions and modifications are made.

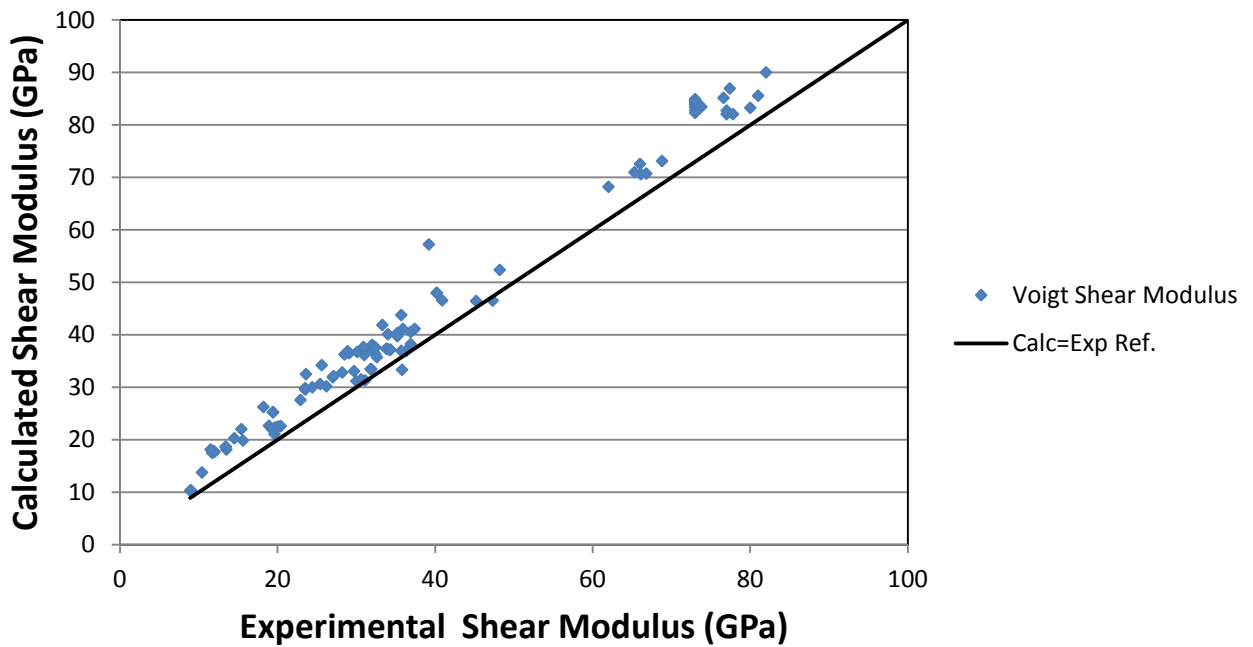


Figure 1.3-Shear modulus calculated using the Voigt model from equation (1) for the 117 experimental systems.

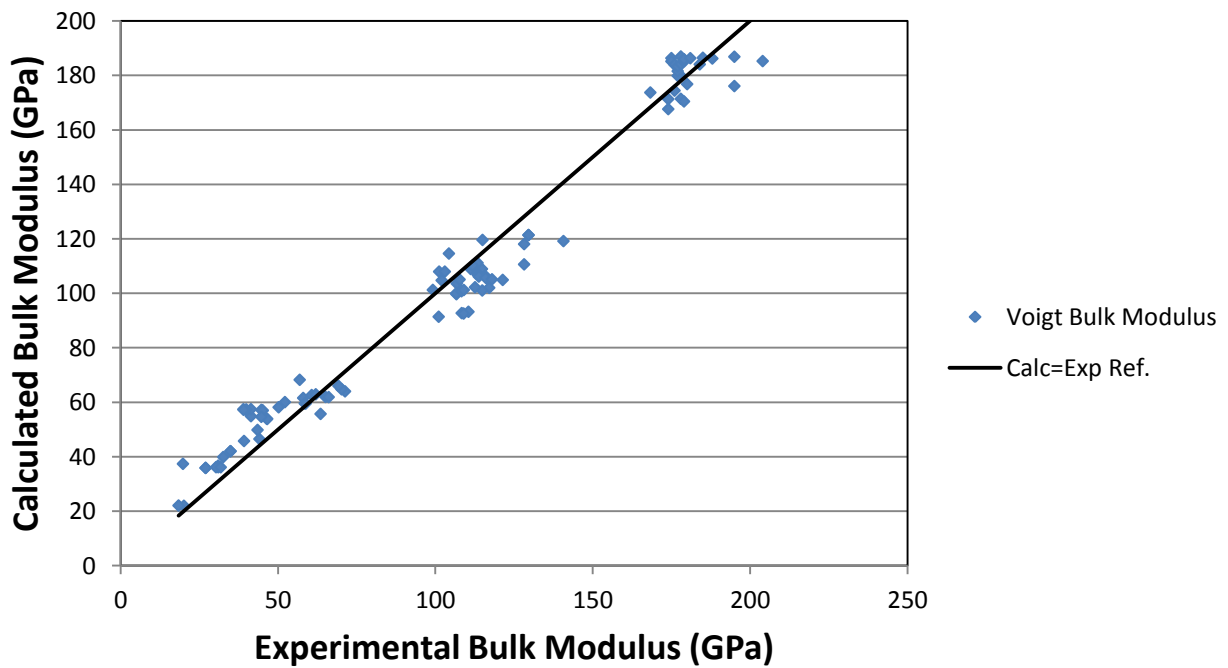


Figure 1.4-Bulk modulus calculated using the Voigt model from equation (2) for the 117 experimental systems.

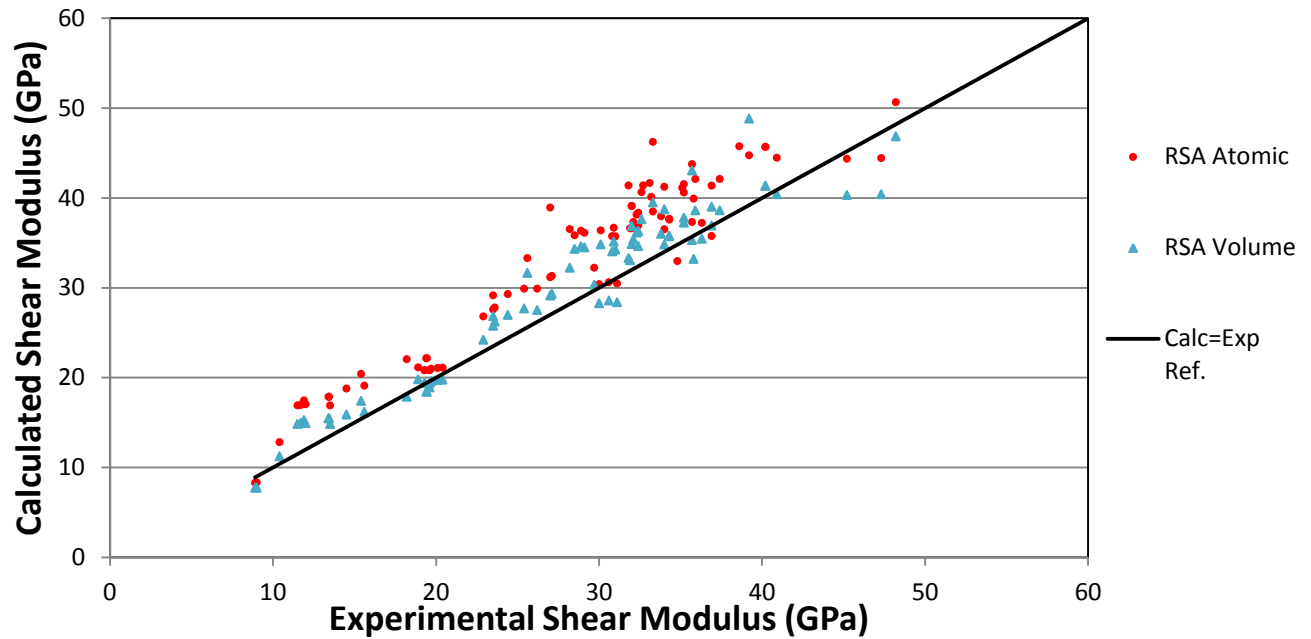
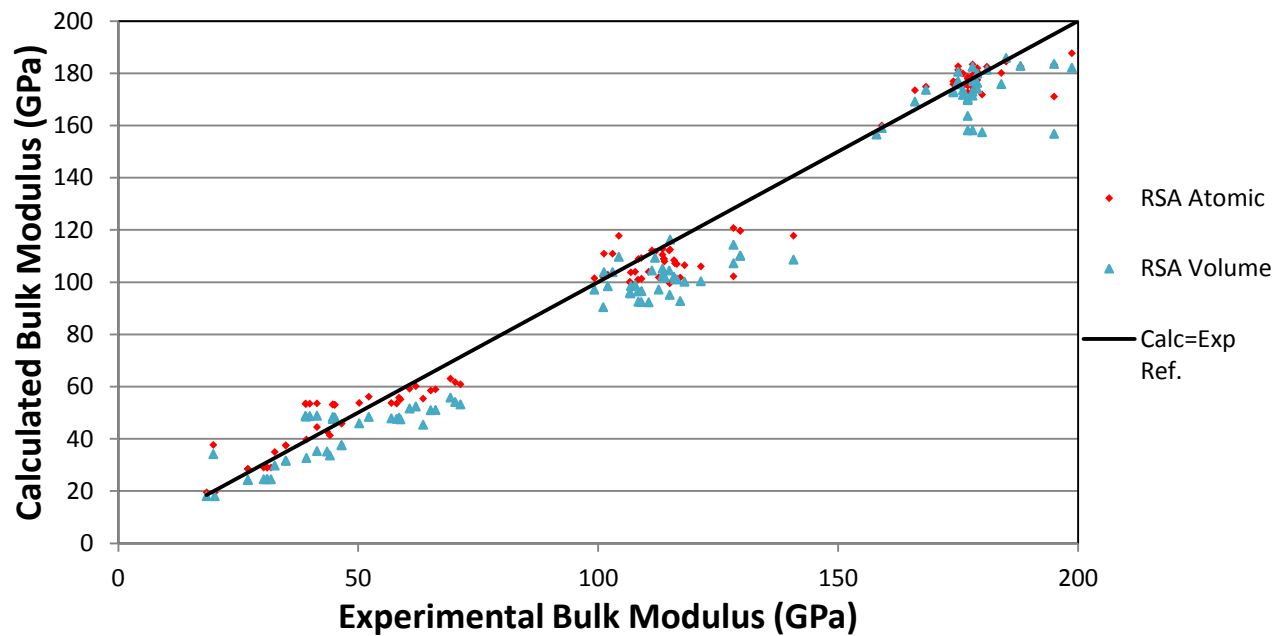


Figure 1.5- Shear modulus for 117 experimental systems calculated using Reuss model from equation (3).



Figures 1.6- Bulk modulus for 117 experimental systems calculated using Reuss model from equations (4).

These models serve as a crude approach to modeling of metallic glass systems, but provide a rough baseline to compare to for later models. Given the higher accuracy of the Reuss model when compared to the Voigt model it was selected as the baseline model against which all future models would be compared. To refine the methods the RSA was broken down into two different categories, volume and atomic, based on which atomic fraction ratio was used to calculate the moduli of the system. This was done as a method of determining if the volume of the elements present in the system or the number of atomic bonds was a more dominant force in modeling elastic moduli. While atomic fraction is simple to use as it is simply the atomic ratio of elements present in the system, the volume fraction in this model is determined by the volume of each element as a fraction of the whole and was calculated using equation 5:

$$\phi_i^{Vol} = \frac{\phi_i \cdot V_i}{\sum_i V_i \cdot \phi_i} \quad (5)$$

where ϕ_i is the atomic fraction, V_i is the volume per atom, and ϕ_i^{Vol} is the volume fraction of that element. Using the volume for each element (determined by the atomic radius of each element in a metallic bond), and the atomic ratio in the composition, it is possible to calculate the volume fraction percent that each element contributes. It is important to note that the Reuss and Voigt models both were constructed with only volume fraction in mind as elastic properties are based on the distribution of force throughout the system, which is based on the area presented. In this manner the volume fraction is the most apt way of determining the distribution of pressure over the system as a whole, and is used in nearly every model of elastic moduli since the model's creation. With this in mind the atomic and volume fraction ratios were carried forward with the volume fraction being used in each model and the atomic fraction only being used in the RSA model to determine if atomic fractions could be used as a more accurate representation of the elastic properties in amorphous systems. While there is no absolute reason that the atomic fraction is incorrect the elastic properties of systems are based on the force applied to an area, which is more directly related to the volume occupied encouraging the use of volume fractions. At this point it was desired to increase the accuracy of the elastic moduli models, but the iso-stress versus iso-strain question was still unresolved when dealing with the shear and bulk moduli modeling. Further

investigations were performed into how to combine the two models to better account for the distribution of force throughout the amorphous structure.

1.3 Hashin-Shtrikman bounds

Beyond the Reuss and Voigt bounds it is possible to create a more refined window for the elastic moduli of a system to better account for the iso-stress versus iso-strain models of force in the metallic system. The Hashin-Shtrikman method developed in 1962 and 1963 works on the idea that the system has no locations in which the system undergoes either iso-strain or iso-stress but is more a combination of the two. Through this approach the extreme cases of Reuss (uniform stress on all phases) and Voigt (uniform strain on all phases) are treated as extreme overestimates of the actual system. To create a more realistic model Hashin and Strikman determined the bounds by limiting the elastic energy deviations that can occur from a specific isotropic state [17]. This is done by using the volume fractions of the elements present in the system and combining the possible phases formed using equations #6 and 7 where the modulus of the host element, denoted by subscript H as G_H or K_H , is adjusted by the addition of other elements:

$$G_{net} = G_H + \frac{\phi_{i+H}}{(G_i - G_H)^{-1} + 2 \cdot (1 - \phi_{i+H}) \cdot \frac{(K_H + 2G_H)}{5G_H(K_H + \frac{4}{3}G_H)}} \quad (6)$$

$$K_{net} = K_H + \frac{1 - \phi_{i+H}}{(K_i - K_H)^{-1} + \frac{\phi_{i+H}}{(K_H + \frac{4}{3}G_H)}} \quad (7)$$

The extreme upper and lower bounds of the Hashin-Shtrikman system are created when the host and additional elements act in reversed roles. In this case the extremes are still rather pronounced, rendering them unable to exactly predict the properties of the systems under investigation. However, they are often more refined when compared to the Voigt and Reuss methods, as shown in Figure 1.7. The main focus of the Hashin-Shtrikman bounds was to show the constriction or relaxation of potential range of the data obtainable with the upper and lower extremes. Given the potential influence of the atomic structuring on the properties of the system as a whole by simply viewing the

system as a combination of elemental values taken to extremes little improvement is gained when compared to the Voigt and Reuss models.

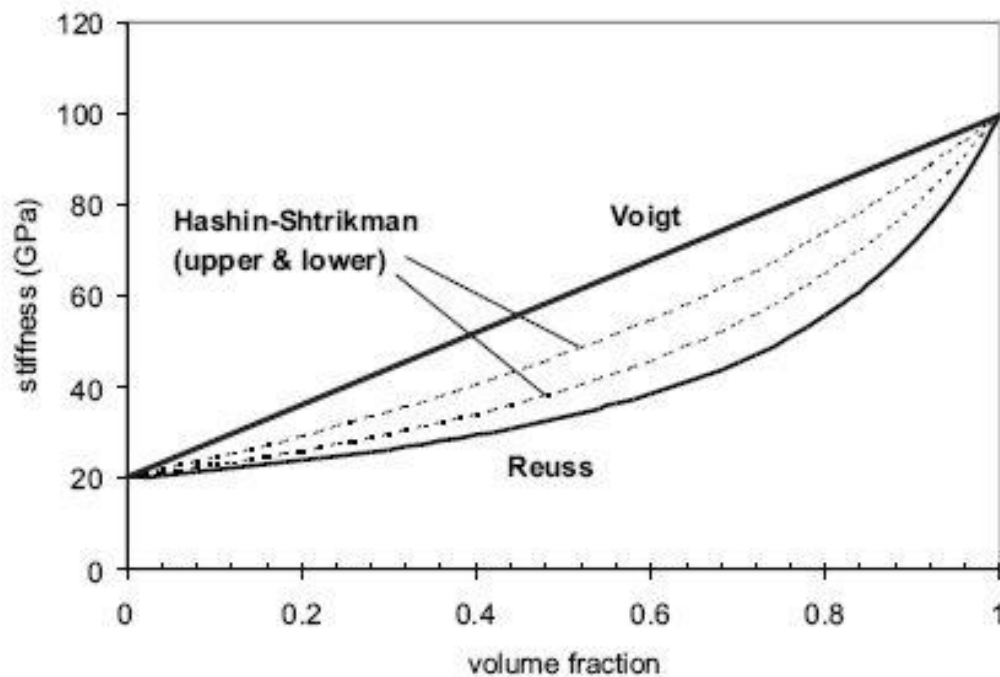


Figure 1.7- Example system bounds: Voigt, Reuss, and Hashin-Shtrikman. H-S bounds contained within others due to constraints placed on energy deviation limit [18]

The effort to constrain the amorphous metallic glass systems within the Hashin-Shtrikman bounds to a more accurate model proved to be a difficult task as the order of elemental addition had a dramatic impact on the upper and lower bounds. As many of the amorphous systems have a well defined host element filling roughly 40-60% atomic fraction the additional elements were far less defined in the order in which they should be included. Depending on the order in which the elements were added the upper and lower bounds of the Hashin-Shtrikman model often ended up nearly the same values as the Voigt and Reuss models for amorphous systems, raising the question of how applicable with method would be without a defined method of selecting the elemental order. The R^2 value obtained for the Hashin-Shtrikman method was 0.553, though the result could be dramatically increased or decreased if elemental additions were altered in the order in which they were applied.

1.4 Application of ATA model

While the RSA method was acceptable for loose fits of shear and bulk moduli in order to predict and model individual systems a more refined model had to be created. The first step in this direction was using the average T-Matrix approximation (ATA) based on the initial work of J. Korringa [19] and J. Beeby[20] modeling the electronic structure of systems followed by K. Watson [21] and later J. Berryman [22] moving on to elastic properties. In order to find the Green function of the effective medium or system the total scattering matrix or T-matrix must be found. In this model the T-matrix is taken as the total average and substituted back into the Green's function of the system to find the effective values. This average T-matrix approximation method is based on modeling the single-scattering in systems consisting of spherical components. In this method the model predicts how the single waves traveling through the system of spheres will alter the state of the system as a whole, determining its elastic properties. Using this concept, Berryman et al. adjusted the simply electronic model to predict how elements or compositions would react to the inclusion of additional elements. In order to model anything beyond the most basic system the ATA model has to make several assumptions in order to properly model more complex systems containing multiple elements. The ATA model must select one element as the host with the other elements as the inclusion elements. In addition, the composition must have constituents with sufficiently split shear and bulk moduli before a reasonable value can be obtained. If the components have moduli values within ~5-10% variation the mathematical ATA model will not take into account the properties of the additional constituents and simply return a result strongly biased by the host element. Beyond this, the selection of which element acts as the host of the composition alters the end results, even when the elements are maintained in the same volume fractions. In the extreme cases where the element with the highest shear modulus is selected as the host the bulk modulus calculated is the Hashin-Shtrikman lower bound and the upper bound when the lowers shear modulus is selected as host. This shows how the ATA method, with the numerous assumptions made about elemental structure and elemental values, can result in the same values as the Hashin-Shtrikman

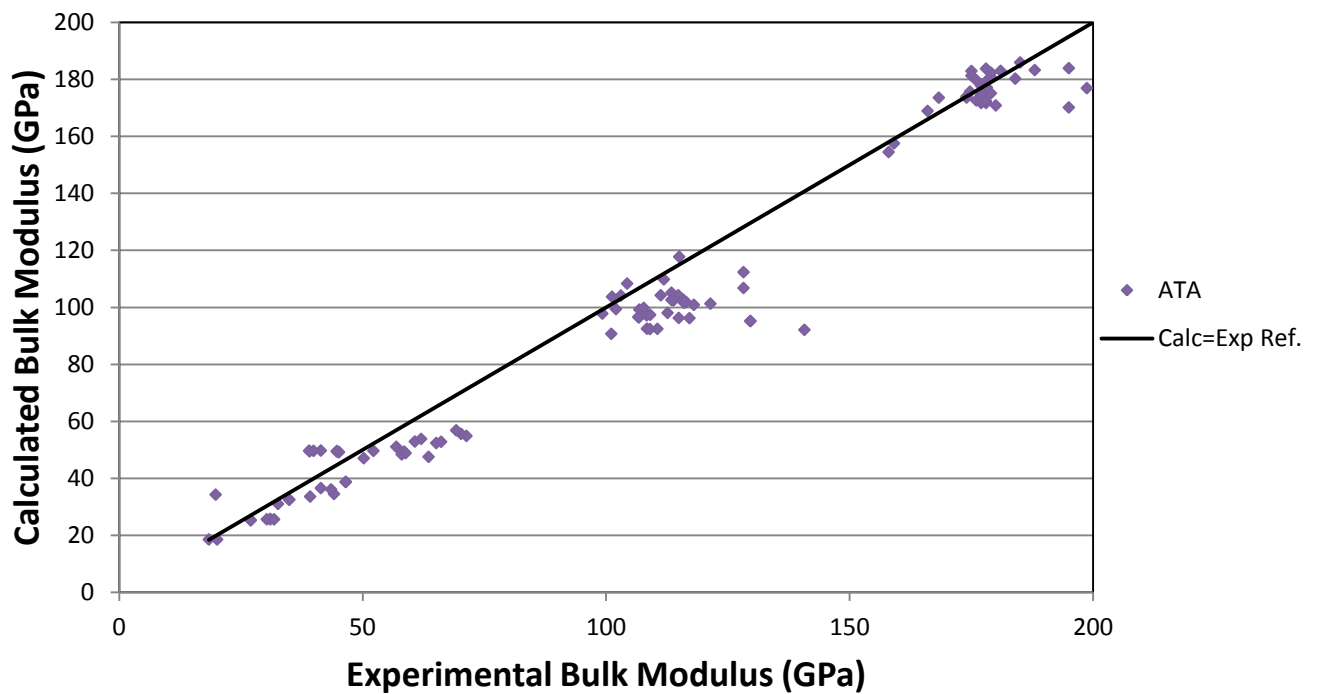
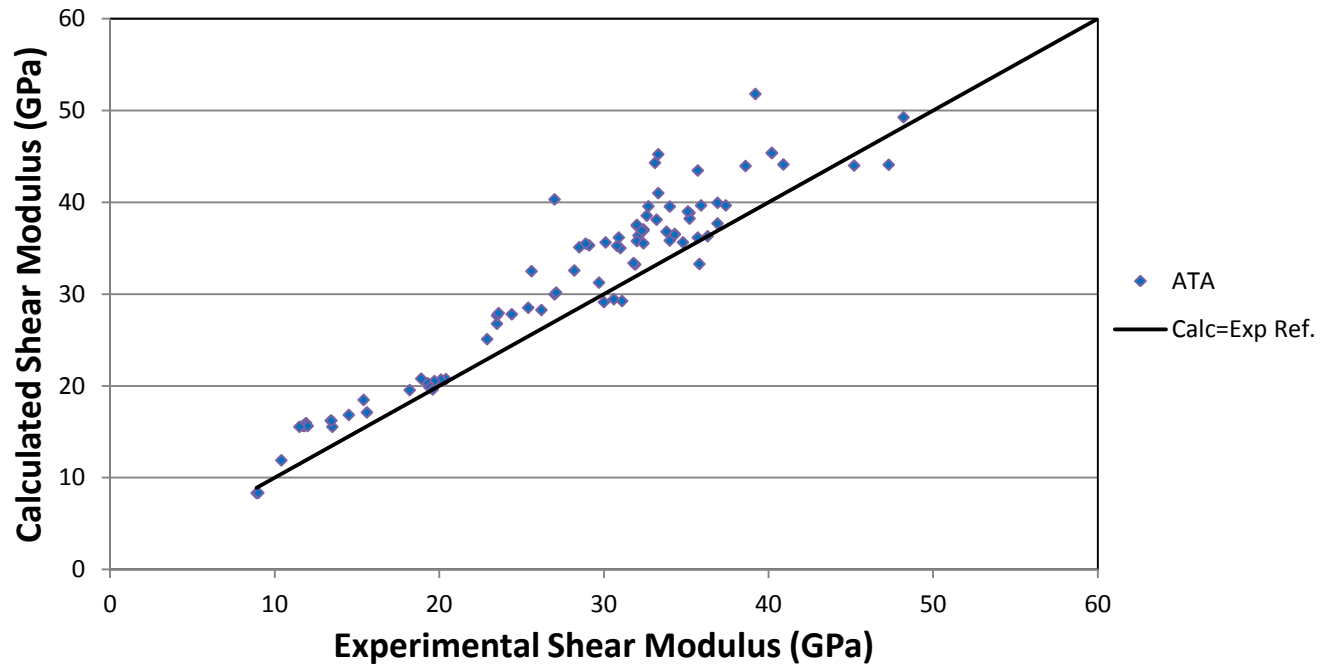
bounds. With this in mind the ATA model enables elastic properties to be modeled in a more refined manner compared to the Voigt or Reuss models which are simply additions of the elements present. These assumptions result in the model demonstrated through equations #8-10 to calculate the shear and bulk modulus of the composition where equation (#8) was a substitution made for ease of display:

$$X = \frac{G \cdot (9K + 8G)}{6 \cdot (K + 2G)} \quad (8)$$

$$G = G_H + \frac{\sum_i \phi_i \cdot (G_i - G_H) \cdot \frac{(G_H + X)}{(G_i + X)}}{1 - \sum_i \phi_i \cdot \frac{(1 - (G_H + X))}{(G_i + X)}} \quad (9)$$

$$K = K_H + \frac{\sum_i \phi_i \cdot (K_i - K_H) \cdot \frac{(K_H + X)}{(K_i + X)}}{1 - \sum_i \phi_i \cdot \frac{(1 - (K_H + X))}{(K_i + X)}} \quad (10)$$

To calculate the results of these equations the mathematical models were input in MATLAB using import features from Microsoft Excel. This enabled the rapid computation of the elastic properties of all 117 systems to occur rapidly and in tandem. This ATA model can be used for any composition of elements, allowing it the same capabilities as the RSA model with a similar degree of accuracy, $R^2=0.848$ for Shear and $R^2=0.867$ for Bulk. The data for the 117 systems is shown in Figures 1.8 and 1.9. The comparable accuracy of the ATA model to the RSA model rendered this model as insufficient for proper modeling of mechanical properties, but showed the potential to use alternative methods to predict the properties of systems.



Figures 1.8 and 1.9- ATA model of shear and bulk moduli for 117 experimental systems.

1.5 CPA model

Once established, the ATA model could be modified to provide a more accurate model of the shear and bulk moduli. In the ATA model the Green function was found through the use of averaged T-matrices while the coherent potential approximation (CPA) model relies on a different method of determining the T-matrix. This is done through determining the Green function self-consistently, requiring that the $\langle T \rangle$ be equal to zero implying that the Green function yields $\bar{G} = \langle G \rangle$. The comparison between the average T-matrix and declaration of a net zero T-matrix is further shown in the work of Kumar and Baskaran [23]. This self-consistent Green function enables the removal of several approximations made to calculate the ATA model, primarily the declaration of a host element. This is due to the idea of an effective medium in place of a pure host, as the system is described through its overall properties in place of treatment of the system as a split between host and the inclusions. Further use of the Berryman work [22] was used to create this approximation model, forcing both the bulk and shear moduli to be calculated in tandem. This coupling makes for a more complex calculation method that must be solved through iteration, which renders it difficult to perform by hand. This modified approach results in equations:

$$0 = \sum_i \phi_i \cdot \frac{K_i - K}{3K_i + 4G} \quad (11)$$

$$0 = \sum_i \phi_i \cdot \frac{G_i - G}{5G \cdot (3K + 4G) + 6 \cdot (K + 2G) \cdot (G_i - G)} \quad (12)$$

To calculate using the CPA model MATLAB was used to determine the results with data exported to Excel. Using this model on the 117 samples yields slightly improved results compared to the Differential Effective Medium (DEM) model (discussed in following section) with shear and bulk moduli accuracies as $R^2=0.876$ and $R^2=0.867$ respectively with the data shown on Figures 1.10 and 1.11. It is worth noting that when the shear modulus of all elements included in the model is identical, all models thus far: RSA, ATA, and CPA yield the same results showing model consistency. This method proved to be the more accurate at predicting the shear moduli with similar results to the ATA

method for bulk moduli, but still left room for improvement. Moving forward the RSA model using both atomic and volume fractions were kept as comparative values while the CPA and DEM models were selected as the basis for future modifications to increase accuracy.

1.6 DEM model

The next model that was investigated was the differential effective medium (DEM) method which was a differential approach to the ATA model. This allowed for a more refined composition to be constructed using a gradual approach to the composition rather than a brute calculation. In order to obtain the differential model the alterations to the system must be made in such a way that small steps are taken to adjust the effective medium of the system. This is done by altering the medium $K_{DEM}(y)$ by a small step $dy/(1 - y)$ to the new effective medium $K_{DEM}(y + dy)$. This tiny alteration renormalized the medium after each new solute addition to the system, rendering that new effective medium as the host. This method still suffers from the same problem as the ATA model in that the initial selection of the host element or composition alters the end result after the addition of the other inclusions. This difference in the end result is based on the path taken to add in the inclusions. To avoid this having a dramatic influence when combining the system each differential step consisted of a fraction of each elemental inclusion based on the ratio of each component present in the final composition. In this model the element with the highest volume fraction was selected as the host element, in place of selecting the host based on the shear or bulk modulus of the element. The equations for the DEM method were based off the work of J. Berryman [22] and McLaughlin [2] with the intention of a more gradual and refined approach to determine elastic properties. In order to more accurately model the DEM method Mathematica was used to perform rapid integration. The altered ATA equations in their differential form can be modeling using the DEM equations #11-12 where G' and K' are the derivatives of the shear and bulk moduli:

$$K'(\phi) = \left(\frac{1}{1-\phi}\right) \cdot \sum_i \phi_i \cdot \left(K + \frac{4}{3}G\right) \cdot \frac{(K_i - K)}{\left(K_i + \frac{4}{3}G\right)} \quad (13)$$

$$G'(\phi) = \left(\frac{1}{1-\phi}\right) \cdot \sum_i \phi_i \cdot (G + X) \cdot \frac{(G_i - G)}{(G_i + X)} \quad (14)$$

Compared to the ATA method where the volume or atomic fractions were values simply placed in the model the DEM method builds up to the atomic ratio in an atom by atom case. The ϕ value in this model is the combined volume fraction of elements, including the host, present in the composition. As stated before, the $d\phi$ steps are done in such a way that each element increments in a fraction of a step based on the ratio of elements present in the final composition being modeled. This enables the model to slowly apply each atom of the solute and calculate the shear and bulk moduli at each step. Through this process of atom by atom addition the DEM model resulted in improved accuracy in the shear modulus compared to ATA, but still falls short in the modeling of the bulk modulus compared to simple atomic RSA and shear modulus when using CPA with values of $R^2=0.873$ for shear and $R^2=0.864$ for bulk. Data is presented on Figures 1.10 and 1.11.

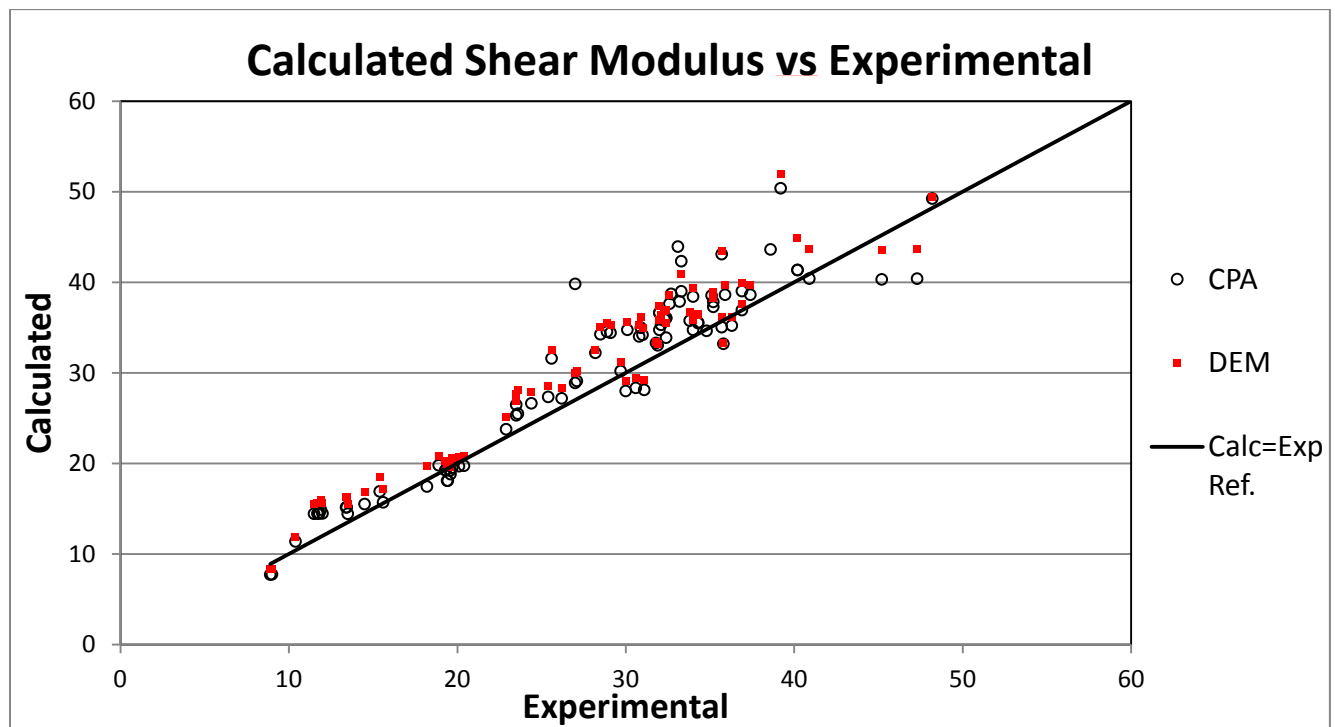


Figure 1.10- Shear modulus for 117 experimental systems calculated using CPA and DEM methods through equations (11,12) and (9,10) respectively.

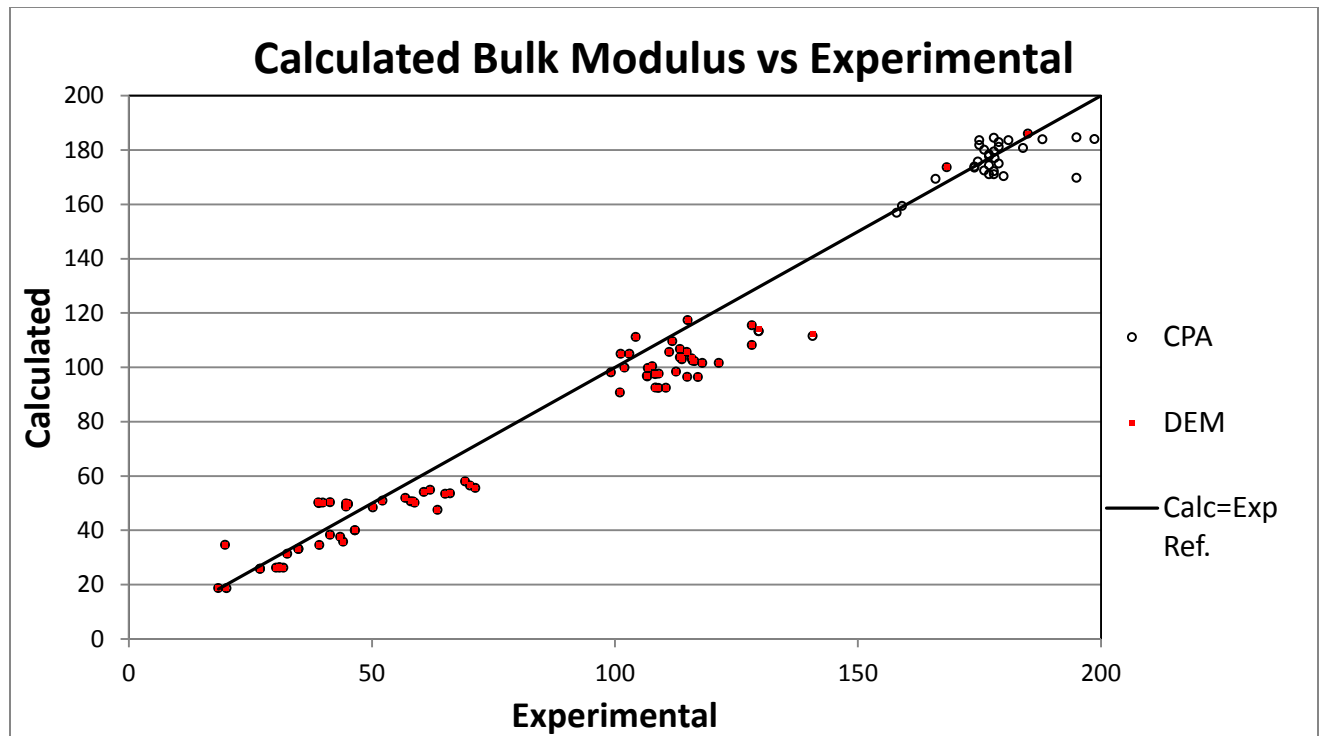


Figure 1.11- Bulk modulus for 117 experimental systems calculated using CPA and DEM methods through equations (11,12) and (9,10) respectively.

At this point the return on improvements to model accuracy through equation alteration suffered from diminishing returns and the CPA method was settled on as the "best choice" for modeling the shear modulus, as well as bulk when using volume fractions of the elements present. A combination of all R^2 results is shown in Table 1.1 for easy reference. In this table metalloid and non-metalloid systems were divided up for further analysis and model accuracy checks.

Table 1.1- R^2 correlation using select mathematical model on BMG systems shown in appendix [1].

Type and amount of system	RSA Atomic	RSA Volume	CPA	DEM
All Elements, Shear Modulus				
Non-metalloid systems=83	0.793	0.874	0.882	0.883
Metalloid systems =34	0.864	0.864	0.863	0.850
Total systems=117	0.811	0.871	0.876	0.873
All Elements, Bulk Modulus				
Non-metalloid systems=83	0.848	0.831	0.846	0.842
Metalloid systems =34	0.955	0.917	0.933	0.950
Total systems=117	0.870	0.853	0.867	0.864

Chapter 2

Atomic Structuring

2.1 Influence of atomic structure

Before any further analysis or modification to the elastic modeling was done on amorphous systems the difference between amorphous and crystalline had to be further understood. Beyond simply the structure difference between crystalline and amorphous atomic sites how the system responds to stress and strains must be defined. The way to think about the bulk and shear modulus is to consider them in terms of bonding. The bulk modulus is the system reaction to hydrostatic pressure while the shear modulus is a measurement of the system responding to shear stress. Under these stresses the bulk modulus measures the bonds being stretched or compressed while shear modulus is the bonds stretching and compressing in conjunction with bond angular distortion. When comparing crystalline systems to amorphous systems the measured values for the bulk modulus are typically around 6% larger in crystalline systems compared to amorphous ones [25, 26]. As for shear modulus the amorphous systems are about 30% weaker when compared to the same composition in a crystalline structure [25-30]. That is not to be considered a direct and exact ratio for both bulk and shear modulus comparing amorphous to crystalline systems, merely an average over recorded experimental results. It must also be considered that amorphous systems are not always fully amorphous and contain small microstructures or multiple phases.

With a deeper look into the bulk modulus of amorphous versus crystalline systems the fundamentals of what a system's bulk modulus must be understood. For a crystalline system the bulk modulus is based on the interatomic potential energy well and the equilibrium spacing between those adjacent atoms. As the curvature of the potential well increases or the equilibrium spacing shrinks the bulk modulus increases. On average, metallic glasses are 0.5-2.0% less dense than their crystalline counterpart, increasing the interatomic equilibrium spacing. If the bonding between the atoms is assumed to be roughly similar in strength (yielding the same interatomic potential energy

well) for the crystalline and amorphous systems this separation increase can accurately explain the difference between the bulk modulus of each structure [25].

When observing the shear modulus of amorphous systems compared with crystalline ones the increase in atomic spacing alone cannot explain the 30% reduced values in amorphous systems. Chen's work on structural relaxation and its influence on the density and Young's modulus of metallic glasses demonstrated that with annealing and restructuring of the material the volume and Young's modulus did not follow the expected relationship, suggesting outside influence [31]. Following this logic Weaire and others proposed that it was the restructuring of the atoms inside the amorphous system that caused environmental differences for each atom, and how they respond to shear stress once applied [32]. The wide range of environments present in a random amorphous system results in some regions in which the structure is unstable. When undergoing a shear stress the way in which each atom responds to the macroscopic strain determines how the displacement occurs. Because the local environment for each atom is different, the displacement that occurs for each atom varies, and in simulating this displacement what is called "internal rearrangement" occurs [32-34]. The rearrangement is more common in the unstable regions, resulting in the movement of both the regions surrounding these unstable ones, as well as the atoms present inside the region. This results in not only individual atoms being moved, but entire regions being readjusted to create a more stable environment. This rearrangement was modeled as a small local event, but the cumulative effect of these strains results in a macroscopic strain event [35]. It is due to these local events, and the impact they have on the macroscopic scale, that the amorphous systems are believed to have dramatically reduced shear moduli compared to their crystalline counterparts.

2.2 Crystalline modeling

With the knowledge that crystalline and amorphous systems had dramatically different elastic moduli values the next step taken was to use the same EMA model on crystalline systems. To do this, four models: RSA atomic fraction, RSA volume fraction, CPA, and DEM were taken forward and used on a set of 17 crystalline compositions to determine their accuracy. The systems investigated included: Fe-Cr-Ni [36], Ti-V[37],

and Cr-Fe[37] with their moduli and compositions shown in appendix [2] and were selected due to the elements included and the moduli measured. When these compositions were modeled using the two RSA models, ATA, and CPA the coefficients of determination are shown in Table 2.1.

Table 2.1- Elastic Moduli Coefficient of Determination:17 Crystalline Metallic Systems

Property	RSA Atomic	RSA Volume	ATA	CPA
Shear Modulus	0.873	0.873	0.866	0.866
Bulk Modulus	0.897	0.898	0.898	0.896

It is worth noting that the shear modulus modeled for both crystalline and amorphous systems was above the experimental values while the bulk modulus was typically underestimated for crystalline systems and overestimated for amorphous. The bulk modulus of the amorphous systems reached an R^2 of around 0.867 compared to the 0.898 for crystalline and a shear modulus value of 0.876 for amorphous and 0.870 for crystalline. These values are quite similar, with crystalline being more accurate on bulk and amorphous more accurate on shear.

As a net result, the EMA method does not have a dramatically higher accuracy when modeling crystalline versus amorphous systems, and has room for improvement on both fronts. The EMA method does over-estimate the bulk modulus of the amorphous systems, and is both above and below on crystalline systems. This may be caused by the structure of the crystalline systems having a dramatic influence on the bulk modulus, which was not accounted for in any of the present models. As a result of each structure having a different packing fraction the interatomic spacing is altered, raising or lowering the bulk modulus. As for shear, the EMA model overestimates in both cases which is most likely due to the structural setup not being taken into account for both the crystalline and amorphous systems. This inaccuracy on both structure styles when using simple elemental values suggests the need to include additional terms to more accurately model the elastic moduli.

2.3 Cluster Modeling

While the accuracy of the models thus far is a fair estimate of the elastic moduli there still remains additional factors that must be accounted for when modeling the properties of a system from base elements. The dramatic difference between the crystalline and amorphous experimental data for shear modulus, and to a limited extent bulk, shows the strength of the structure in determining the elastic properties. In order to more accurately model the shear and bulk moduli of metallic glass systems the short and medium range atomic structuring were both considered due to potential impact on elastic moduli. By including the properties of atomic interactions, as well as the properties of the elements individually, the model was modified to create a more accurate analysis of the system. This was done by first incorporating the positions of the atoms when arranged in an amorphous metallic glass system. This is not to say that the atoms have a long range, repeated pattern in amorphous systems only that the atoms prefer to arrange themselves in preferential locations based on the chemical composition of the system. Due to chemical interactions between the constituent elements more energetically stable bonds would be more likely to occur, influencing the nearest neighbors that each element would most likely obtain.

The cluster model was proposed by Miracle, Sanders, and Senkov in 2003 to describe how the atoms in an amorphous system would most likely organize themselves just prior to being critically cooled into a solid state [38]. This model was designed to understand how the atomic packing occurred in amorphous systems that were capable of forming densities in excess of 99% of the crystalline structure [39, 40]. In order to achieve this level of compaction the constituting elements had to have a specific collection of properties, something that was not present in all metallic glass systems. This included atomic ratios as well as atomic radii ratios between the solute and solvent element. The atomic radii ratio was defined as R , which is the ratio of solute atomic radius normalized to solvent atomic radius. This ratio, R , was then used to compute the coordination number, N_T , of solvent atoms needed to fully enclose the solute atoms in a cluster. The 3-D coordination number was calculated using Miracle's model as shown in equations #16-18 yielding the results shown in Table 2.2.

$$N_T = \frac{4\pi}{6 \cos^{-1}\{\sin(\pi/3) \cdot [1 - 1/(R+1)^2]^{1/2}\} - \pi} \quad \text{for } 0.225 \leq R < 0.414 \quad (16)$$

$$N_T = \frac{4\pi}{8 \cos^{-1}\{\sin(\pi/4) \cdot [1 - 1/(R+1)^2]^{1/2}\} - 2\pi} \quad \text{for } 0.414 \leq R < 0.902 \quad (17)$$

$$N_T = \frac{4\pi}{10 \cos^{-1}\{\sin(\pi/5) \cdot [1 - 1/(R+1)^2]^{1/2}\} - 3\pi} \quad \text{for } 0.902 \leq R \quad (18)$$

Table 2.2- Coordination numbers (N) and the corresponding radii ratio R_N^* , reproduced from Miracle [40]

N	R_N^*	N	R_N^*
3	0.155	12	0.902
4	0.225	13	0.976
5	0.362	14	1.047
6	0.414	15	1.116
7	0.518	16	1.183
8	0.617	17	1.248
9	0.710	18	1.311
10	0.799	19	1.373
11	0.884	20	1.433

Using these coordination numbers, and the atomic ratio of the elements present in the metallic glass system it is possible to predict the packing efficiency of the metallic glass system. Beyond simply computing the packing efficiency and density of the system the cluster model was able to predict the ratio and location of specific types of atoms in a theoretical metallic glass system. This enabled the structure of metallic glasses to be theorized and analyzed to better understand the short and medium range ordering. By incorporating this short and medium range order into the modeling of the elastic properties of the glasses alterations could be made to the influence each element had on the system as a whole. Located in Figure 2.1 is Miracle's demonstration of the coordination number and radii ratio showing progression as the radius of the solute grows compared to solvent. Section A demonstrates the influence of the atomic radii ratio on the entrapment of the core atom by surrounding it with increasing amounts of similar

radii atoms. Section B is a demonstration of the number of amorphous binary systems discovered given the number of atoms it takes to entrap the second element in the binary system. The higher probability of amorphous binaries existing with entrapment using 9, 10, 12, and 17 atoms compared to adjacent ratios demonstrates a preferred radii ratios for optimal disorder in creating amorphous systems. Section C is a 3D modeling of the distinct radii ratios and the locations of the atoms needed to ensnare and isolate the central atom.

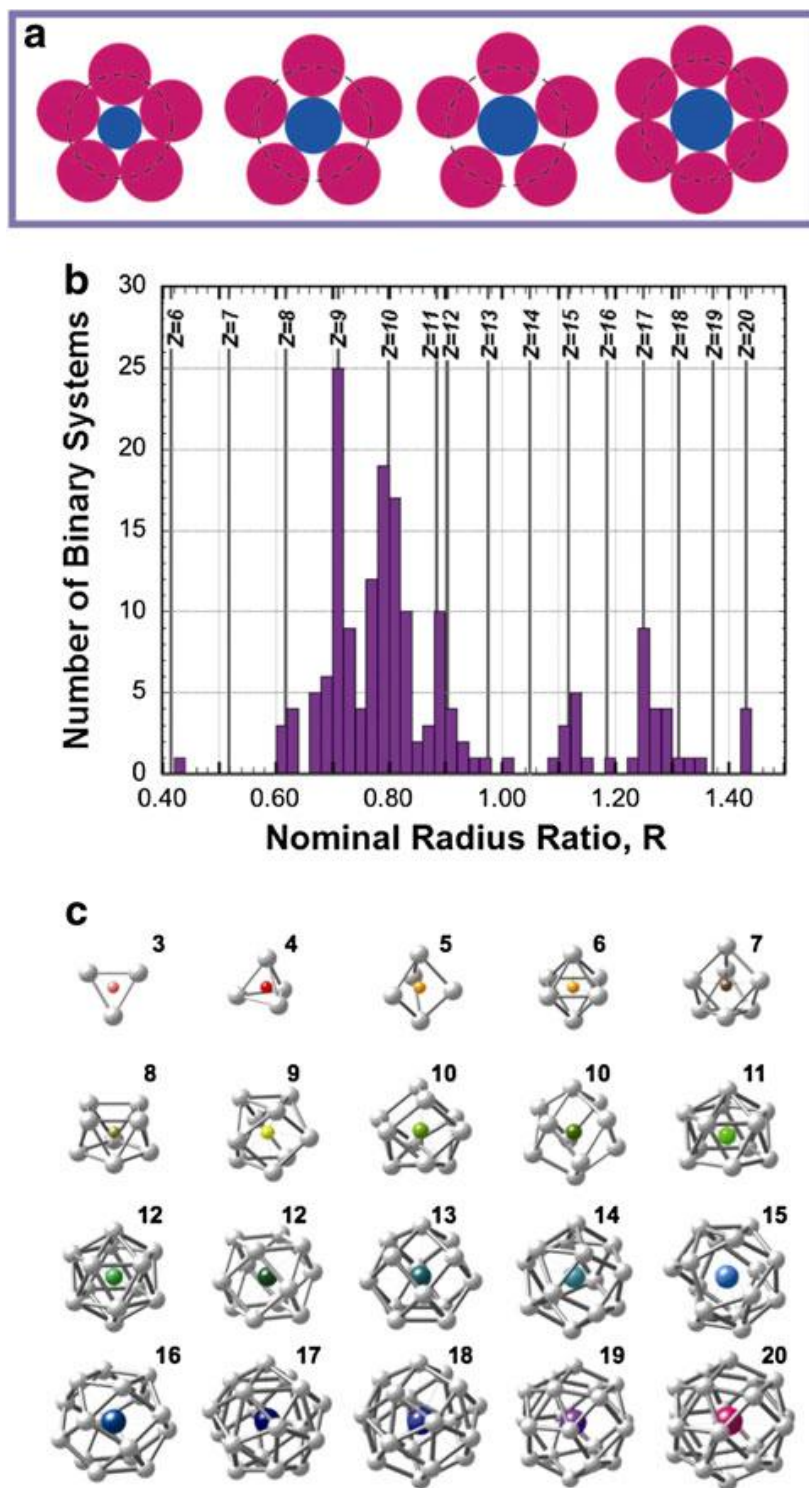


Figure 2.1- Miracle Model coordination number and atomic structure based on radii ratio [41]

2.4 Cluster atomic sites

In the cluster model there are four distinct sites for atoms to be located: Ω , α , β , and γ . The omega site is solvent element forming the cluster shells. The alpha site is the primary solute element, acting as the core of each of the clusters surrounded entirely by omega sites. The beta and gamma sites are locations present between omega/alpha site clusters. This is shown in Figure 2.2 with a 2-D slice in part a and a 3-D arrangement in part b [40].

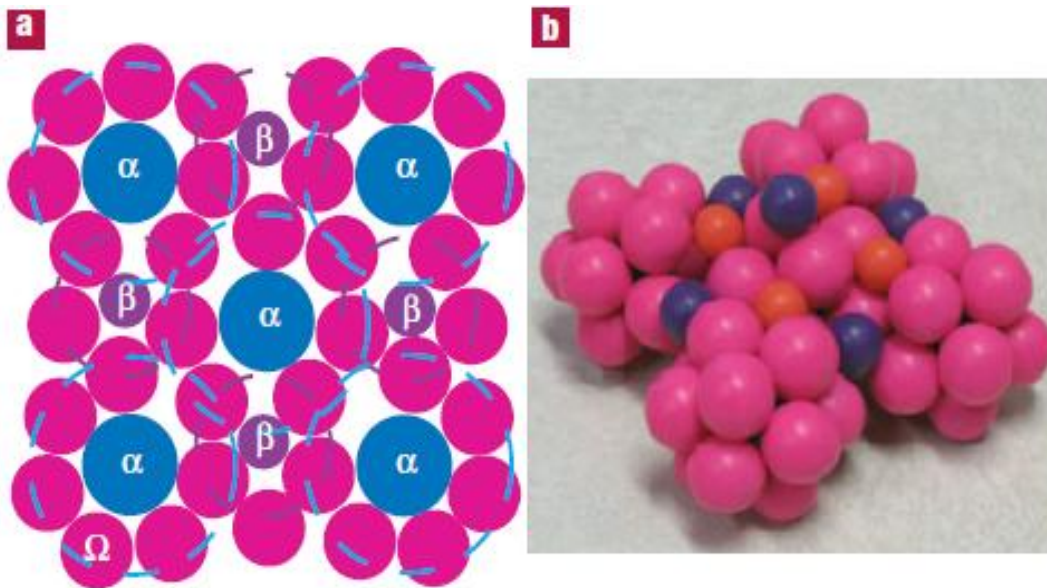


Figure 2.2- 2-D and 3-D representations of atomic ordering in Miracle cluster model with pink being Ω , blue being α , purple being β , and orange being γ [40]

It is worth noting that the ratio of Ω : α : β : γ site amount is dependent on the coordination number, which is based on the atomic radius ratio. If the system follows fcc style packing the α : β : γ ratio is 1:1:2 whereas if the packing is bcc α : β : γ yields 1:1.5:0 and sc yields 1:1:0 as gamma sites do not exist in these packing structures. For the majority of this work the fcc style packing was used to determine the α : β : γ site ratio, though special attention should be placed on the selection of cluster packing when creating theoretical new compositions or structures. It should also be noted that the size of the alpha, beta, and gamma sites is determined by their individual coordination number. In

this model the largest coordination numbered element is considered in the alpha site, with the second largest falling into beta, and third into the gamma site.

2.5 Application of cluster model

Following the adoption of the cluster model to simulate the short and medium range order of metallic glass amorphous systems alterations could be made to the influence each element had on the system. To include the effects of the cluster structure on the system as a whole the first step was to determine the influence of the alpha site on the omega, beta, and gamma sites. This was done by attempting to account for the influence the omega shell had on the ability of the alpha site to contribute the system due to the isolation of the alpha (and beta and gamma) site element. When using the elemental values without alteration or modification it implies that those elements are bonded in the same manner as their pure elemental system. This allows those elements to play a contributing role in determining the properties of the system as a whole, despite being, in the case of alpha, beta, and gamma sites, completely isolated from other atoms of the same element. In isolation their interaction with the omega site element is their only real influence as amorphous systems in the cluster structure as only short and medium range ordering exist. This interaction was used to predict and alter how the alpha site element contributed to the system in several different ways.

One of the most important points about the cluster model as described so far is that it is the ideal case, not typically found when compared to actual experimental systems. In the ideal amorphous system using the cluster model the ratio of elements present falls in the exact ratio of sites available using that structure. The site ratio is determined by equation #19 where S_Ω is the effective number of omega sites, $N_{\alpha-\Omega}$ is the coordination number for omega sites per alpha site, and N_ϕ the number of overlapping shells. In the ideal case there is no shell overlap, each shell forming its own entity, resulting in the number of omega sites being equal to the coordination number $N_{\alpha-\Omega}$.

$$S_\Omega = \frac{N_{\alpha-\Omega}}{1 + \frac{N_\phi}{N_{\alpha-\Omega}}} \quad (19)$$

In the ideal case, if a radii ratio R of 0.902 is selected this causes 12 potential omega sites for each alpha and beta site with 2 gamma sites in an fcc structure. In a more complex system the clusters may be arranged so that the shells overlap, allowing each omega site to participate as a shell element in 2 distinct clusters. This arrangement yields an overall value of N_ϕ is 12, since each of the omega site atoms interacts with a unique distinct cluster. In order for this to happen the shells need to overlap, resulting in each omega element counting as part of the shell in two distinct clusters, reducing the number of total omega site atoms needed. This results in an effective S_Ω of 6 omega sites, as each solvent element acts as an omega site for 2 clusters, dramatically reducing the atomic fraction of the omega site element needed to form a cluster model. This results in an effective site ratio of $\Omega:\alpha:\beta:\gamma$ as 6:1:1:2 given a coordination number of 12. Given that the structure of the clusters and their overlap is caused by the radii ratio of the omega to alpha elements the beta and gamma sizes do not influence the spread of the atoms in the cluster packing. It is essential to again note that the alpha site is the element with the highest coordination number, determining the ratio of $\Omega:\alpha:\beta:\gamma$ sites. It is the use of this overlap value that determines the extent to which the alpha, beta, and gamma sites can be filled. If the overlap value is already set to the coordination number no more alpha (and therefore beta and gamma) sites can be created. If the system has atomic ratios with the solute elements exceeding the solute sites in the cluster model the solutes begin to take the place of the solvent in omega sites. This begins to dramatically alter the cluster model into an amorphous system with entirely random atomic sites and no real cluster formation. The model is most applicable when the system falls in the border region of solute rich and solute lean, as shown in Figure 2.3, where the clusters are created and solute is not widely isolated.

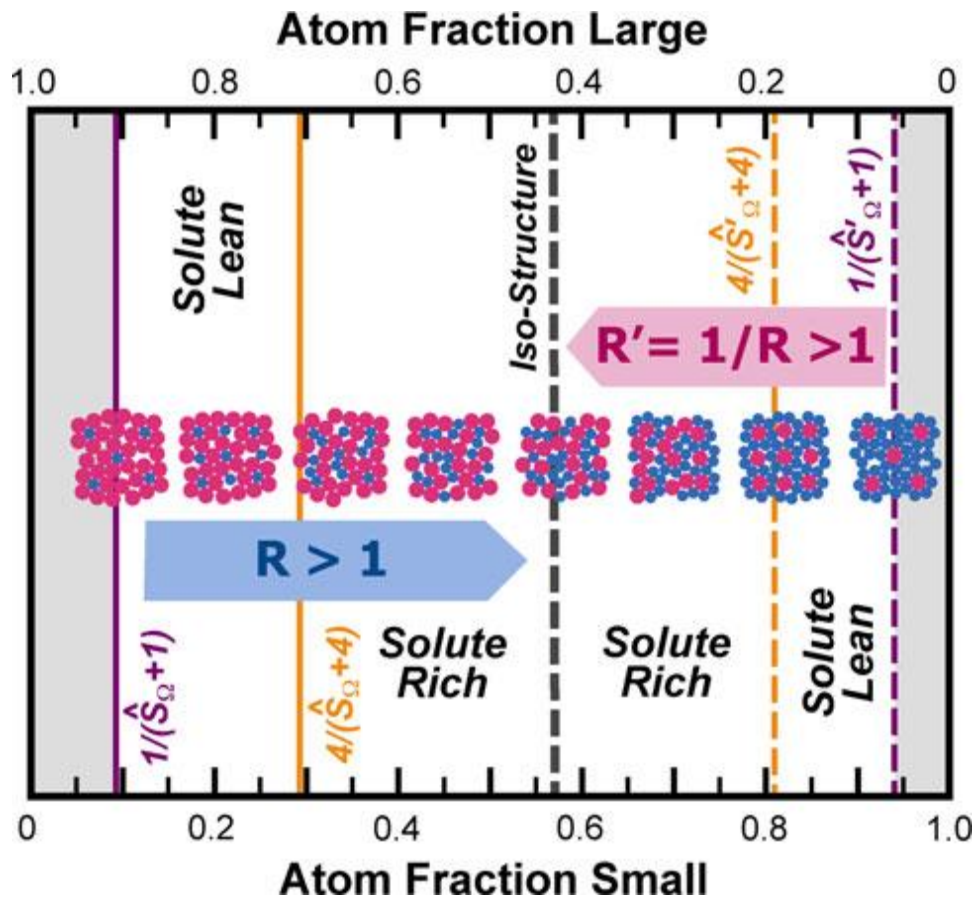
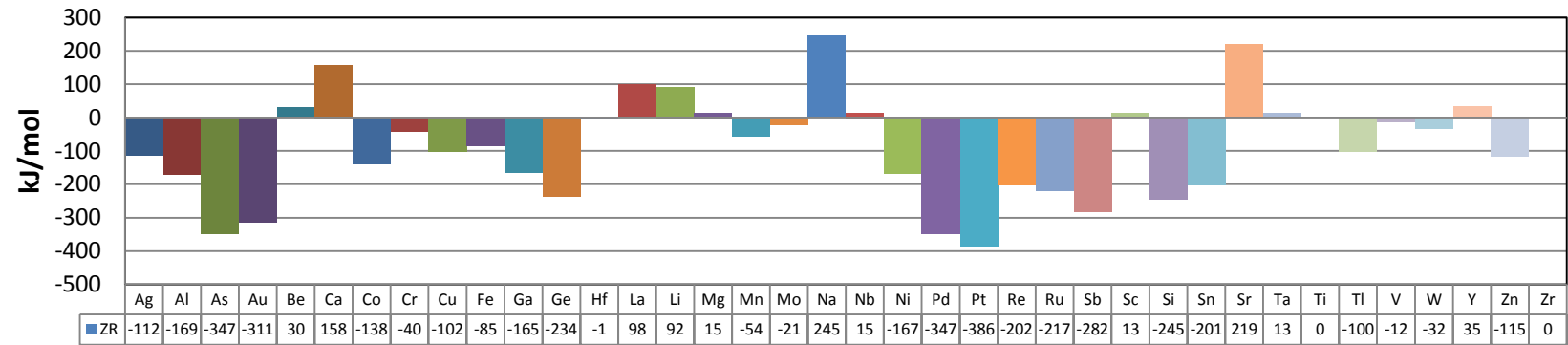


Figure 2.3- Atomic fraction of solute versus solvent. Demonstration of solute rich versus lean and cluster formation [41]

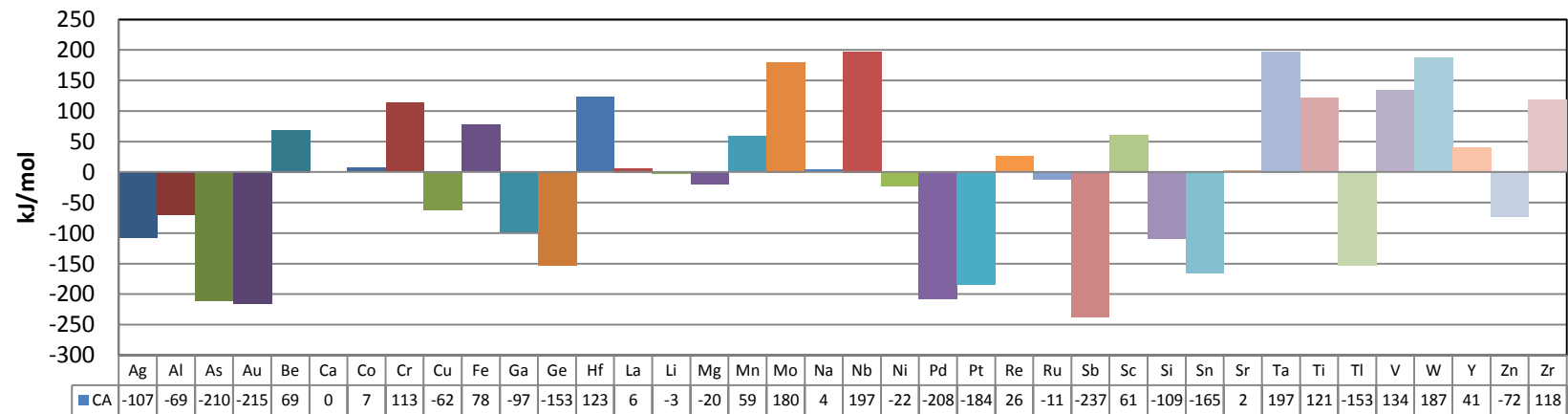
In order to model systems where the solute atomic percentages exceed the number of available alpha, beta, and gamma sites the solute elements needed to be broken into two sub-categories. This became a fairly complex system as beyond simply determining the radii ratio (and as a result, coordination number) the bond attraction and heat of formation between the elements needed to be accounted for. The elements that were most likely and stable to bond with the solvent element would fill the alpha, beta, and gamma sites before other elements, especially when the solute atom count exceeded the viable locations. To determine this, the heat of formation and bonding stability were investigated for the dominant metallic glass structures with the five dominant solvents selected for heat of formation checks. These heats of formation are shown in Figures 2.4-2.8 with the intention of determining which element would be selected as the most likely candidate to be surrounded by the host element. Using this, in conjunction with the radii

values, elements were selected to fill the alpha, beta, and gamma sites with excess elements forming clusters with no specific location. These excess atoms were then treated as acting as the base element with no alterations made to their contributing properties.

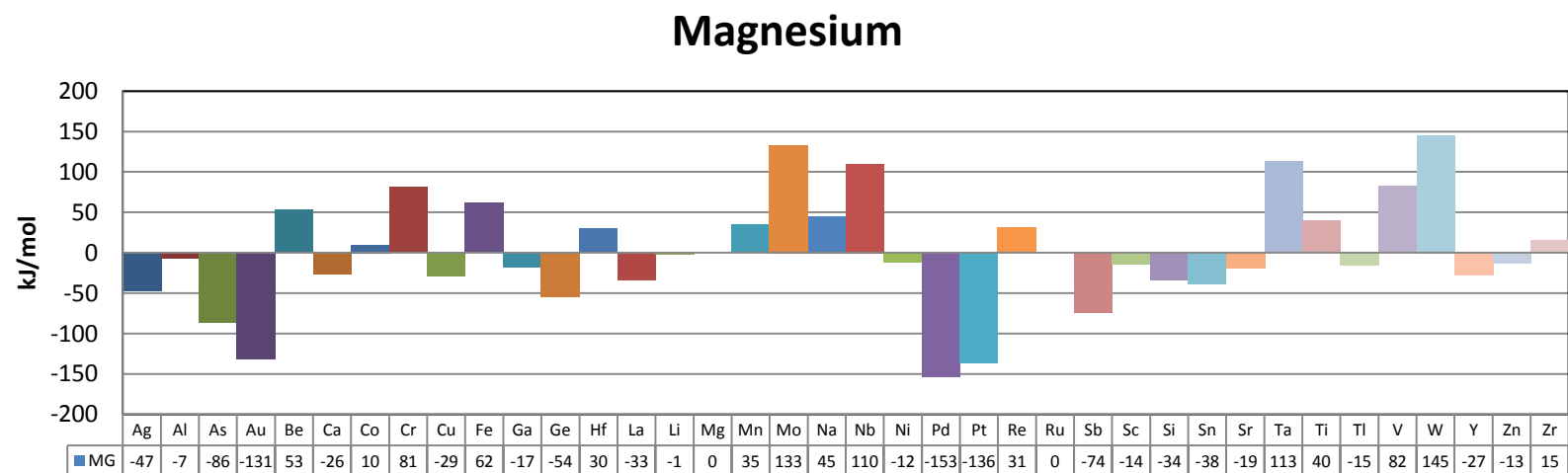
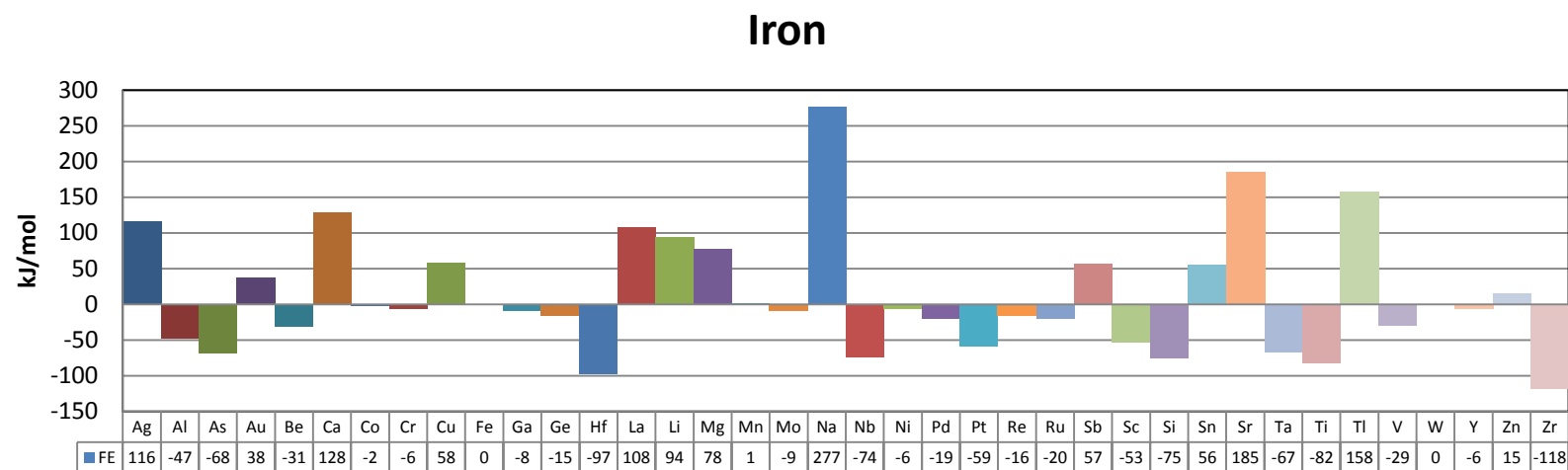
Zirconium



Calcium



Figures 2.4 and 2.5- Heat of formation of the demonstrated binary systems in kJ/mol for Zirconium and Calcium binaries respectively.



Figures 2.6 and 2.7- Heat of formation of the demonstrated binary systems in kJ/mol for Iron and Magnesium binaries respectively.

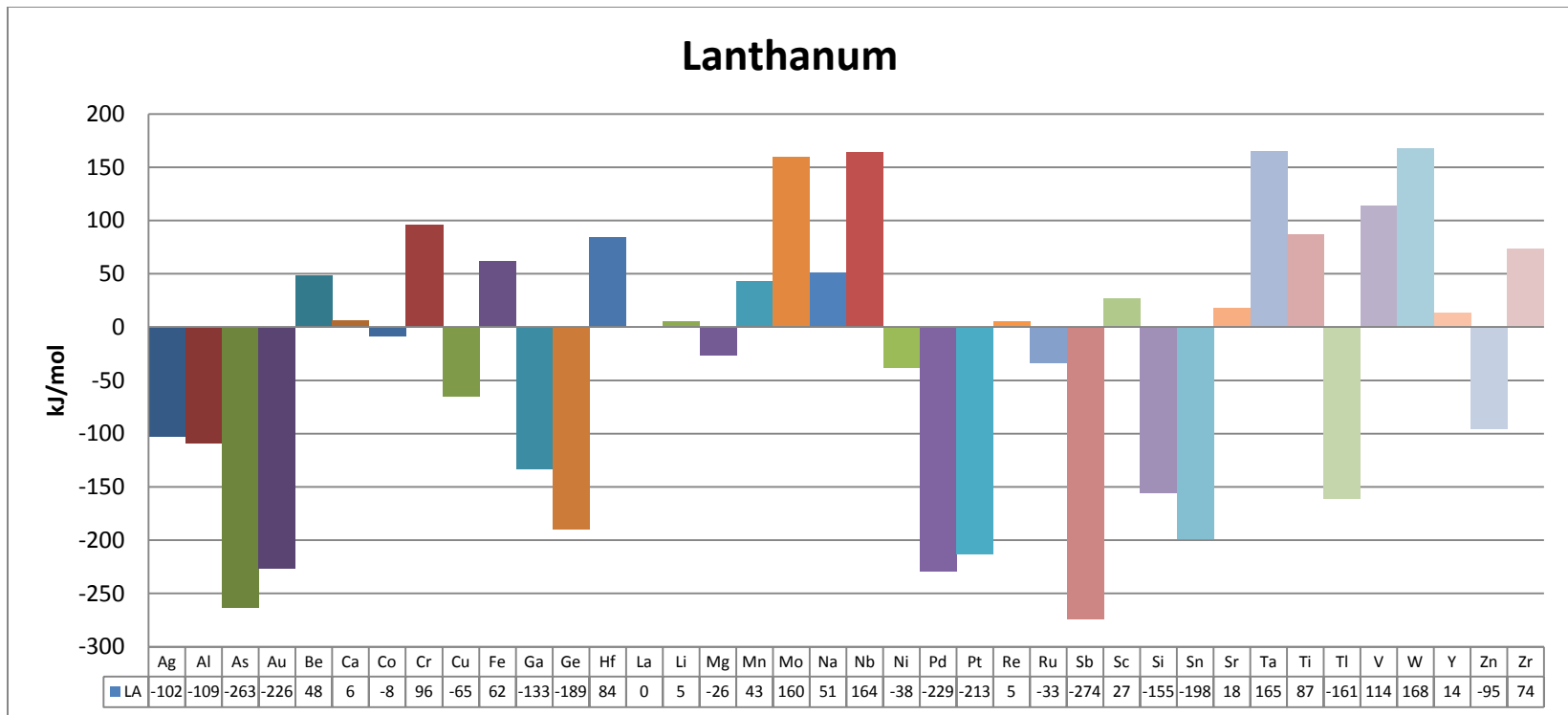


Figure 2.8- Heat of formation of the demonstrated binary systems in kJ/mol for Lanthanum binaries.

2.6 Modeling using cluster method

One assumption that must be made before beginning to model the cluster method is to determine what influence the elements that are not accounted for in the site selection have in determining the properties of the whole system. In this modeling work the first assumption was the concept that excess solute atoms with no cluster site in which to be placed would act as the base element, bonded to similar element atoms. In order to control the system even further and limit the number of independent variables present the cluster overlap fraction had to be controlled, determining the number of each site present. If the cluster overlap value was left unselected the possibility of isolated versus non-isolated solute elements would be too high to properly model as the influence of each element would dramatically vary based on its location. To combat this, the overlap value was set to the highest possible value which is same as the coordination number determined by radii of the alpha and omega elements. In the case where the number of solute elements did not match or exceed the maximum number of sites the selected coordination number was reduced allowing for clusters to still be created but the overlap of omega sites to be reduced. It is worth noting that this combined alteration of isolated and non-isolated solute elements altered the mathematical models in manageable ways. In place of i (found in the ATA, CPA, and DEM models) being the number of elements present in the system it is increased to being the number of elements present plus 3, accounting for the alpha, beta, and gamma site contributions. In this way the shear and bulk moduli of the elements present in the alpha, beta, and gamma sites needed to be calculated before performing the mathematical model in its current state.

With these contributions in mind the models were altered to account for changes created by the cluster packing style. The first alteration was a simple brute force adjustment of the isolated site shear/bulk moduli. This is referred to as $G_x \rightarrow G_x'$ in which the shear and bulk modulus of the isolated elements was altered to be a hybrid of the dominant element and that particular isolated element. This was calculated in a 50-50 influence ratio using a value of 0.5 for ϕ using equation #1. The following step was to perform the same analysis in a 50-50 influence using the RSA calculation using equation #3. The resulting accuracy values are shown in Table 2.3 with the brute force approach

increasing the accuracy of the RSA models as well as in the CPA model. When using the RSA influence calculation the accuracy of the all of the models increased compared to baseline accuracy as well as the $G_x \rightarrow G_x'$ method.

Table 2.3- Elastic Moduli Accuracy using Cluster Style Modeling

Model Method	RSA Atomic	RSA Volume	CPA
Shear Modulus			
No change	0.810	0.871	0.876
$G_x \rightarrow G_x'$	0.834	0.875	0.878
RSA $G_x \rightarrow G_x'$	0.855	0.881	0.882
Shell Select	0.881	0.889	0.889
Bulk Modulus			
No change	0.870	0.853	0.867
$G_x \rightarrow G_x'$	0.873	0.848	0.860
RSA $G_x \rightarrow G_x'$	0.862	0.839	0.846

Once the accuracy increase was noted using alterations to the influence of the isolated atoms to the system further alterations methods were attempted. The next step was to determine if the difference between the shear and bulk moduli of the isolated elements and the omega site solvent determined the influence the atoms had on the system. This was done by treatment of modulus of isolated atoms in a method called "shell select" based on the properties of the omega site shell and alpha, beta, and gamma isolated sites. For shear, if the modulus of the isolated element was greater than the shell treat isolated as the shell value. If isolated was less than shell treat isolated as the isolated elemental value. For bulk it was treated in the inverse manner where if the isolated element had a higher bulk modulus than the shell element the isolated was treated as the

isolated elemental value. If the isolated was weaker than the shell the isolated element acquired the shell value. This had an improvement compared to baseline model, as well as the RSA and direct sum $G_x \rightarrow G_x'$ modifications for the shear and bulk moduli. This method of selection as to which elemental value to pick for the isolated element was based on how the force would be distributed over the clusters that formed in the amorphous system. When undergoing a shear stress the weakest element would be the dominant element, akin to springs in which the weakest spring determines when the system begins to move. If the cluster was assembled from lower shear modulus elements the isolated core element would be carried along when the cluster elements moved due to the shear stress. If the isolated element had a lower elemental shear modulus it would be more likely to buckle compared to the shell elements. The same logic can be applied in reverse when considering the bulk modulus. The strongest element resists compaction, and due to the rough geometry of a shell the isolated element in the core of the sphere would benefit from the resistance of the shell to compression, or provide that resistance if the shell consisted of lower bulk modulus elements. This same logic can be seen in the direct and RSA $G_x \rightarrow G_x'$ methods as the isolated element takes on the properties of the elements of the shell, becoming stronger or weaker based on the elements providing the isolation.

It was at this point that the overarching predictions of the elastic moduli of metallic glasses reached an end point. The decline in increasing accuracy without arbitrary mathematical alterations with limited physical reasoning resulted in a pause in progress. Beyond this, the potential accuracy was limited due to the spread and uncertainty of the experimental results obtained by various groups on bulk metallic glass systems. Minor alterations to the system may require fine tuning the elastic model that cannot be taken into effect without further understanding of the elements used in the system. It is due to this "fine tuning" that the model's accuracy may be limited without delving deeply into the properties of each binary and ternary bonding set that may occur within a metallic glass system.

2.7 Metallic bonding and binary systems

The goal of this section of the project was to properly model the elastic properties of more complex systems involving three or more elements built up from smaller calculations. This was done using the *ab initio* calculations performed by Michael Widom at Carnegie Mellon University on binary systems to more accurately predict the properties of ternary style systems. By using the properties of binaries in more complex compositions it was possible to include the influence of atomic bonding on the shear and bulk moduli. As simply using the elemental values for the shear and bulk moduli of the elements present in the composition vastly underestimated the elastic properties of the samples it became essential to account for the atomic interactions to obtain accurate results.

To account for the influence of the bonding in systems more complex than a simple binary the strength of the bonds between those elements needed to be obtained. Using the elastic properties of the *ab initio* calculated binaries it was possible to determine the influence that the bonds had on the shear and bulk moduli predicted. This was done by backing out the effective shear and bulk modulus of the two elements present in the binary system and using those values to determine the influence of the atomic bond. To obtain these results equations #20-22 were used where: M_{Binary} is the measured elastic modulus of the binary system, M_A and M_B are the elastic moduli of the two base elements composing the binary while M_{AB} is how both elements act when in the binary, ϕ_A and ϕ_B are the volume fractions of the elements, and M_{A^*} and M_{B^*} are the effective elastic moduli of the elements once bonding has been accounted for. Using these equations on the *ab initio* binaries it is possible to determine the effective shear and bulk modulus of these elements when atomic bonding is taken into account. These are then used as effective moduli in the effective medium approximation making it possible to model the elastic moduli for more complex systems, in this case ternaries, far more accurately.

$$\frac{1}{M_{Bin}} = \frac{\phi_A}{M_{A^*}} + \frac{\phi_B}{M_{B^*}} \quad (20)$$

$$M_{A^*} = (1 - \phi_B) \cdot M_{AB} + \phi_B \cdot M_A \quad (21)$$

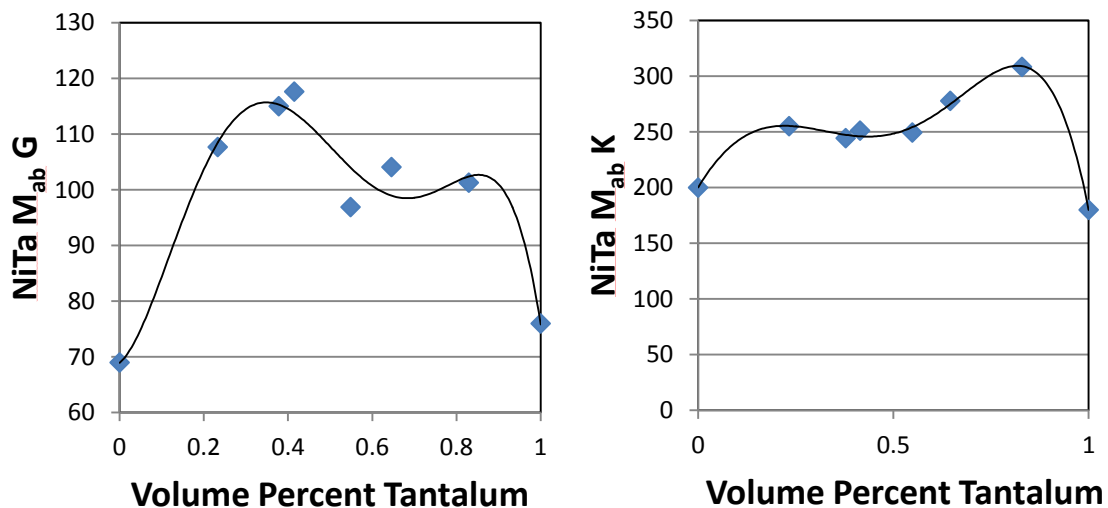
$$M_{B^*} = (1 - \phi_A) \cdot M_{AB} + \phi_A \cdot M_B \quad (22)$$

In regions of a ternary system in which the atomic bonding does not have a reliable binary to determine the bonding strength averages between the adjacent values were obtained. To obtain more accurate results more *ab initio* binaries must be calculated to more accurately show how the strength of the bonding varies based on the composition of the binary.

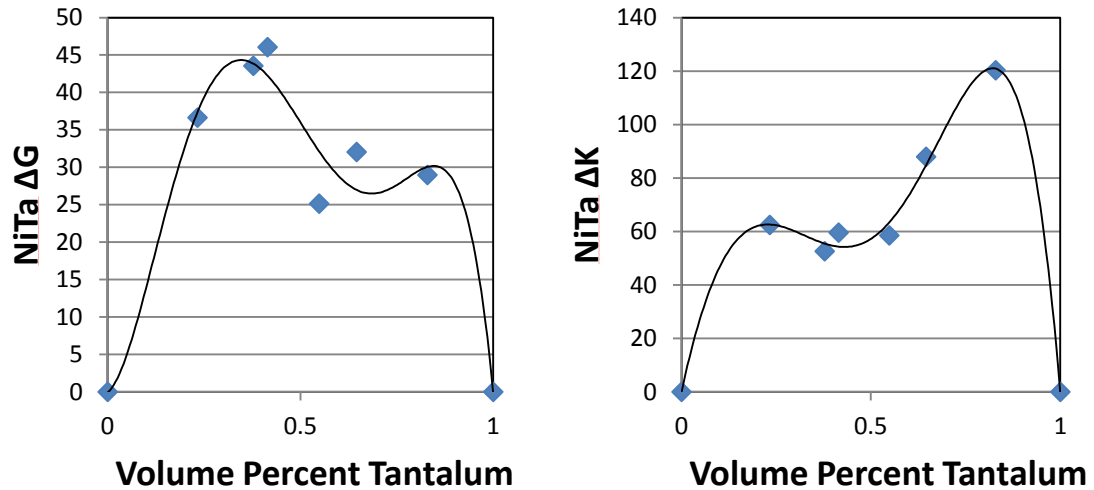
In addition to the M_{ab} method of determining the ternary system properties from binaries another method was created which will be called the "delta method". This method uses equation #23 with a far simpler method of determining the alteration to the base elements of a simple factor Δ . This is simply a constant value to adjust the moduli for each element in order to simulate the measured values of the binary system.

$$\frac{1}{M_{Bin}} = \frac{\phi_A}{M_A + \Delta} + \frac{\phi_B}{M_B + \Delta} \quad (23)$$

Several binary systems were modeled in an effort to simulate multiple ternary systems with representative demonstrations of the delta and M_{ab} systems shown in Figures 2.9-2.12.



Figures 2.9 and 2.10- M_{ab} plots with experimental data as blue points. Lines are best fit curves to predict properties of binary based on atomic ratio of elements present.



Figures 2.11 and 2.12- Delta plots with experimental data as blue points. Lines are best fit curves to predict properties of binary based on atomic ratio of elements present.

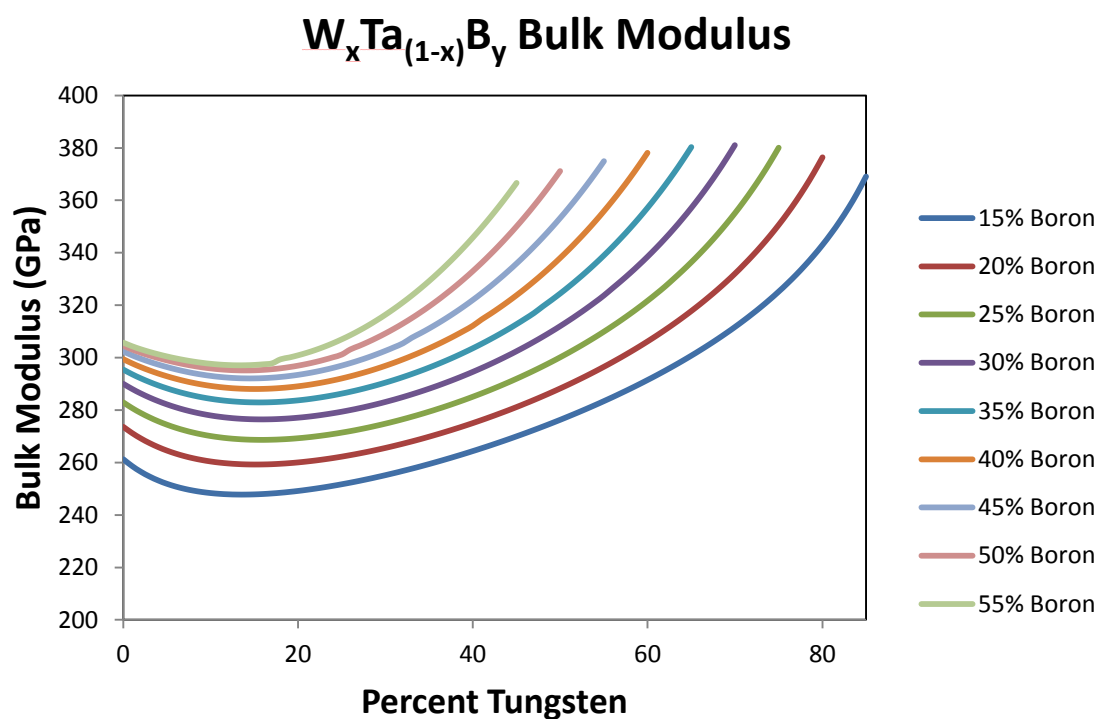
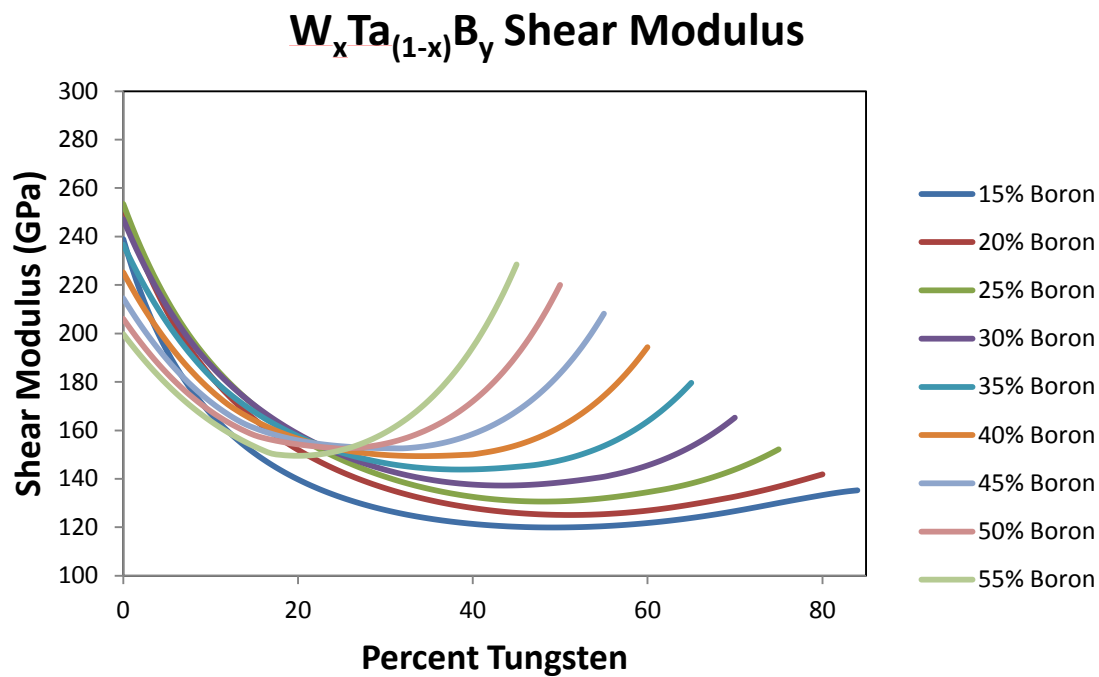
Through the use of the delta and M_{ab} calculations ternary approximations could be calculated using the ATA mathematical model. In this model the modified shear or bulk modulus calculated from the binary simulations to replace the elemental values. In order to extrapolate the properties of the elements between the known binary systems a curve of best fit was calculated to smoothly connect the known binary points. This curve was then used to predict the properties of the elemental values in those set atomic ratios when present in a ternary system. In order to relate the binary atomic ratios into the ternary system bonding priority had to be established. This was done by a set of fraction ratios to determine to which other element each individual atom was bonded. To obtain this influence of this ratio equation #24 was used where G_a^* is the effective modulus of the element once resolved, G_{ab} or G_{ac} is the modified modulus when taking into account the binary state of element a and b or a and c, and φ is the volume fraction of that element present:

$$G_a^* = G_{ab} \cdot \varphi_a \cdot \left(\frac{\varphi_b}{\varphi_b + \varphi_c} \right) + G_{ac} \cdot \varphi_a \cdot \left(\frac{\varphi_c}{\varphi_b + \varphi_c} \right) + G_a \cdot (\varphi_b + \varphi_c) \quad (24)$$

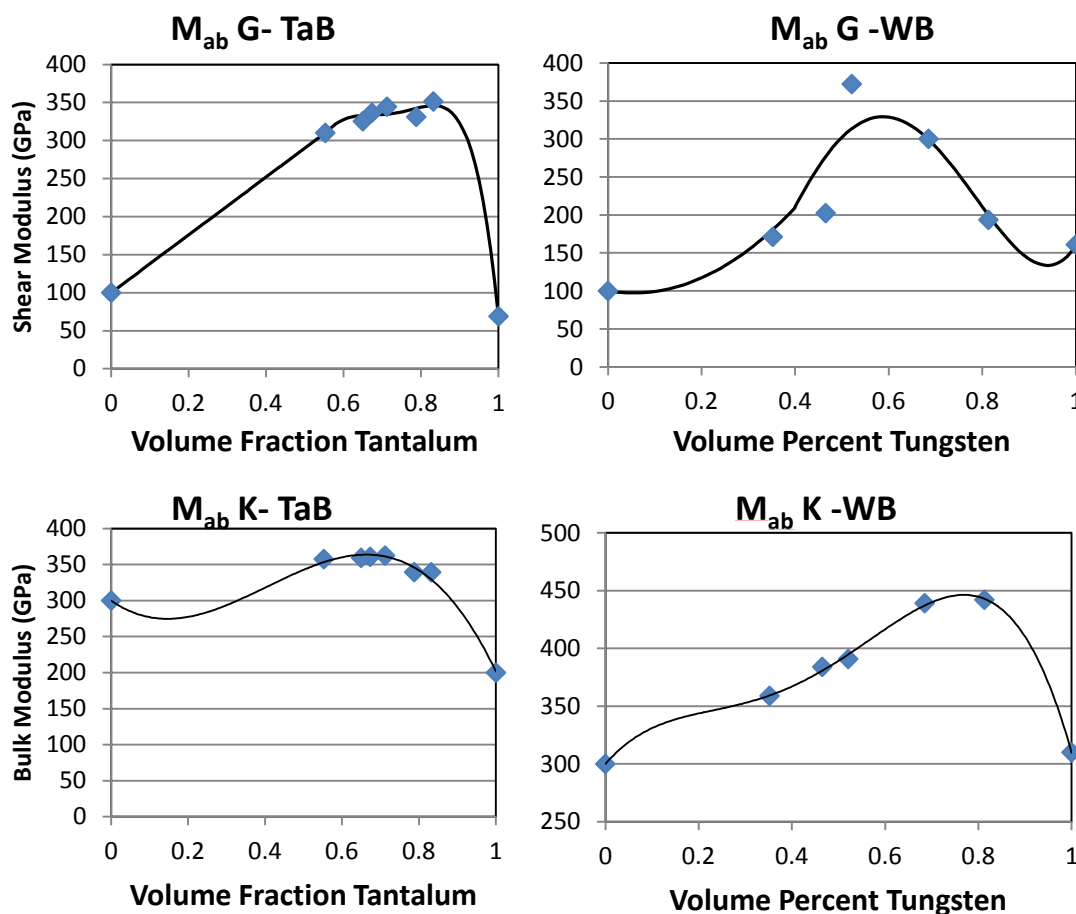
This effective new modulus was calculated for each of the three elements present in the ternary, effectively accounting for how the element would act at that ternary composition

based on how it would behave based on those elements in binary form. This does not account for any changes in the bonding that occur with three distinct elements present, rendering any alterations to the overall structure unaccounted for. This is one of the primary goals to increase the accuracy of the model as the binary data incorporates the structure of those binaries, but may not be the structure present in the ternary.

In order to demonstrate the method a WTaB ternary model was conducted in Figures 2.13 and 2.14 if the system was in exact thirds the binaries present would be W-B, W-Ta, and B-Ta. This was done through the use of the M_{ab} style system to determine the alterations to the effective moduli of W, Ta, and B based on their binary data. The figures demonstrate the modeled moduli as the system transitions from simple W-B binary systems to the gradual addition of Ta, ending in pure Ta-B binaries. Special focus must be given to Figures 2.15-2.18 which are the M_{ab} models for W-B and Ta-B. The curve of best fit for the bulk modulus is a single equation yielding points close to the binary values. However, the shear modulus modeling is far less accurate due to the wide variation in the shear modulus of the binary values. It is possible to create a more accurate M_{ab} curve to fit the binary values (yielding more accurate shear and bulk binary values on the ternary model) through a more direct connection to the binary points. This runs the risk of an even stronger bias towards the structures present in the binary systems as the elemental values decrease in their influence.



Figures 2.13 and 2.14: Bulk and Shear moduli predictions of ternary composition $W Ta B$ through the use of M_{ab} model.



Figures 2.15-2.18: M_{ab} plots for WB and TaB binary shear and bulk moduli.

To simulate the tungsten properties, in this ternary, equation #24 is used to determine how tungsten behaves in the CPA or ATA model based on the W-B binary and the W-Ta binary. It is worth noting that W and Ta do not bond and form a distinct phase so no M_{ab} plots were constructed. In that system each element behaves as it would in its elemental state. As the atomic ratio in the ternary shifted the influence of one binary would grow as the other falls away, altering the elastic properties of those two elements effectively. In this fashion the elastic properties of each element were constantly recalculated to represent the contribution to the ternary system from the effectively present binary pairs.

The overall accuracy of the ternary model did show promise for potential modeling of ternary systems without the need for atomic structuring in the form of clusters or amorphous networks. The accuracy of this method can be further tested

through the creation and measurement of ternary systems to compare the experimental results to mathematical simulations. If further adjustments or alterations to the contributions based on heat of formation or atomic bonding priority must be made it is simple to adjust the priority in the modeling software to alter the preference of each element. In this way the model may be adjusted to reflect the unique properties of the ternary (or binary) system under investigation.

2.8 Amorphous metallic elastic moduli summary

- Coherent Potential Approximation model of Effective Medium Approximation serves as a more accurate model of the shear and bulk modulus of amorphous materials than simple elemental Reciprocal Sum Approach. Using 117 sample amorphous systems the R^2 for the CPA model is 0.876 and 0.867 for shear and bulk respectively compared to 0.871 and 0.853 for the shear and bulk modulus of the RSA model.
- Using the same EMA models on a collection of 17 crystalline materials yielded R^2 values of 0.87 for shear and 0.90 for bulk with shear being over-estimated in both structured systems while bulk was over estimated in amorphous and under estimated in crystalline. Amorphous materials' experimentally determined shear and bulk moduli are around 30% and 6% respectively lower when compared to the experimentally determined moduli of the same crystalline compositions. The bulk modulus difference is believed to be due to atomic packing fraction changes whereas shear modulus is due to disorganized local structure and environmental effects in the amorphous systems.
- To account for local environmental effects in amorphous systems a cluster model was used to predict and describe the short and medium range ordering. This structuring method allowed for the accuracy of shear and bulk moduli to be slightly improved using the adjusted CPA model to 0.889 and 0.869 respectively.
- Further modifications may be made to more accurately account for the atomic interactions and structure modifications

Chapter 3

Bulk Metallic Glasses

3.1 Introduction to Bulk Metallic Glasses

Amorphous materials, as described earlier, are systems in which there is no single crystalline phase but rather the atoms are found in a random or semi-random arrangement. These systems are vitreous solids with limited if any crystallization occurring during the creation process. Through the controlling of this creation method it is possible to fabricate systems that can be classified as "Bulk Metallic Glasses" or BMG in which the amorphous structure is retained in larger (larger than a few cubic millimeter) samples. Maintaining the critical cooling rate while expanding the size of the system has proven to be one of the many challenges in creating bulk metallic glass systems. A collection of several laws exists to determine the criteria needed to halt crystallization and create the bulk amorphous systems: [8,9]

1: A BMG should contain a three or more element system to increase complexity. This creates more complex crystalline structures that must be formed, slowing the crystallization rate and increasing the energy needed to crystallize. Two element BMGs exist but the fabrication method requires extreme conditions to retain the structure free configuration.

2: Select a composition near the eutectic point in the solid:liquid transition allowing for stability once a lower temperature has been reached.

3: A negative heat of mixing to decrease atomic diffusivity and increase the energy barrier at the solid-liquid interface. This slows the reorganization of the atoms and hinders the crystallization rate.

4: Selecting a higher atomic radii ratio (as highlighted earlier) to create higher packing density and requires a larger volume change for crystallization to occur.

Using these four constraints it is possible to theorize and create BMGs though retaining the amorphous nature of the system often requires dramatically different methods based

on the properties of the system in question. The main focus of much BMG research has been in the creation of amorphous systems with lower critical cooling rates and increasing the size of the amorphous system.

3.2 Creation of BMGs

The ability to maintain the amorphous nature of the material during processing has been one of the largest hurdles in the creation of Bulk Metallic Glasses. At this moment there are two distinct pathways to create BMGs: direct casting and powder metallurgy. Direct casting follows methods similar to the creation of the first BMGs through the use of suction and die casting to rapidly cool the liquid metal. This is through the creation of the amorphous system through arc or induction style melting and rapid quenching to reach the critical cooling rate. It is due to the typically low thermal conductivity of the amorphous style systems that often hinders this approach as the thermal transport is often too slow to allow for larger sample creations. It is for this reason that larger BMGs (>1cm) are often difficult to make using this method.

The second route of powder metallurgy involves the creation of the amorphous system through heating the powders or pellets typically to within the glass transition temperature (T_g) and the crystallization temperature (T_x). While within this region the systems are deformed under pressure to create the shape and size of the desired sample. By remaining within this temperature window it is possible to bypass the limitation of the critical cooling rate imposed on the direct casting method. A figure demonstrating the crystallization and glass regions is shown in Figure 3.1 a Time-Temperature-Transition (TTT) diagram. This demonstrates the critical cooling rate needed to bypass crystallization and the temperature window in which the system may be shaped without crystallization. The two paths are the two distinct paths of creating BMG systems, critical cooling rate along path 1 and powder metallurgy along path 2.

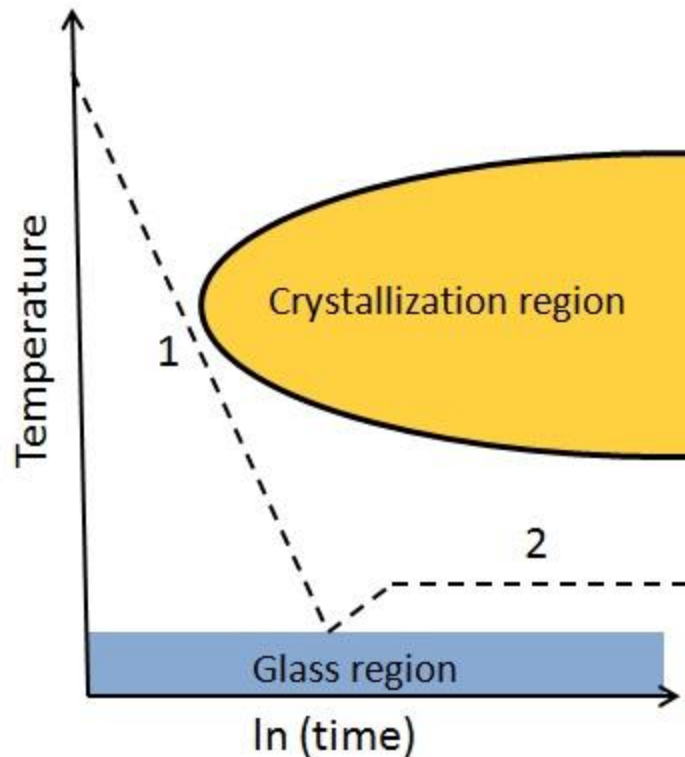


Figure 3.1- Representation of Glass and Crystallization regions with respect to temperature and time. Path 1 demonstrates rapid quenching while Path 2 represents powder metallurgy.

3.3 Comparison of BMG to crystalline systems

When comparing the BMG to crystalline materials it is essential to consider what influence the amorphous structure has on the elastic properties. Due to the liquid like structure of amorphous materials as mentioned before it is only possible to consider the short and medium range order of the atomic system. This limits the structural length of BMGs to the order of a few hundred atoms compared to the global structure viewed when dealing with purely crystalline materials. This structure enables BMGs to have a pairing of very high strength with a fairly low elastic modulus. When comparing amorphous materials to crystalline systems the elastic strain limits are often important to consider. Most crystalline metallic systems are limited to within 0.1-0.5% strain while metallic glass systems can reach to within the 1.5-2% strain limitation as shown by Inoue *et al.* [8] This enables a yield strength of nearly 3 times higher compared to crystalline materials

with the same Young's modulus. The measurement of the Young's modulus when compared to tensile strength is a factor of three lower in amorphous systems compared to their crystalline counterparts establishing a linear relationship between the tensile strength and Young's modulus, as expected if the systems follow Hooke's law. This is shown in Figure 3.2 comparing crystalline metals and bulk metallic glasses.

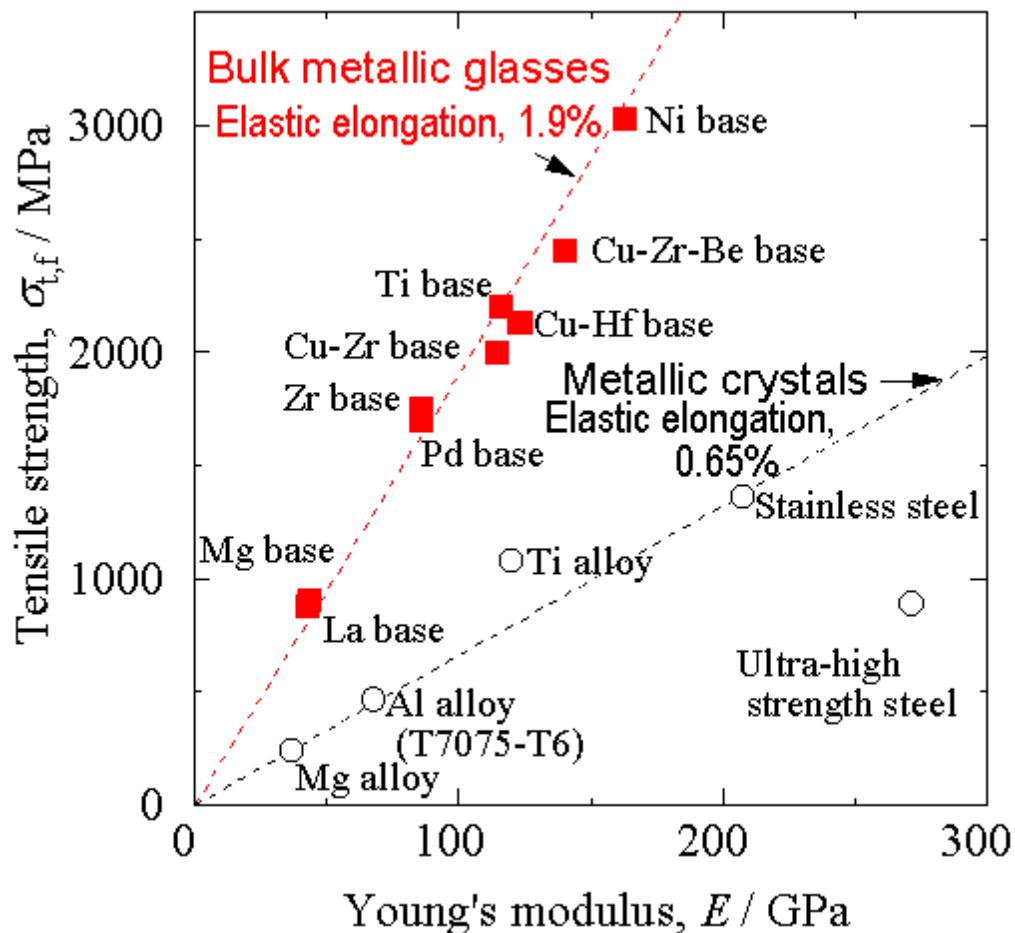


Figure 3.2- Comparison of Tensile strength and Young's modulus for BMG and crystalline metals [8]

In addition to moduli and tensile strength the hardness of the amorphous materials must be considered due to its relationship with shear modulus and flow stress. When comparing amorphous metallic systems to ceramics it has been shown that the wear resistance is higher in amorphous systems [8]. This high hardness and wear resistance

enables amorphous systems to be a viable candidate for protective layering and room temperature metallic systems. When compared with metallic crystalline systems the wear resistance of the amorphous systems was found to be dramatically higher when compared to certain steels with Inoue reporting an excess of 1000 times when comparing amorphous Ni systems to steel [8]. It is due to the liquid like structure of the amorphous systems lacking grain boundaries and defect locations that enables long term resistance to wear with Figure 3.3 demonstrating the performance of select BMGs compared to steel.

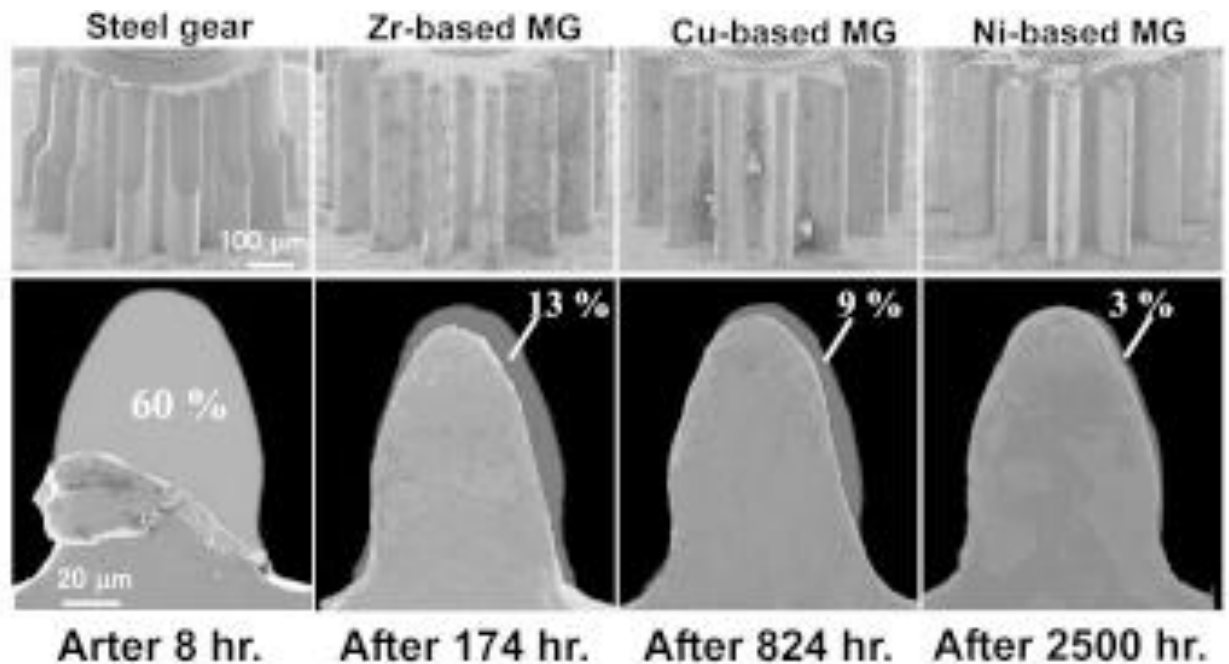


Figure 3.3- Demonstration of wear resistance and deformation on gear teeth comparing metallic glasses to steels [8]

While amorphous materials are far better at wear resistance and elastic strain compared to crystalline materials the fracture toughness of amorphous systems often falls below that of crystalline systems. Toughness is determined by the force load that the system can undertake before a fracture occurs. It is due to the lack of a crystalline structure that amorphous systems have lower load limits as the long range order allows for a distribution of plastic flow bands. This short range order prevents the distribution of the strain forcing the system to yield to propagating shear bands. It is worth considering the limits of a system with a nano-crystalline structure within an amorphous system as the

hybrid of the two structures allows for the halting of shear band propagation resulting in a higher fracture toughness [42, 43]

3.4: Creation tools for Bulk Metallic Glass systems

Spark plasma sintering (SPS) is a relatively new technique that uses the combination of a pulsed direct current and uniaxial stress to sinter the material. This method is similar to hot pressing through the application of pressure and heat, but comes with the benefit of dramatically lower creation times which serves to preserve nanocrystalline structure and limit crystallization time. [44, 45]. It is due to this rapid heating and cooling rate created through the use of current flow as opposed to inductive or resistance based heating used in the hot press. Despite the naming the spark plasma sintering involves no plasma during the sintering process [44]. With this in mind, the exact mechanisms of the SPS process are still under investigation and despite a non-perfect understanding the method is still under heavy use in the creation of many advanced materials such as nanoceramics, nanocrystalline metals, and bulk metallic glasses.

While electrical sparks are present during the sintering process there are also temperature spikes created through the method of direct current application used in the SPS process. The direct current undergoes short on-off cycles creating short bursts of current between the particles being sintered. This causes small temperature spikes in regions, raising the potential issue of localized heating as the current selects the pathway of least resistance to complete the circuit. This is shown in Figure 3.4 demonstrating the current pathway around the particles under compaction as modeled by Tokita in his work analyzing the methodology of SPS compaction [46].

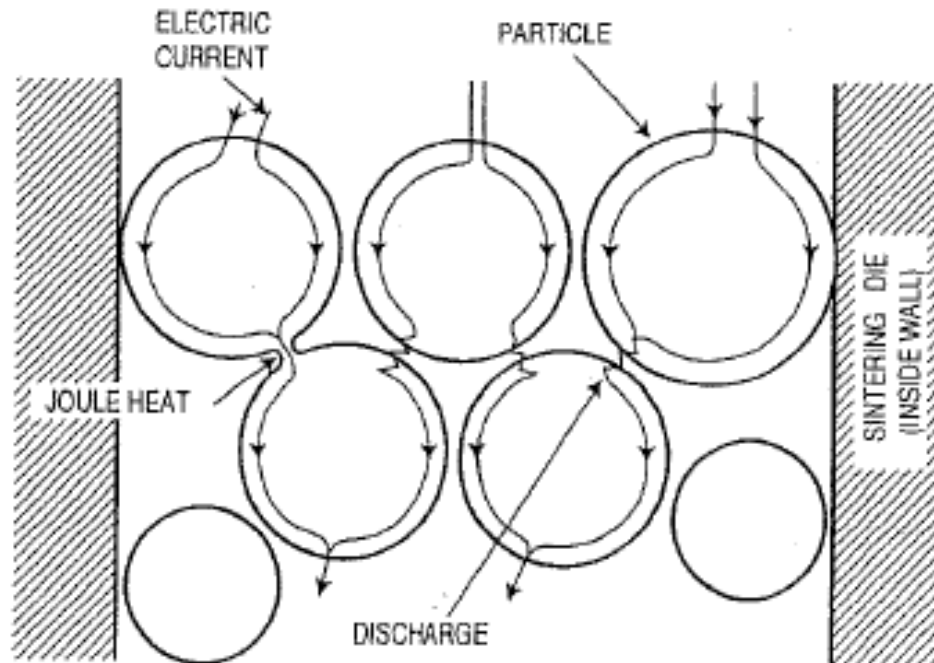


Figure 3.4- Current pathway under Spark Plasma Sintering compaction [46]

The SPS machine in use for these experiments was the Thermal Technologies SPS 10-4 capable of 10 tonnes of force (98.06 kiloNewtons) and 4000 Amps of current. The furnace chamber is capable of being pumped to ~1 mTorr of pressure and is backfilled under Argon or Helium to prevent contamination. The images of this device are shown below in Figure 3.5 for the outside of the device with Figures 3.6 and 3.7 [44] demonstrating the pressure and current applications.

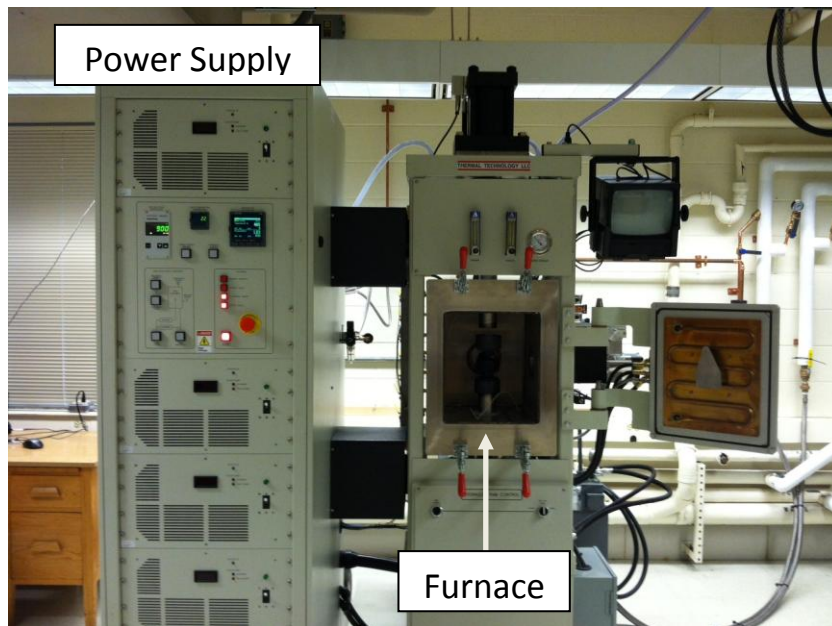
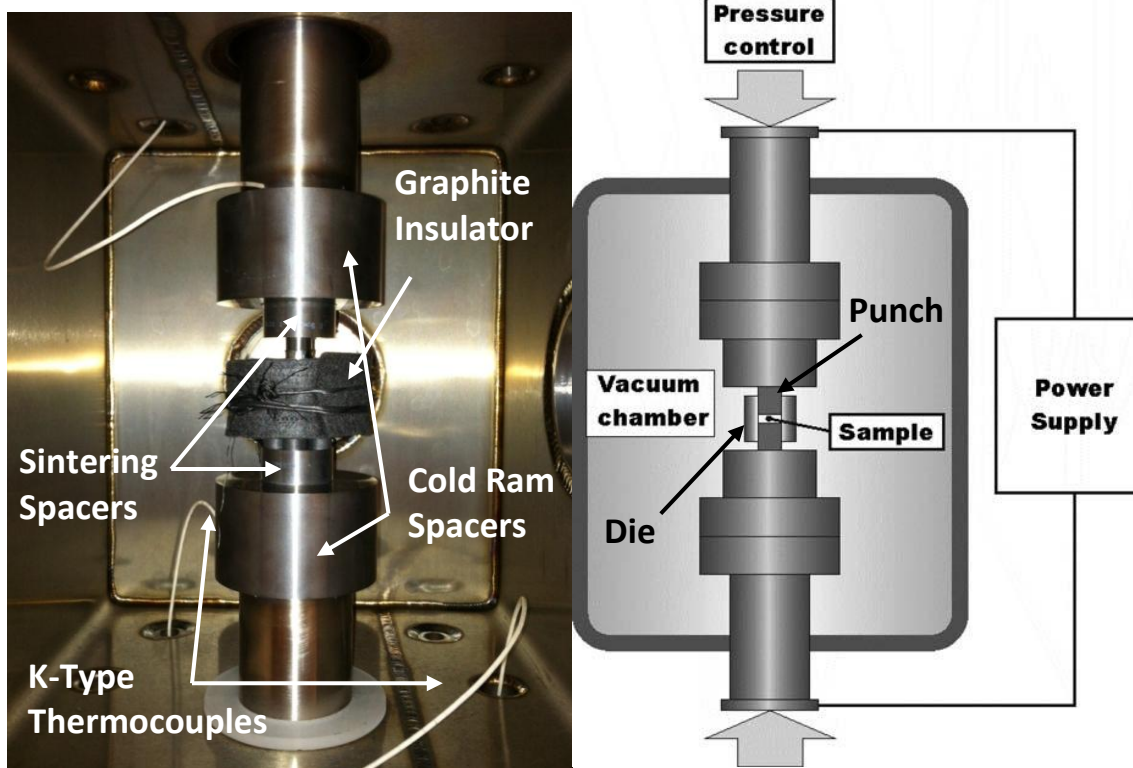


Figure 3.5- Thermal Technologies SPS 10-4 device. Hydraulic and Vacuum pumps are located behind the device.



Figures 3.6 and 3.7- Inner view of Spark Plasma Sintering furnace demonstrating the tool assembly

3.5 Spark Plasma Sintering methodology

The SPS method involves many user defined parameters when performing sample sintering including (as shown on Figure 3.8) : dwell temperature (2), pressure (5), heating rate(1), cooling rate (3), pressure rates (4 and 6), and dwell time (hold region) [45]. The influence of each of these parameters dramatically alters the properties of the created sample resulting in alterations to the phases created and the densification of the powder into a single system.

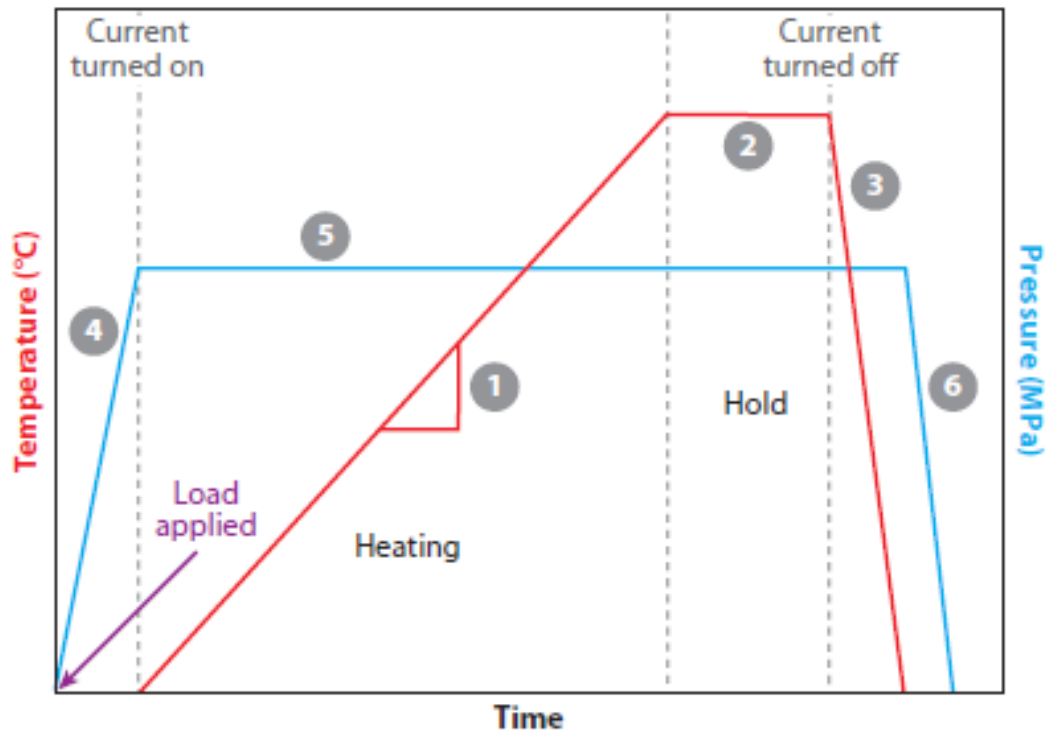


Figure 3.8- Demonstration of temperature and pressure as a function of time during Spark Plasma Sintering system compaction [45]

3.5.1 SPS temperature

The sintering temperature is the most important part in the creation of most systems in determining the final result of the creation process. The temperature that the system reaches is based on numerous factors including the intensity of the current applied, the material being sintered, and the materials used to form the die, punch and foil coating of the powders being sintered. To finely control the temperature of the system a

K-type thermocouple is used to measure the thermal properties of the Die in nearly direct contact with the powder. A pyrometer may also be used to determine temperature based on the infrared light emitted from the system. This ensures the accuracy of the temperature measurement to limit the phase transitions from occurring in metallic glass creation when operating within the glass transition and crystallization temperature window.

3.5.1.1 Differential Thermal Analysis

In order to determine the ideal operating temperature for the creation of bulk metallic glasses the glass transition temperature and crystallization temperature must be finely measured. This is done through differential thermal analysis (DTA) which measures the change in heat flow to the sample, either endothermic or exothermic, as a function of temperature. When crystallization occurs from an amorphous system there is an exothermic event due to the structuring of the atoms to the more relaxed crystalline state. It is this temperature that is the crystallization temperature (T_x) and the process leading up to it in which the exothermic reaction begins that is used to identify the glass transition temperature (T_g). This is done through the use of Al_2O_3 as an inert substance in two chambers, each with the temperature under measurement by a thermocouple connected to a voltmeter. One containing only Al_2O_3 to act as a base point for comparison, the other with the sample contained within Al_2O_3 for reference. As the heat flows to the chamber containing both vials the one containing the sample will slightly alter the energy during the crystallization process, sending a minor deflection to the voltmeter connected to the thermocouples. This deflection is related to the energy of crystallization of the sample, yielding both the temperature at which it occurs and the energy needed. Selecting the appropriate temperature for SPS processing will allow for the glass transition to occur resulting in compaction and densification while remaining below the T_x to retain the amorphous structure.

3.5.2 SPS Dwell temperature

The highest temperature that the SPS system reaches during the sintering process is referred to as the dwell temperature. Through appropriate selection of this temperature

through the knowledge of the T_x and T_g of the system it is possible to select the ideal temperature at which to sinter. In addition to the correct temperature the dwell time is an important factor to consider. The time spent sintering at the dwell temperature is referred to as the dwell time and can allow for phase transitions to occur even below the crystallization temperature. As time dwelling increases the amount of energy put into the system rises allowing for localized crystallization to occur. This can form either nanocrystalline regions or a fully crystalline system if the dwell time is too long. Typical dwell times for amorphous BMG systems are in the range of a few minutes, far shorter than is typically possible in a hot press style system. To firmly establish the dwell time desired a Time-Temperature-Transformation (TTT) analysis done must be conducted on the samples to ensure the structure remained amorphous.

3.5.3 SPS Heating and Cooling rate

In addition to the dwelling temperature and time the heating and cooling rates for the SPS run must be considered. Due to the nature of the SPS heating method it is possible to rapidly heat and cool the system through rapid application or removal of the current flow. There still remains some dispute on the impact of the heating and cooling rate's influence on the densification of the system. This influence was investigated and the impact is minimal with further analysis shown later in this work. Despite minimal influence the main objective in controlling the heating rate is to ensure limited grain growth while avoiding current spikes causing localized heating to occur.

3.5.4 SPS Pressure

The application of pressure during the sintering process serves a twofold benefit to the creation of a compact system. The pressure applied first allows for the rearrangement of the particles to a more condensed arrangement and clears the agglomerates. The second function is in the addition of a driving force for sintering given by the relation shown in equation 25.

$$\frac{d\rho}{(1-\rho)dt} = B \left(g \frac{\gamma}{x} + P \right) \quad (25)$$

where ρ is fractional density, B is Diffusion and temperature factor, g is the geometrical constant, γ is the Surface energy, t is time, and P is the pressure applied. The influence of pressure on the compaction of the disk is related to the particle size in question. At smaller sizes the influence of pressure is diminished while at larger particle sizes the pressure can distort and fill vacancies [44]. The influence of pressure versus densification is demonstrated in Figure 3.9 for a ZrO_2 sample.

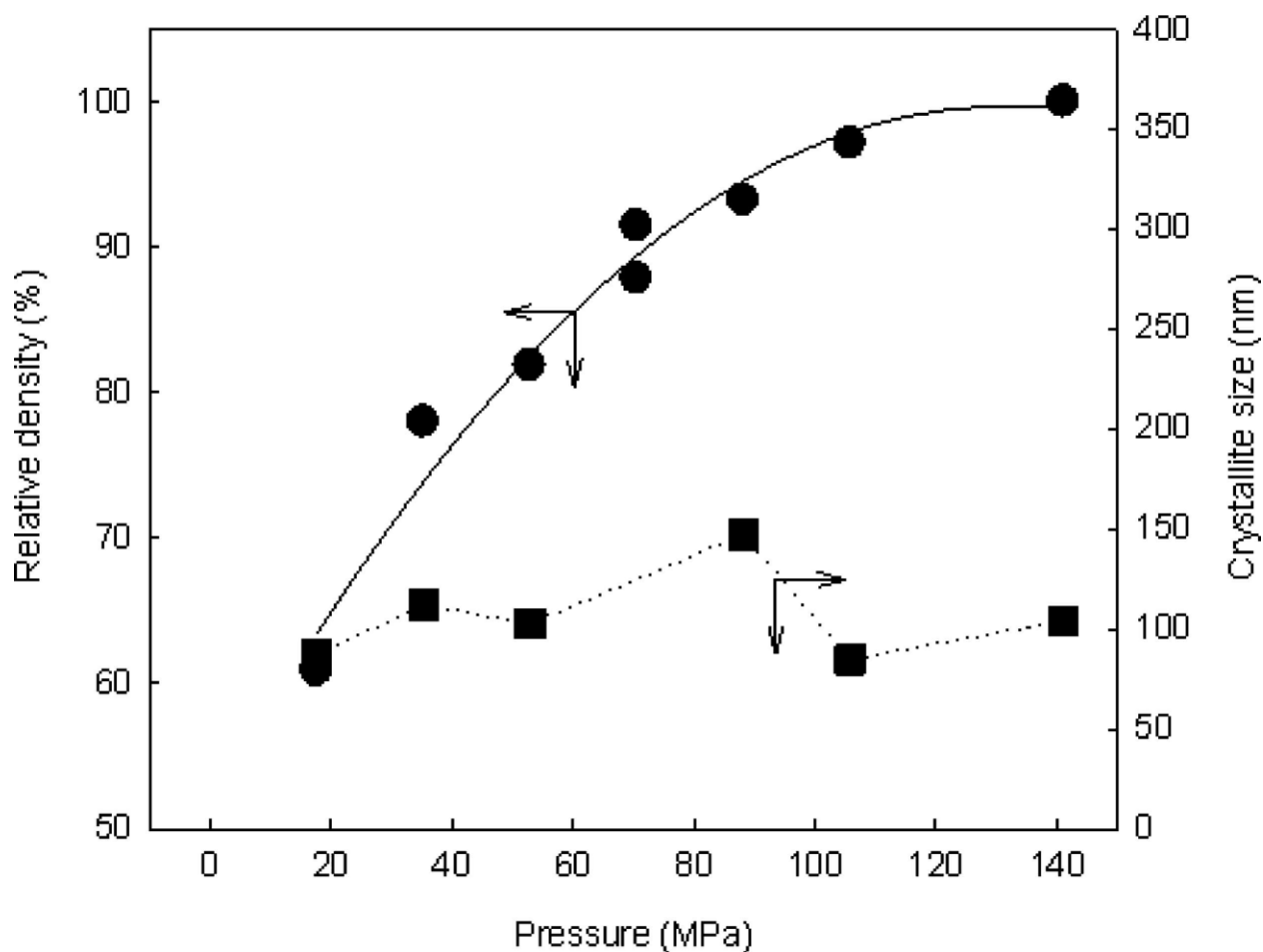


Figure 3.9-Compaction density as a function of pressure and particle size for ZrO_2 in SPS[44]

The rate of application of pressure plays a very minor role dependant more on when the pressure is applied rather than the rate at which it increases. Application near room temperature allows for more compact powders reducing the sparks present jumping from particle to particle. Application near the glass transition temperature allows for a reorganization to occur when the atoms are in a more liquid state enabling pores to be filled. The results obtained in varying heating and pressure rates demonstrate little influence on the final density of the system, though this may be more due to user error on a minor influential component of densification.

3.6 Spark Plasma Sintering synopsis

The main goal of the SPS method in the creation of BMG systems is in the retention of the amorphous structure of the nanopowder while accomplishing densification into a bulk system. This is achieved through the dwelling temperature above the glass transition T_g while remaining below the crystallization temperature T_x . Higher pressure and dwell time are selected to ensure reorganization of the atoms to create a nonporous system without returning to a crystalline state. In some cases small amounts of nanocrystalline structure was allowed and encouraged to obtain a denser system with higher hardness while retaining the majority of the benefits of an amorphous system. In addition to controlling the crystallization and compaction contamination must also be prevented. This was done through isolation of the powder in Tantalum foil 0.025mm thick above and below the powder, separating it from the punches. In addition to this a second coating layer of graphite foil was present surrounding the Tantalum foil to aid in the preservation of the punch and die system and inhibit bonding between the foils and the SPS equipment.

In addition to control of crystallization and phase transformations the compaction level of the created disk is of high importance. This can be shown through many BMG systems such as $Zr_{55}Cu_{30}Al_{10}Ni_5$ by Xie *et al.* [47, 48]. The importance of compaction level is demonstrated through their results comparing the as cast rod to two distinct samples with dramatically different porosity levels. Through minimization of porosity the overall strength of the material rises dramatically while porous samples are easily fractured. This is demonstrated in Figure 3.10 showing compressive stress versus strain.

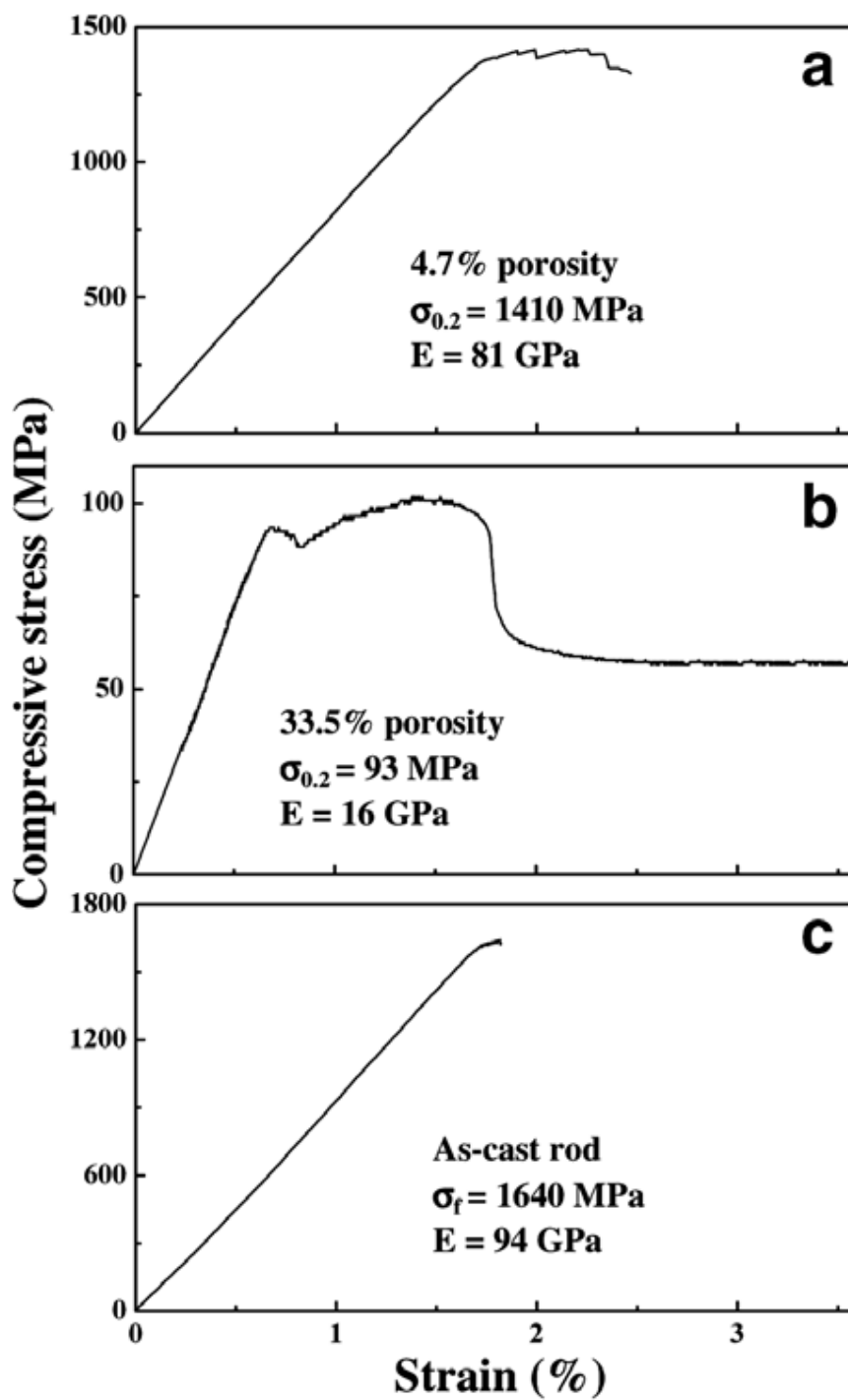


Figure 3.10- Compressive stress versus strain for $Zr_{55}Cu_{30}Al_{10}Ni_5$ demonstrating importance of high compaction and low porosity in BMG creation [47]

3.7 Spark Plasma Sintering sample preparation

In the creation of BMG through the Spark Plasma Sintering system there are numerous factors that need to be determined before reliable high quality samples can be created. This involves the knowledge of the glass and crystallization temperatures, the strength of the sample, and the crystallization rate at a given temperature. To establish this it is often required to first perform a Differential Thermal Analysis (DTA) on sample of the powder to establish the desired temperature at which the system may be compacted. Knowing the strength of the system, while not essential, allows for the pressure needed for compaction to be estimated. Typical SPS systems are run using a set of graphite punches, dies, and spacers which can only withstand a pressure of 60 MPa before fracturing may occur. Through the use of alternate punch and die materials such as Inconel 718 (superalloys) or tungsten-carbide it is possible to reach pressures in excess of 1000 MPa before fracturing may occur. It is important to keep the dwell temperature of the system in mind when selecting the material for the system as fracturing may occur at a far lower pressure at higher temperatures. A rough rule for the creation of our BMG systems is if the dwell temperature is below 800C WC punch and die systems may be used carefully but at temperatures beyond this graphite is the only reliable system that can withstand both the temperature and pressure required. The tools used as well as the parameters for the SPS system are described for each system created with a focus on the benefits and costs of that particular method. These procedures were refined and adjusted to optimize the compaction, crystalline nature, and strength of the created BMG system.

3.7.1 Ball Milling

The early work into the creation of Bulk Metallic Glass systems under the Spark Plasma Sintering device focused on the use of amorphous powders synthesized through mechanical alloying. Mechanical alloying is a method of creating amorphous powders through high energy ball milling, a process in which small spheres are contained along with the elemental powders within a vial. The vials are then subject to rapid motion (with the motion style and intensity subject to the ball mill used) which allows for high energy impacts of the balls on the elemental powders. This milling allows for the elemental powders to alloy together at relatively low temperatures and mix the atomic

structure. The time and energy required to alloy the elemental powders into an amorphous system is heavily dependent on a set of factors including the charge ratio (the mass ratio of the balls used in the mill to the combined mass of the elemental powders) and the milling device used. There are two commonly used milling methods planetary and shaker . Planetary ball milling involves the rotation of the vial around a central axis to impact the balls on the powder as the vial rotates around the central axis as well as on its own vertical axis as shown Figure 3.11 [49]. The shaker ball mill has the same vial setup as the planetary ball mill but shakes the vials in a figure eight pattern in three dimensions. This allows for numerous impacts between the balls, powder, and vial enabling rapid milling due to high energy chaotic motion.

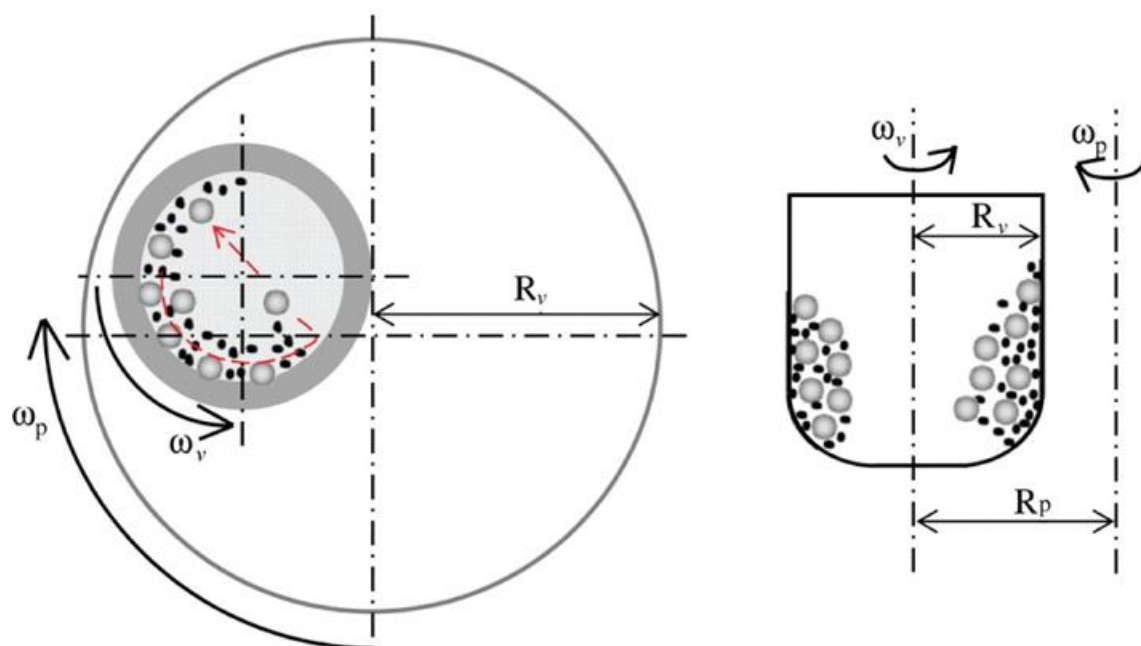


Figure 3.11- Ball mill vial rotation diagram[49]

For this work the primary milling method used was the shaker method using the SPEX 8000D ball milling device. The milling time was varied based on the composition under investigation typically using two larger and four smaller balls with diameters of 12.7 mm and 6.35mm respectively within the vial 7.62 cm in height and 5.76 cm in diameter all constructed of 8007 SPEX stainless steel. This was typically done on 8 grams of elemental powder yielding a charge ratio of 3:1. The vials were all sealed

inside an argon filled glove box to minimize the oxidation risk and aid the amorphous transition and final composition remained intact.

3.7.2 Melt Spinning

In order to create amorphous systems through quenching the metallic liquid faster than the critical cooling rate the melt-spinning process was used. This involves the creation of crystalline metal ingots through arc melting and shattering to produce small metallic shards. These shards are then placed within small quartz tubes with a small ejection hole near at the bottom of the tube, typically 0.5-0.8 mm in diameter. The system is evacuated down to below 30 mTorr and refilled with Argon or Helium gas to ensure contamination free environment. The metal is then induction melted and ejected onto by pressurized Argon or Helium onto a copper wheel experiencing a cooling surface in excess of 30 m/sec. This allows for cooling rates in the range of 10^4 - 10^7 K/sec allowing the system to be critically cooled and the amorphous structure preserved. This process creates metallic ribbons and in the use of our system in excess of 1 meter length and 5 mm width. These systems were then analyzed using X-ray diffraction and Vickers hardness tests to determine strength and structure. Compositions that retained the amorphous nature and exhibited high hardness on the Vickers scale were selected as potential candidates for further investigation. The wheel and induction coil are shown on Figure 3.12 with a long cylinder to contain the ribbons to the left of the wheel.

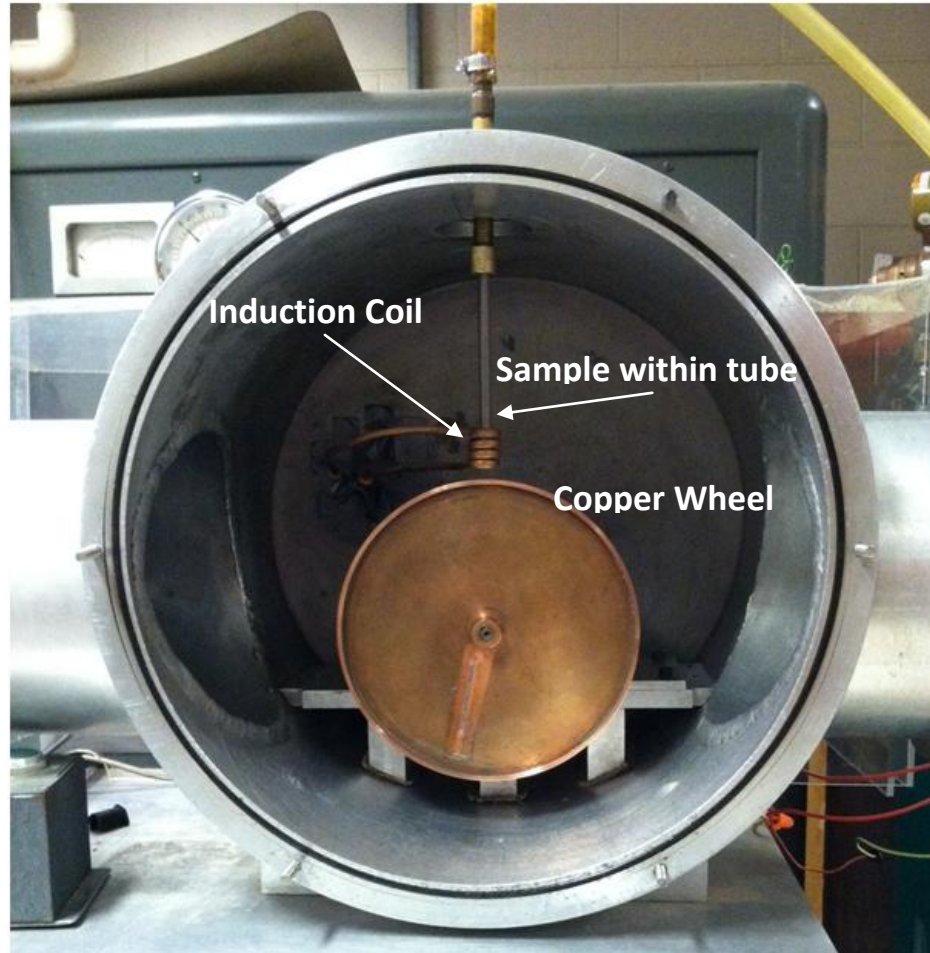


Figure 3.12- Melt Spinner system for creation of amorphous metallic ribbons.

3.8 Vickers Hardness

In order to obtain the hardness of the system in question Vickers hardness measurements were conducted. This method involves the use of a square-based pyramid diamond to create indents in the material under investigation. The angle of the pyramidal diamond tip is set at 22° allowing the indents to remain the same shape and style across multiple runs and systems. This allows for equation (26) to be used to determine the hardness of the material based on the force applied and the diagonal length of the indent created by the diamond where F is the force applied, A is the area of the indent, and d is the diagonal length of the indent.

$$HV = F/A \approx 1.891F/d^2 \quad (26)$$

Chapter 4

Experimental Results

4.1 WCoB metallic glass systems

The primary focus of this BMG research was on the creation of alloys that were highly dense, exhibited a high hardness value, maintained a limited ductility, and remained fully amorphous. Early BMG research was done of systems that enabled easier access to amorphous phases through rapid quenching such as Zr, Fe, or Rare Earth elements such as Ds or Pr. The advantages of these systems lay in the ease with which they formed amorphous structures through quenching or milling, but the shear and bulk moduli of these systems were often too low for application in the desired field. To counter this early work was done on Tungsten based systems to discover compositions that could form amorphous structures while retaining the strength and density of Tungsten. To select the elements to pair with the core element phase diagrams were frequently consulted to find the optimal atomic ratio that, energetically, yield the most stable compound. When consulting the phase diagram for Iron-Boron as shown in Figure 4.1 the guideline for selecting the ideal composition is based on the system creation method. If quenching from liquid the ideal composition is at the eutectic points (such as 17% atomic Boron) while when mechanically alloying the ideal location is at the peak energy between eutectic points (such as 50% atomic Boron). This distinction between "ideal" compositions based on the creation method is the ease with which the structures are disassembled and the energy required to reassemble the perfect crystalline lattice.

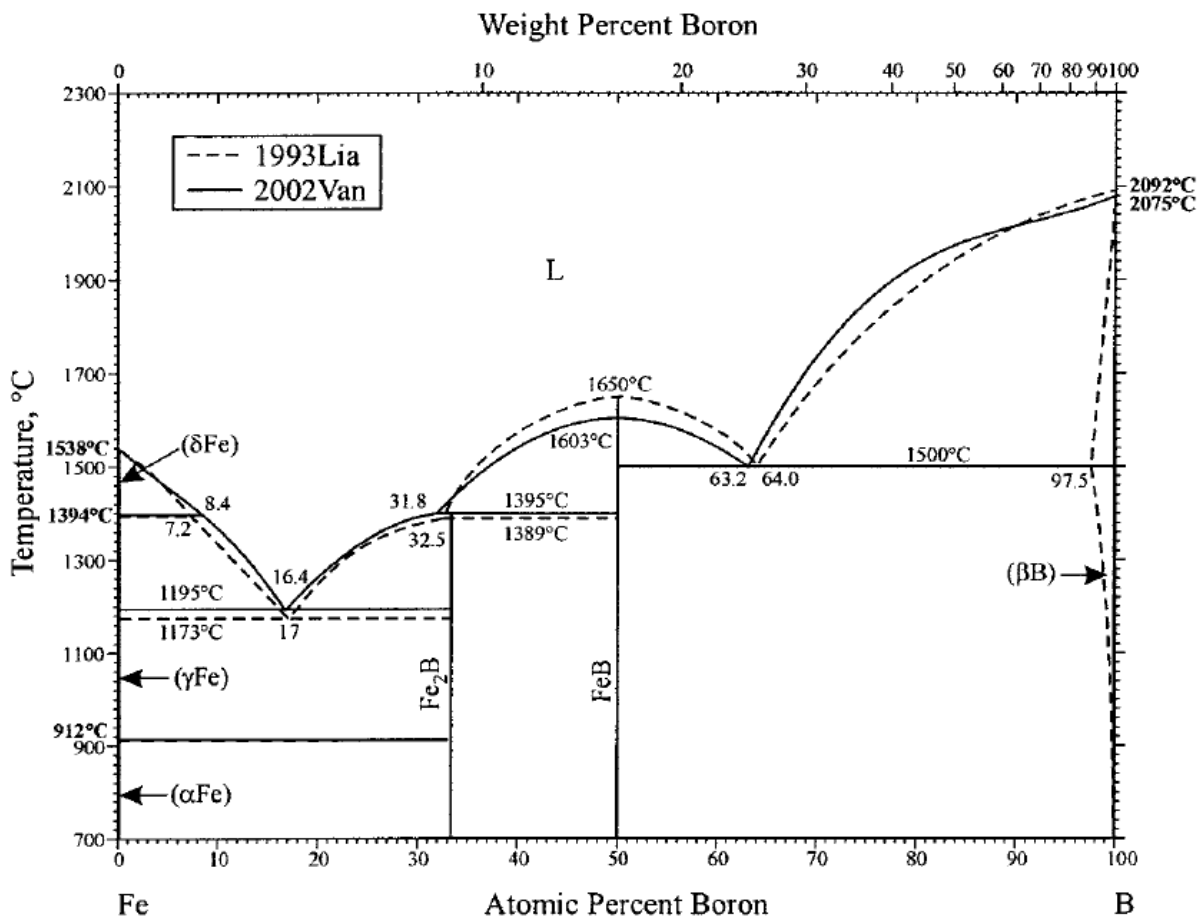


Figure 4.1- Phase diagram of Fe-B binary [50]

In order to select the ideal composition several distinct alloys were created, each through mechanically alloying under the shaker ball mill using 8007D SPEX stainless steel vials and balls. In order to determine the ideal system the first hurdle to overcome was if the composition could truly form an amorphous structure. This was verified through the milling of the desired composition followed by X-Ray diffraction (XRD) of the powder. Amorphous systems, due to their lack of a defined structure, lack the identifying peaks typically found through diffraction of incident X-rays onto a crystalline system. The less defined the peak the more disordered the structure of the system, allowing for a rough rating of the amorphous nature of each particular system. This method enables selection of alloys before any further action is taken on a particular system, with the XRD patterns of select compositions as well as the time milled present in Figure 4.2.

W systems- XRD Plots

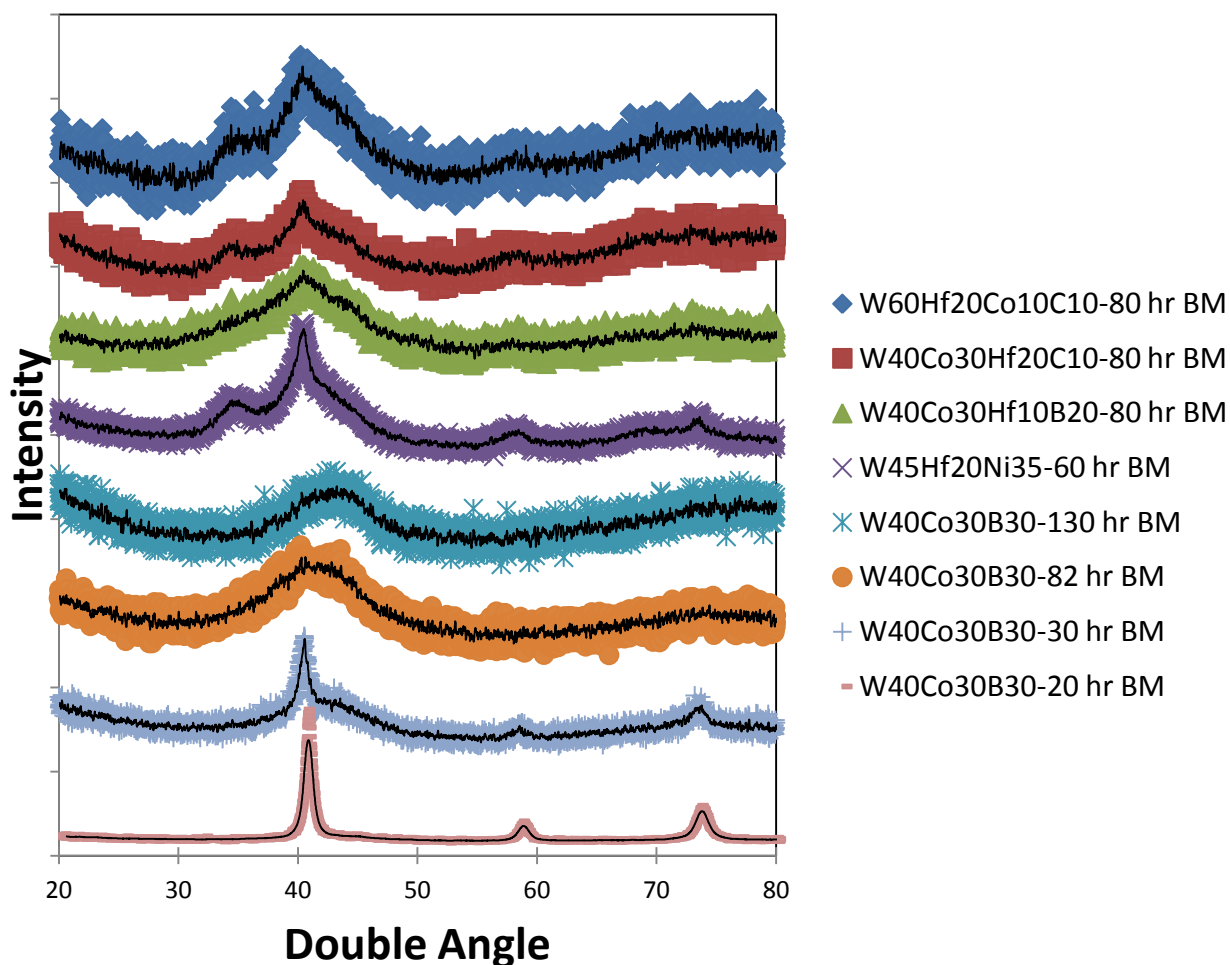


Figure 4.2- X-Ray Diffraction diagram of W-based ball milled systems

The peak location at 40.2° is indicative of (011) Tungsten showing the lack of fully amorphous structure or full integration of Tungsten within the system. As the system becomes more disordered the Tungsten peak begins to spread, as shown through the progression of $W_{40}Co_{30}B_{30}$ for 20, 30, and 82 hour Ball Milling (BM) times. By this 82 hour point the system no longer has a defined W peak allowing for the claim that the system is "XRD amorphous" in that the system can no longer identify any defined crystalline structure. It is systems that have reached this point that were further investigated for their potential to create BMG systems under the SPS process.

Once selected for their amorphous forming capability the alloys created through mechanical alloying were subject to further investigation under Differential Thermal Analysis (DTA) and Energy-Dispersive X-Ray Spectroscopy (EDS) to determine the temperature at which they recrystallized as well as the actual composition of the alloy. EDS is done through the excitation of the electrons present in the sample, allowing for electrons to move from a lower energy state to vacant bands. The return to the stable lower energy state releases X-rays with specific frequencies allowing for the identification of the atoms present in the sample based on the frequencies collected as well as the composition ratio based on the overall intensity ratios. Through this it is possible to determine the composition of the system following the mechanical alloying process, as well as any contamination obtained through the process. For Tungsten systems the contamination level during the shaker milling process was high due to the high hardness values of elemental Tungsten when compared to stainless steel. This resulted in contaminations in excess of twenty atomic percent Iron during the 82 hour milling process. The contamination level was varied based on the vial and ball composition used, as well as the system undergoing mechanical alloying. In an attempt to counter this a surfactant, Dodecane, was used to coat the powders and alleviate the contamination. The contamination levels are shown in Figure 4.3 for the $W_{40}Co_{30}B_{30}$ base system under distinct milling conditions. Four distinct methods were used, control being 2 large (12.7mm diameter) and 4 small (6.35 mm diameter) stainless steel balls in a stainless steel vial. The addition of Dodecane served to increase the contamination level, replacement of stainless steel balls with Tungsten Carbide served to reduce the Iron contamination at the cost of Carbon and Tungsten contamination. This contamination level was linked to dramatic density adjustments for the systems created as well as distinct elastic property changes once the systems were SPSed into compact disks.

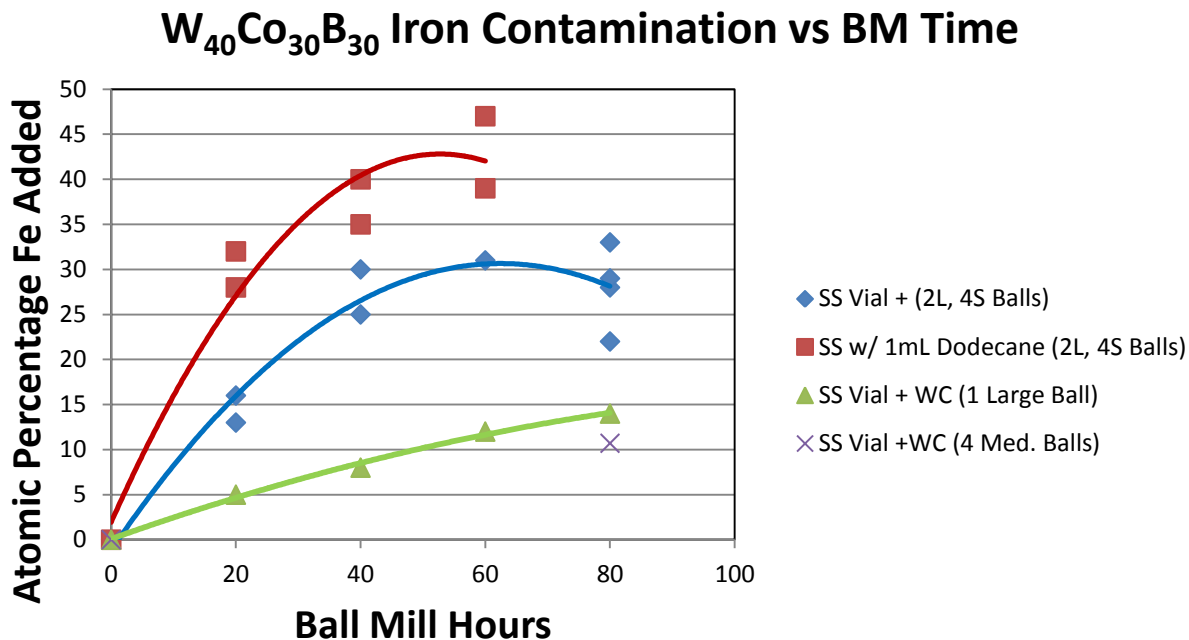


Figure 4.3- Iron contamination during ball milling for W-based systems

Beyond simply altering the elastic properties of the disks the crystallization temperature of the system was altered. In Figure 4.4 a DTA run for $W_{40}Co_{30}B_{30}$ adjusted to $W_{33}Co_{25}B_{25}Fe_{17}$ to account for the contamination level. This yielded a crystallization temperature (T_X) value of 718C with similar DTA curves being present for each sample under investigation. A collection of DTA and EDS results combined to show influence of Iron contamination on W-based system crystallization temperature is shown on Figure 4.5.

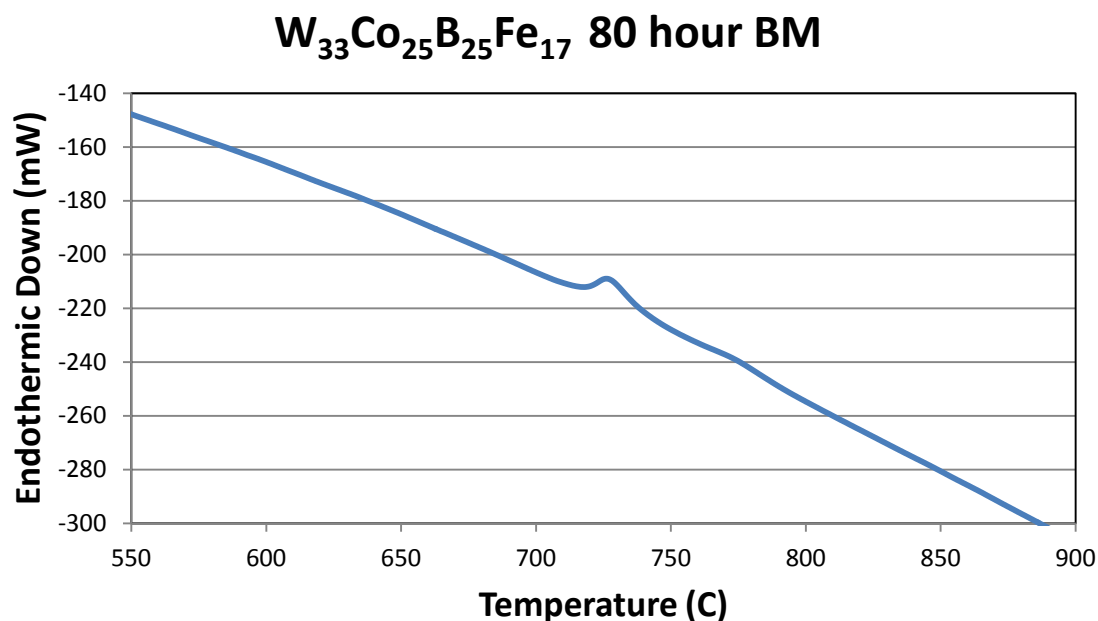


Figure 4.4- Differential Thermal Analysis on $W_{40}Co_{30}B_{30}$ base system post milling.

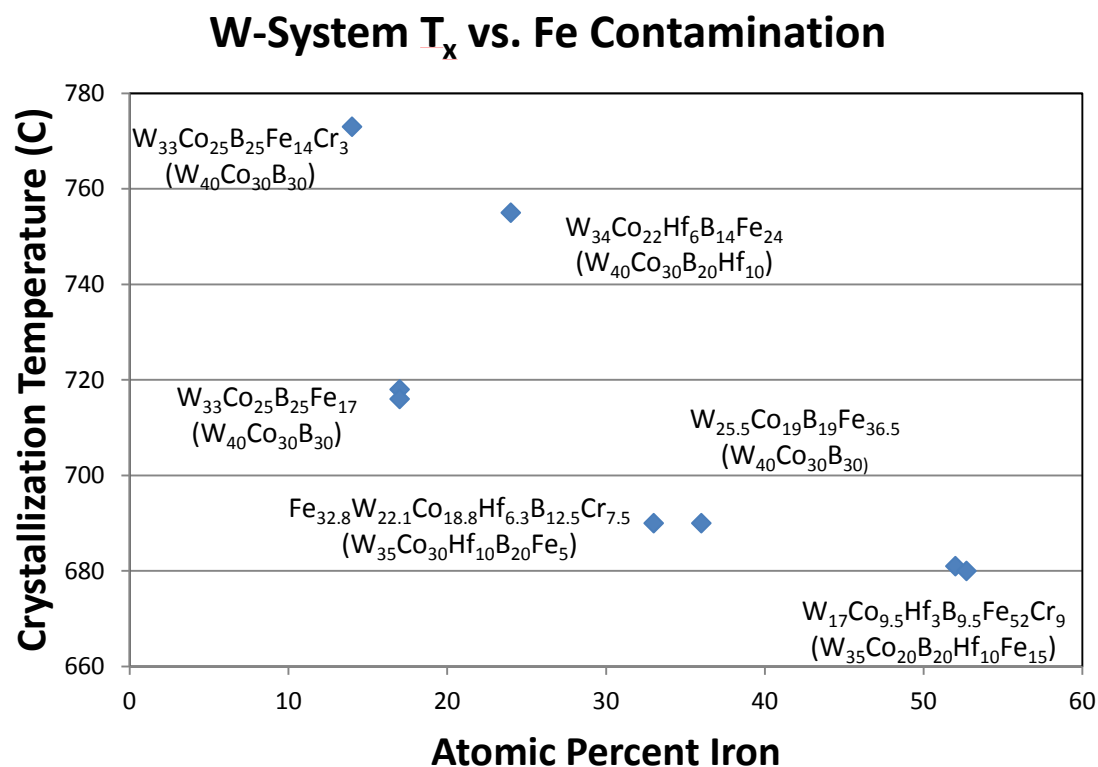


Figure 4.5-DTA results for W-systems showing T_x decrease due to Fe contamination

Once DTA was conducted on a powder sample and a crystallization temperature established SPS parameters could be constructed. This involved the selection of the dwell temperature, pressure applied, current and pressure rates, as well as the time for dwelling at peak temperature. The data presented in Table 4.1 demonstrates each of the listed properties used to create the systems. The experimental results of density and hardness are shown in Table 4.2 with the experimental density of the disk measured through the Archimedes method and the theoretical density calculated an atomic fraction weighted reciprocal sum average of the elemental densities. The percentage value of experimental compared to theoretical is a good first estimate of the porosity of the disk and is an accurate gauge to demonstrate the compaction of the powder into a solid disk.

Table 4.1- Experimental parameters of SPS creation of BMG Tungsten Alloys

Sample System Ideal State- EDS measured State	BM Time	Dwell Temp.	Pressure Applied	Dwell Time (mins)	Pressure and Temperature rates
$W_{40}Co_{30}B_{30}$ - $W_{25.5}Co_{19}B_{19}Fe_{30}Cr_{6.5}$	80 Hours	630C (T_x 680C)	500 MPa	7.5	Pressure then Temp
$W_{40}Co_{30}B_{30}$ - $W_{25.5}Co_{19}B_{19}Fe_{30}Cr_{6.5}$	80 Hours	660C (T_x 680C)	575 MPa	7.5	Pressure then Temp
$W_{40}Co_{30}B_{30}$ - $W_{23}Co_{16.5}B_{16.5}Fe_{36}Cr_8$	130 Hours	630C (T_x ~680C)	50 MPa until 540C, then 500 MPa	9	100 MPa/min 20 C/min At trigger temp
$W_{35}Co_{20}Fe_{15}Hf_{10}B_{20}$ - $W_{17}Co_{9.5}B_{9.5}Hf_3Fe_{52}Cr_9$	80 hours	660C (T_x 681C)	100 MPa until 620C, then 575 MPa	7	250 MPa/min 25 C/min At trigger temp
$W_{35}Co_{20}Fe_{15}Hf_{10}B_{20}$ - $W_{17}Co_{9.5}B_{9.5}Hf_3Fe_{52}Cr_9$	80 hours	660C (T_x 681C)	100 MPa until 620C, then 575 MPa	7	300 MPa/min 25 C/min At trigger temp
$W_{40}Co_{30}B_{30}$ - $W_{33}Co_{25}B_{25}Fe_{17}$	80 hours	690C (T_x 718C)	100 MPa until 660C, then 575 MPa	7	300 MPa/min 25 C/min At trigger temp
$Fe_5W_{35}Co_{30}Hf_{10}B_{20}$ - $Fe_{32.8}W_{22.1}Co_{18.8}Hf_{6.3}$	80 Hours	670C (T_x 690C)	100 MPa until 640C, then 575 MPa	7	275 MPa/min 20C/min At trigger temp
$W_{40}Co_{30}B_{30}$ - $W_{25.5}Co_{19}B_{19}Fe_{30}Cr_{6.5}$	80 Hours	670C (T_x 690C)	100 MPa until 630C, then 575 MPa	7	200 MPa/min 15C/min At trigger temp

Table 4.2- Experimental and Theoretical properties of BMG Tungsten Alloys created through SPS compaction

Sample System Ideal State- EDS measured State	Hardness (GPa)	Experimental Density (g/cc)	Calculated Density (g/cc)	Relative Density- Exp/Calc
$W_{40}Co_{30}B_{30}$ $W_{25.5}Co_{19}B_{19}Fe_{30}Cr_{6.5}$	9.2	9.8	11.74	83%
$W_{40}Co_{30}B_{30}$ $W_{25.5}Co_{19}B_{19}Fe_{30}Cr_{6.5}$	9.1	10.3	11.74	88%
$W_{40}Co_{30}B_{30}$ $W_{23}Co_{16.5}B_{16.5}Fe_{36}Cr_8$	8.83	10.6g	10.7	98%
$W_{35}Co_{20}Fe_{15}Hf_{10}B_{20}$ $W_{17}Co_{9.5}B_{9.5}Hf_3Fe_{52}Cr_9$	11.4	10.41	10.6	98%
$W_{35}Co_{20}Fe_{15}Hf_{10}B_{20}$ $W_{17}Co_{9.5}B_{9.5}Hf_3Fe_{52}Cr_9$	9.6	10.19	10.6	96%
$W_{40}Co_{30}B_{30}$ $W_{33}Co_{25}B_{25}Fe_{17}$	9.7	10.14	13.0	78%
$Fe_5W_{35}Co_{30}Hf_{10}B_{20}$ $Fe_{32.8}W_{22.1}Co_{18.8}Hf_{6.3}$	8.57	11.2	11.65	96.1%
$W_{40}Co_{30}B_{30}$ $W_{25.5}Co_{19}B_{19}Fe_{30}Cr_{6.5}$	9.3	10.6	11.74	90%

Through the creation of the W-base BMG disks the density of the system reflected the Iron contamination level both in numerical value and compaction level. Through the addition of Iron contamination the Tungsten systems were able to create amorphous structures at the cost of hardness and density. The compaction level is evident under optical imaging of the disks once polished using 4000 Grit (6 micron) SiC sandpaper. The images shown in Figure 4.6 are for $W_{19}Co_{13}B_{13}Fe_{48}Cr_7$ SPSed under 630C using 500 MPa of pressure. The compaction level is ~98% with a density of 10.4 g/cc as demonstrated by the small number of pores and their size on the scale of a few microns.

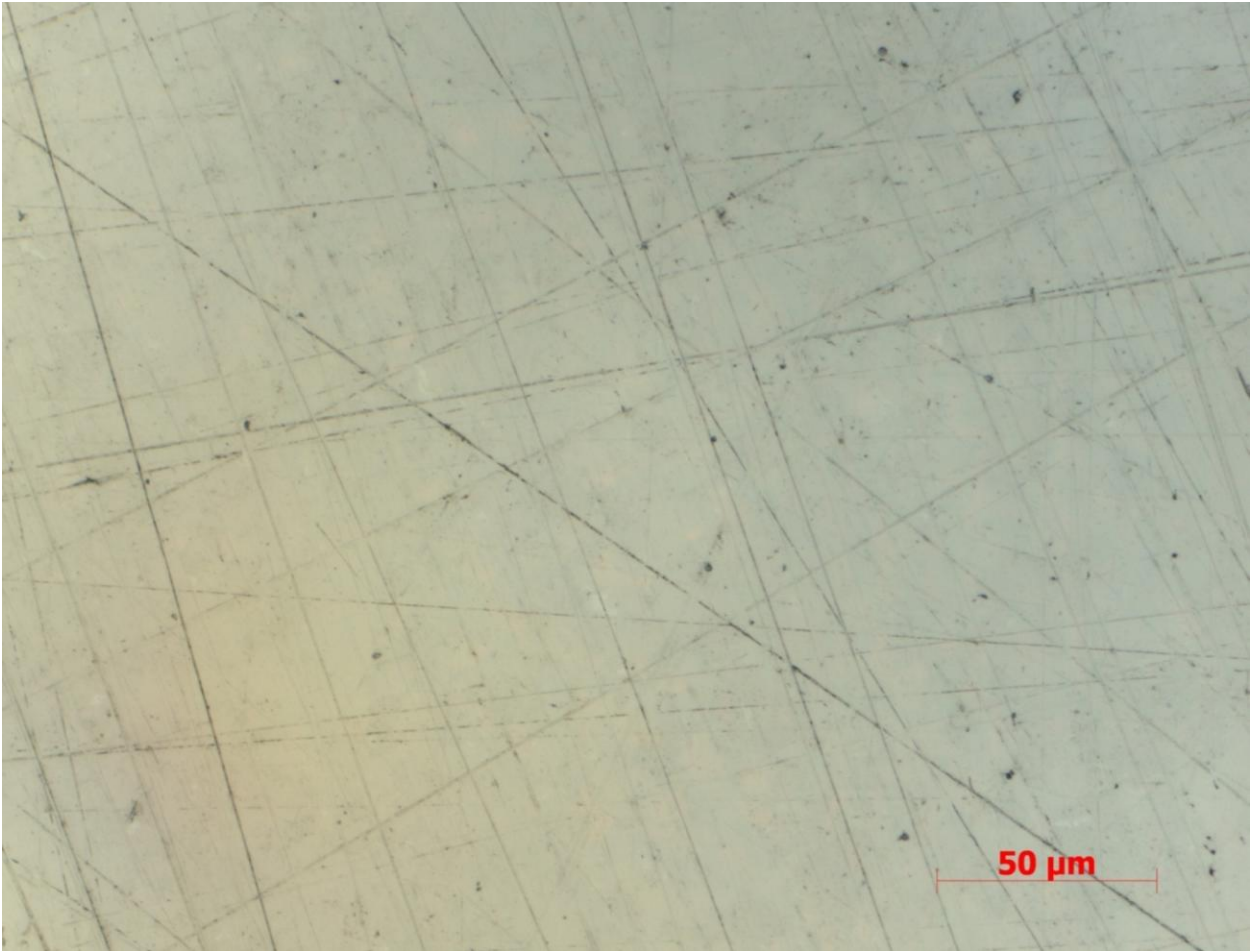


Figure 4.6- $W_{19}Co_{13}B_{13}Fe_{48}Cr_7$ SPS disk images using optical microscope

At first glance the samples created with compaction levels in excess of 98% appear strong the presence of any pores dramatically limits the capabilities of the system as a whole. When subject to stress test the pores serve as fracture points allowing the system to decompose when subject to only a few hundred MPa as opposed to the desired strength in excess of 2-3 GPa. Given the porosity and iron contamination of the Tungsten alloys resulting in lower density, low hardness (below 10 GPa on the Vickers scale), and inability to reproduce any specific run due to semi-random contamination levels the Tungsten alloy systems were halted due to difficulty in producing reliable systems.

4.2 NiCoTa metallic glass systems

With the primary focus of this BMG work being the creation of systems with high density, high hardness, and relatively high ductility while retaining the amorphous properties expected of a BMG the W-based systems were no longer highly viable. The Iron contamination played the role of lowering the hardness and density while allowing for the amorphous structure to be created for Tungsten systems. Due to this the primary element of the system was shifted to a focus on transition metals of Nickel and Cobalt due to their relatively high hardness and density values. The compositions were then adjusted to increase the density and strength of the materials while remaining amorphous. Early work was done through the use of shaker ball milling with the composition and milling time playing critical roles in determining if the system was capable of reaching a fully amorphous state. Select compositions are shown in Figure 4.7 below through the use of 15 hours of shaker ball milling time in the SPEX 8000D model using 8007D stainless steel.

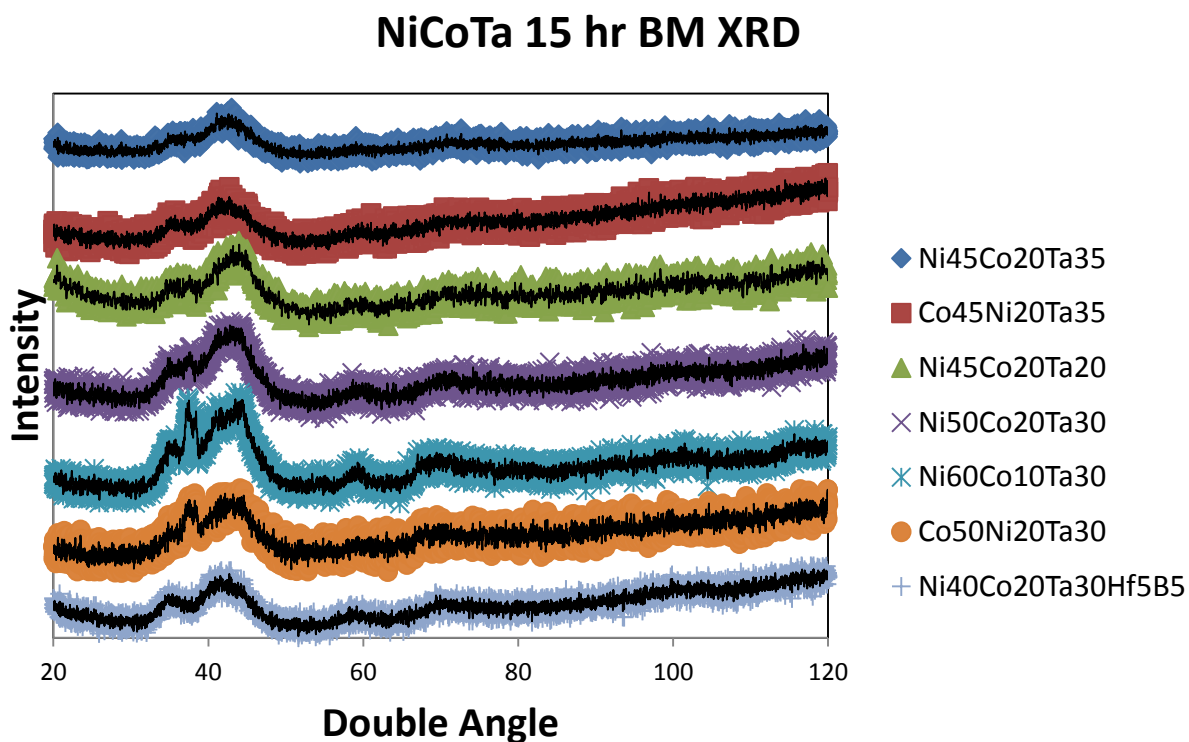


Figure 4.7- X-ray diffraction on select NiCoTa based systems milled for 15 hours

The selection of 15 hours for milling time was done following work on progressively longer milling time on a $\text{Ni}_{45}\text{Co}_{20}\text{Ta}_{35}$ system as shown in Figure 4.8. This demonstrates the small window in which the system appears amorphous under the XRD scan.

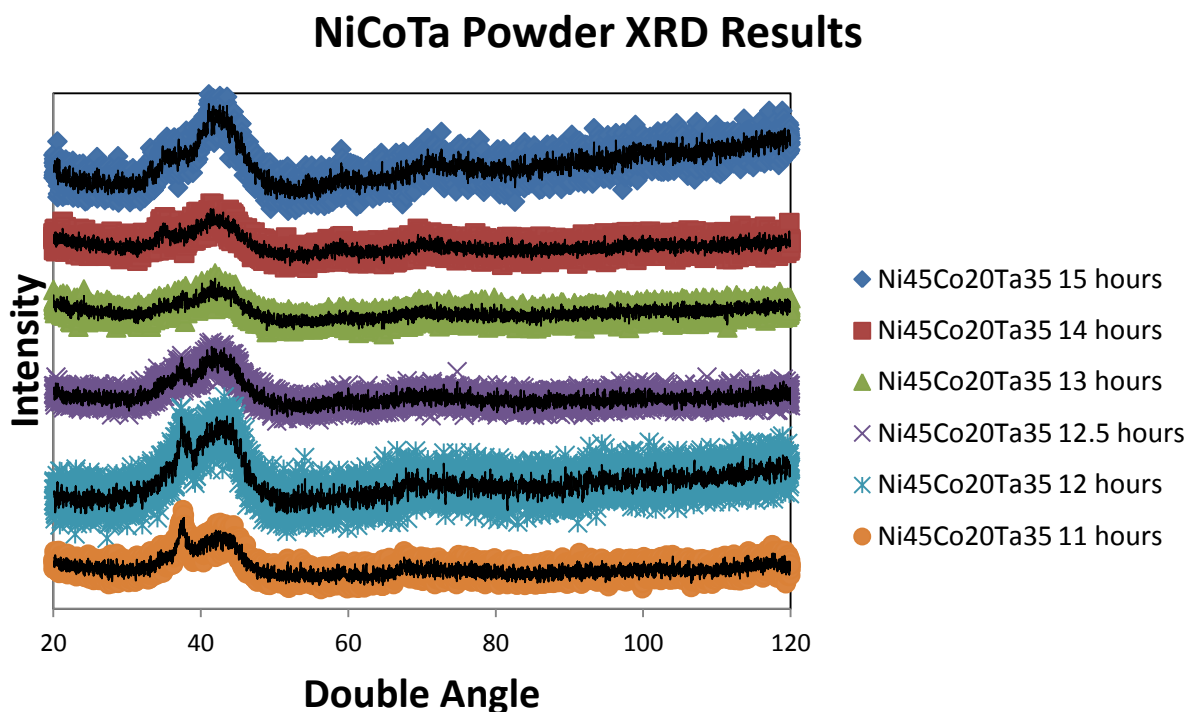


Figure 4.8- X-ray diffraction on $\text{Ni}_{45}\text{Co}_{20}\text{Ta}_{35}$ ball milled systems at various times

The presence of a small shoulder on the amorphous hump in the 30-40° double angle window was indication that the structure was never perfectly amorphous, merely masking crystalline growth in the nanometer size regime. This was verified through TEM imaging of SPS disks made using this powder despite initial powder and SPS disk demonstrating identically amorphous XRD patterns.

Due to the structures forming during the milling process mechanical alloying demonstrated that this method of creating an amorphous system with a NiCoTa composition was difficult. To combat this an alternate style of creating an amorphous structure was selected. Beyond mechanical alloying rapid quenching or shock cooling the liquid metallic system remained a potentially viable method of creating large amounts of amorphous systems. This was done through the combination of arc melting the

elemental ingots into a combined homogeneous ingot which was then melt spun into amorphous ribbons. A demonstration of a ribbon set is shown in Figure 4.9.



Figure 4.9- Demonstration of typical melt spun ribbons, shown is $Ni_{45}Co_{10}Ta_{25}Nb_{20}$

Once a collection of amorphous ribbons was made the next process needed was to create a powder system capable of sintering in the SPS system. This involved a return to the ball milling process to fracture the ribbons into small particles. In an effort to minimize the Iron contamination and still achieve systems consisting of powders the charge ratio was never in excess of 8:1 balls to ribbons with a desired ratio of 4:1 or 3:1 if possible. A milling time cap of 2 hours was set to withhold the contamination level to under 1% atomic Iron. The powders were then compacted and sintered under the SPS system using methods similar to those listed in the Tungsten section. DTA analysis and EDS were performed on select runs with DTA results for a typical $Ni_{45}Co_{20}Ta_{35}$ to

determine the T_x and Iron contamination level. Dwell temperature selected as well as density and hardness results for select NiCoTa style systems are shown in Table 4.3

Table 4.3- Experimental results for early SPS BMG Alloys

System (SPS Dwell Temperature)	Hardness (GPa)	Experimental Density	Theoretical Density	Ingot Precursor Density	Relative Density (SPS/Precursor)
Ni ₄₅ Co ₂₀ Ta ₃₅ (T _{dwell} 690C)	7.57	12.27 g/cc	12.56 g/cc	12.89 g/cc	95.2%
Ni ₄₅ Co ₂₀ Ta ₃₅ (T _{dwell} 735C)	13.73	11.13g/cc	12.56 g/cc	12.89 g/cc	86.3%
Ni ₄₅ Co ₂₀ Ta ₃₅ (T _{dwell} 735C)	12.30	12.28g/cc	12.56 g/cc	12.88 g/cc	95.3%
Ni ₄₀ Co ₂₀ Ta ₃₅ B ₅ (T _{dwell} 680C)	6.83	10.7 g/cc	12.55 g/cc	12.8 g/cc	83%
Ni ₄₅ Co ₁₅ Ta ₃₅ Nb ₅ (T _{dwell} 680C)	6.44	10.27 g/cc	12.44 g/cc	12.6 g/cc	81.5%
Ni ₄₅ Co ₁₀ Ta ₂₅ Nb ₂₀ (T _{dwell} 688C)	13.5	11.00 g/cc	11.30 g/cc	11.46 g/cc	96.0%
Ni ₄₅ Co ₁₀ Ta ₂₅ Nb ₂₀ (T _{dwell} 675C)	12.9	10.49 g/cc	11.30 g/cc	11.34 g/cc	92.5%
Ni ₄₅ Co ₁₀ Ta ₂₅ Nb ₂₀ (T _{dwell} 680C)	13.1	11.15 g/cc	11.30 g/cc	11.31 g/cc	98.6%

Despite a higher measured numerical density Ni₄₅Co₂₀Ta₃₅ systems often had less than desirable compaction percentages as demonstrated by optical images as shown in Figure 4.10. To counter this, additional steps were undertaken to achieve higher

compaction levels without crystallization occurring through temperature adjustment or Iron contamination through extend milling time.

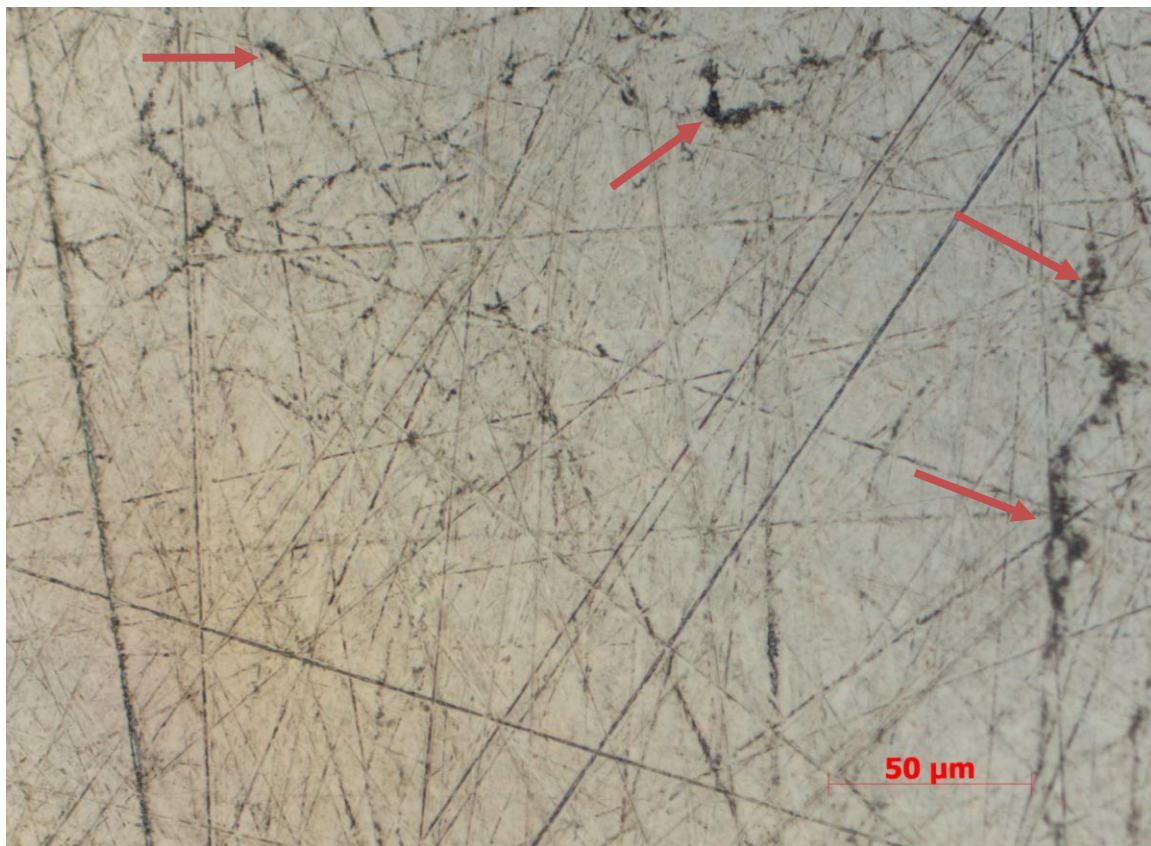


Figure 4.10- Optical image of $Ni_{45}Co_{20}Ta_{35}$ SPS disk created via milled melt spun ribbon. Red lines demonstrate porous regions.

To counter the porosity smaller powder size was desired as the filling fraction is related to the distribution and size of the particles used. In an effort to decrease particle size without extended milling time the ribbons were annealed to embrittle the ribbons due to their highly ductile nature. This was done through sealing the ribbons within quartz crystal tubes containing an Argon atmosphere. The tubes were then placed inside a furnace and heated to within 50C of the crystallization temperature for a dwell time of only a few minutes. The tubes were then rapidly quenched in water and the ribbons extracted. The annealed ribbons were then ball milled for the similar 2 hour time in the shaker mill resulting in far smaller particles. To verify that no crystallization occurred during the process XRD scans were performed on ribbons before and after the annealing process with results shown in Figure 4.11. Crystallization occurred during the annealing

process for ribbons in excess of 690C so a cap was set at 680C, or 70C below crystallization temperature of 753C for $Ni_{45}Co_{20}Ta_{35}$, in an effort to ensure amorphous structures were preserved.

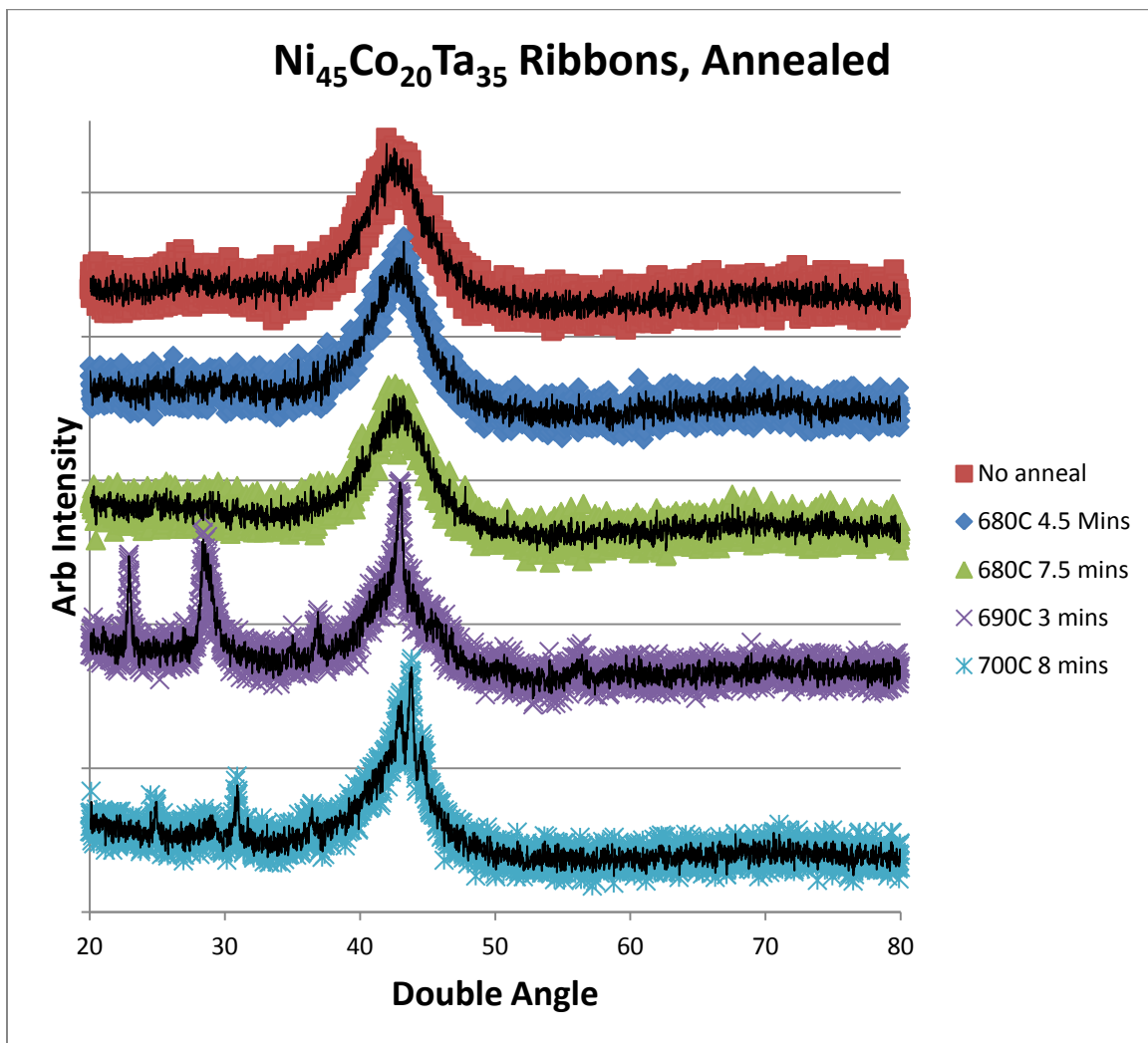


Figure 4.11- X-ray diffraction of $Ni_{45}Co_{20}Ta_{35}$ ribbons at various anneal times and temperatures

Once annealed and milled the systems were SPSed in an effort to create more compact disks. XRD results of the disks created using annealed ribbons is shown in Figure 4.12 to demonstrate the amorphous nature preservation. A temperature 735C sintering is shown for comparison and demonstration of crystallization during SPS process. The crystallization peaks are all due to isolated Tantalum excluded from the amorphous structure.

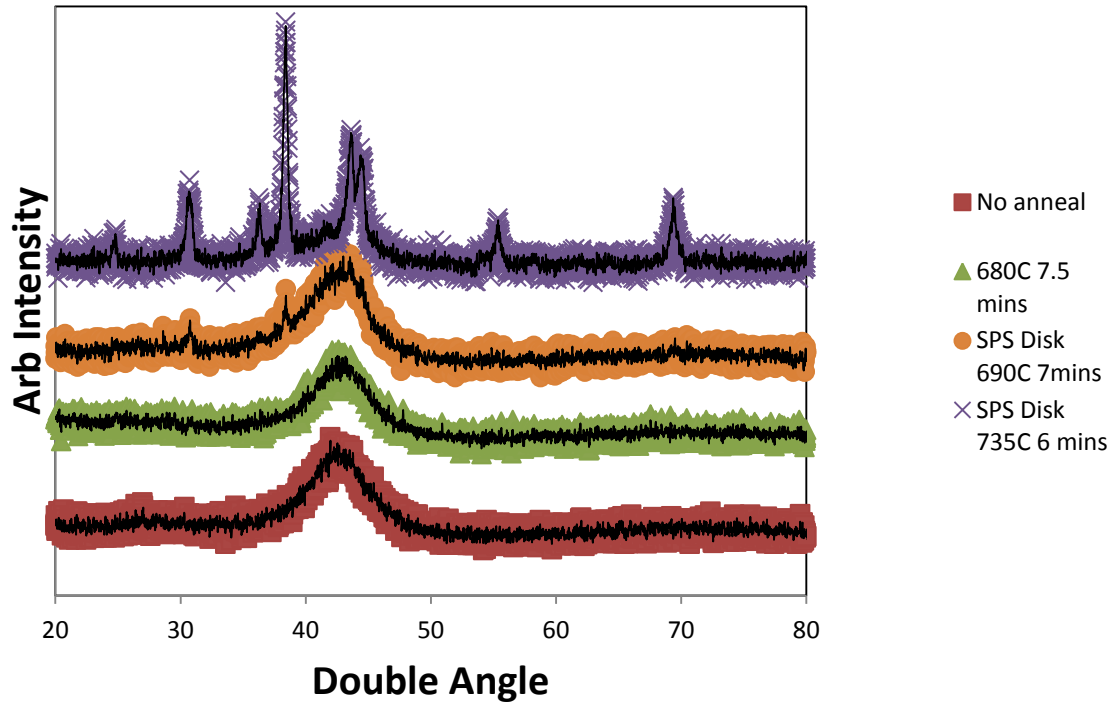


Figure 4.12-X-ray diffraction of $Ni_{45}Co_{20}Ta_{35}$ ribbons and disks once SPSed

Despite this annealing the compaction levels of the disks never exceeded 98% due to limitations on the SPS system used at this point. The punch and die system were comprised of Tungsten Carbide with 3% Cobalt. This system allowed for 575 MPa of pressure with a safe temperature cap of 690C before plastic deformation and fracturing occurred in the system. This limited the approach to the crystallization and glass transition temperatures and inhibited compaction. To counter this a combination of two steps were taken: replacement of the WC system with a 10% doped cobalt which increased the viable temperature at the cost of increased risk of damage done to the punch and die system and adjustment of the crystallization temperature through the composition change to NiCoTaNb.

4.3 NiCoTaNb metallic glass systems

The transition to $Ni_{45}Co_{10}Ta_{25}Nb_{20}$ was done in an effort to compensate for the limitations of the SPS equipment in place of problems present in the NiCoTa system as a

potential BMG system. Due to limitations at 575 MPa of pressure and 690-700C as the safe dwelling temperature the desire to dwell within 25-30C of the crystallization temperature at the glass transition temperature a transition had to be made. Through the use of DTA the crystallization temperature of $\text{Ni}_{45}\text{Co}_{10}\text{Ta}_{25}\text{Nb}_{20}$ was found to be 708C with a minor crystallization range from 620C-660C as shown in Figure 4.13. This first range primarily consisted of Ni-Nb crystallization and did not rapidly occur during SPS, allowing for amorphous structures to be maintained in nearly each sintering.

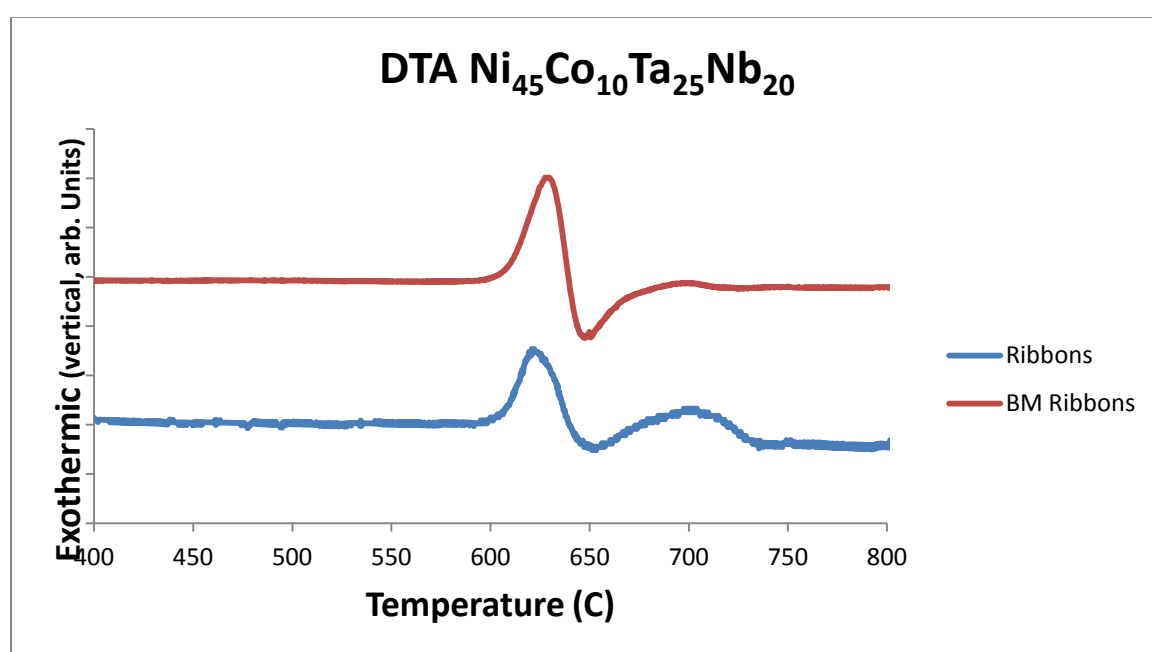


Figure 4.13- DTA results on $\text{Ni}_{45}\text{Co}_{10}\text{Ta}_{25}\text{Nb}_{20}$ ribbons

To reach the desired 100% compaction while retaining the desired properties the particle size of the powders used was measured and adjusted to determine the influence this had on the compaction. This was done through a combination of sifting the ball milled powders and verification of the size/shape of the powders through SEM imaging. Powders were created by shaker milling melt spun ribbons of the NiCoTaNb amorphous system maintaining a 6:1 ratio of stainless steel balls to ribbons. Demonstration of the particle size and distribution is shown in Figure 4.14 with a combination of powders in excess of 100 μm and many below 53 μm (smallest filter applicable to powders). In order to optimize compaction the proper ratio and size of particles had to be obtained.

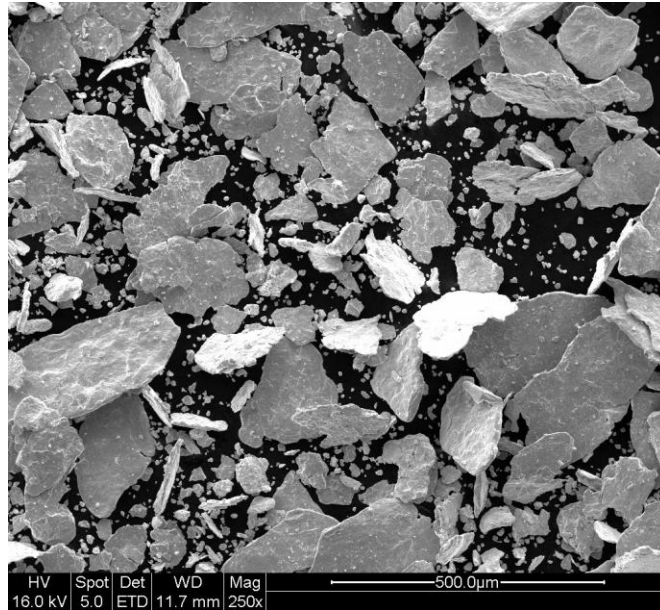


Figure 4.14- SEM imaging of ball milled NiCoTaNb ribbons

In order to maintain a focus on only one factor the $\text{Ni}_{45}\text{Co}_{10}\text{Ta}_{25}\text{Nb}_{20}$ was SPSed using the same conditions of 575 MPa, a dwell time of 7 minutes at a temperature of 680C, pressure and temperature being increased in tandem, and the same punch, die, and foil configuration. This ensured minimal uncertainty as to the cause or compaction changes when comparing the results of each experimental configuration. The dwell temperature of 680C was selected as a baseline through early SPS runs in which crystallization was observed through XRD on the sintered disks, as shown in Figure 4.15.

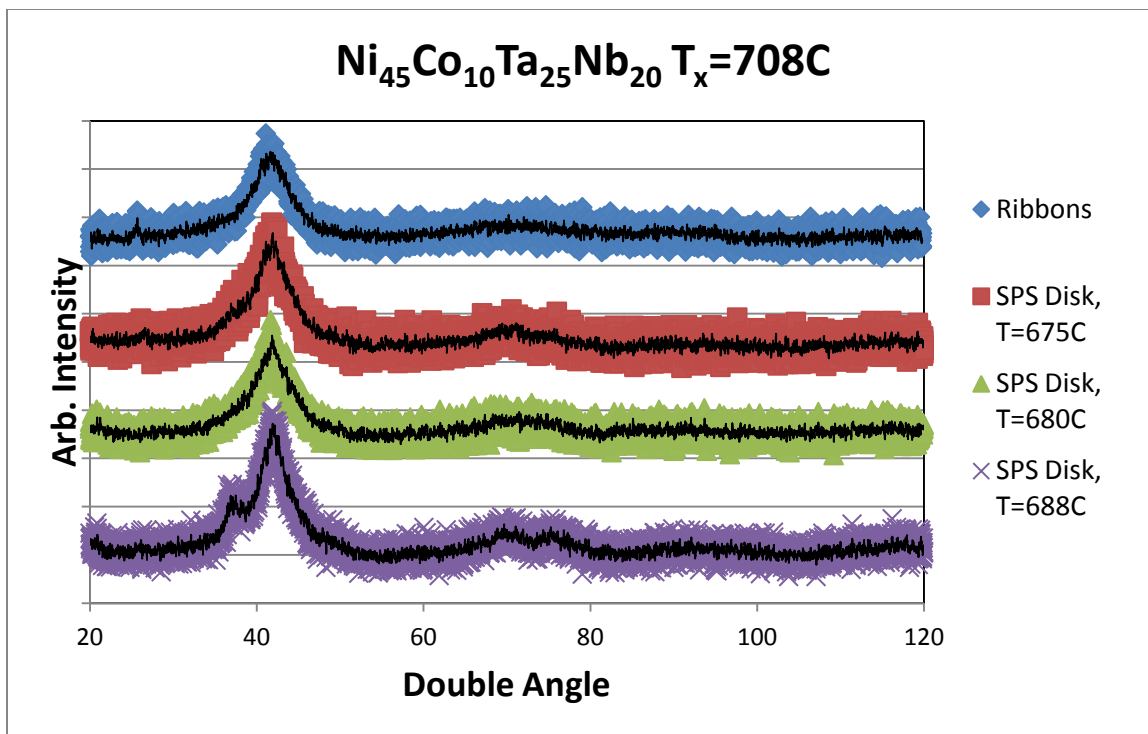


Figure 4.15- X-ray diffraction of Ni₄₅Co₁₀Ta₂₅Nb₂₀ SPS disks made using milled ribbons

With the temperature, pressure, and method selected the optimization of the powder size was done through determination as to what was obtainable and the compaction level reached during SPS. Early work consisted of 2 or 3 powder filtrations compared with systems that underwent no filtration for comparison. To demonstrate the impact of powder filtration two systems are shown in Figures 4.16-4.19. SPS 43 was done using a mass ratio of 43%-33%-24% of particles in the size ranges of 0-53 μ m, 53-74 μ m, and 74-106 μ m respectively. SPS 44 was done using a mass ratio of 40%-60% of particles in the size ranges of 0-53 μ m and 74-106 μ m respectively.

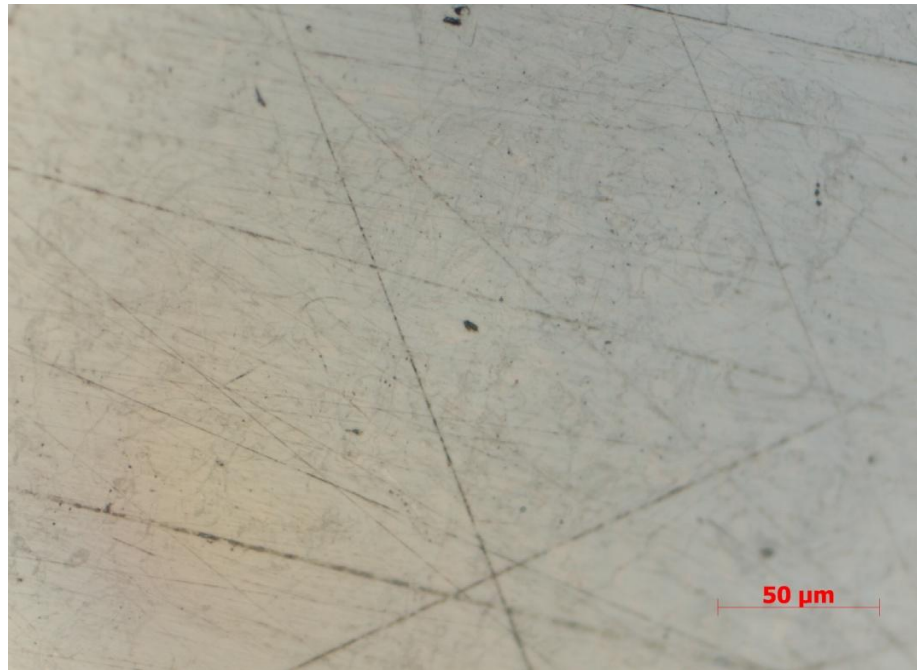
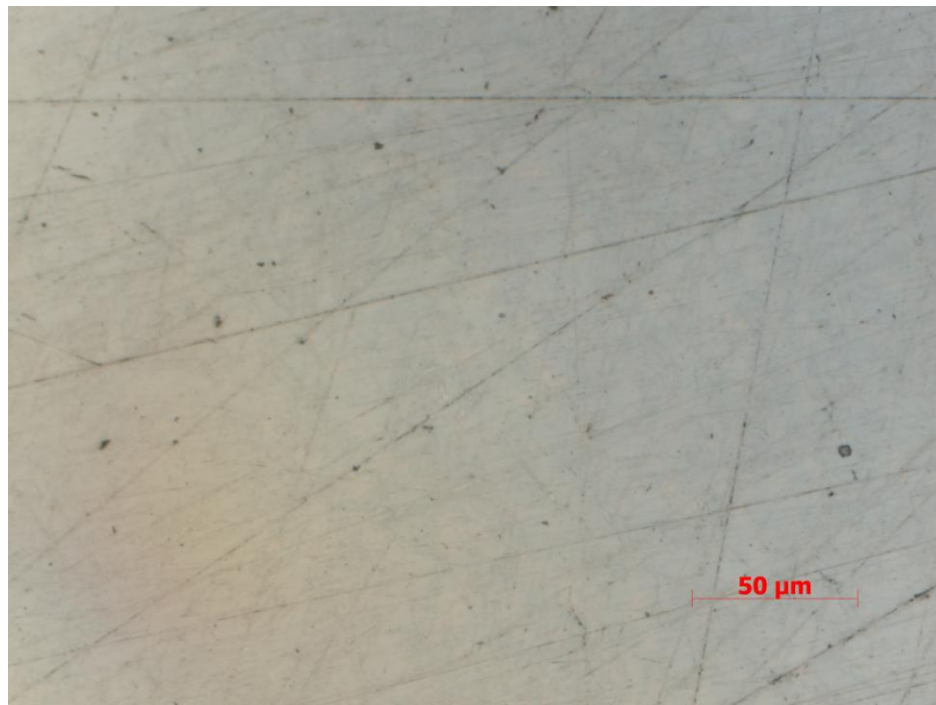


Figure 4.16 (above)- SPS 43 optical image of polished surface

Figure 4.17 (below)- SPS 44 optical image of polished surface



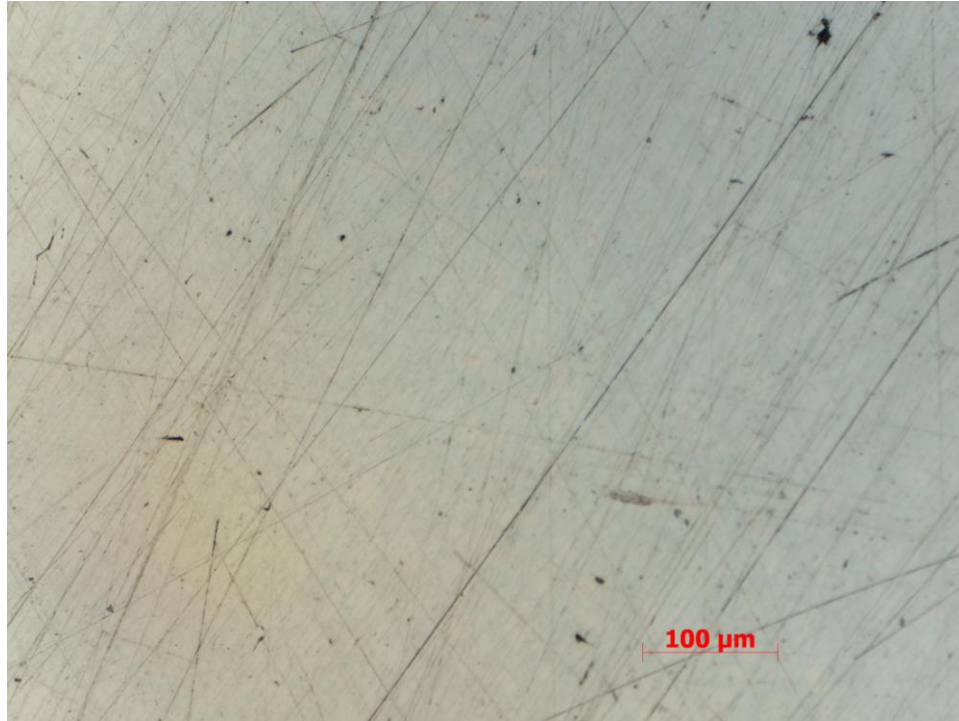
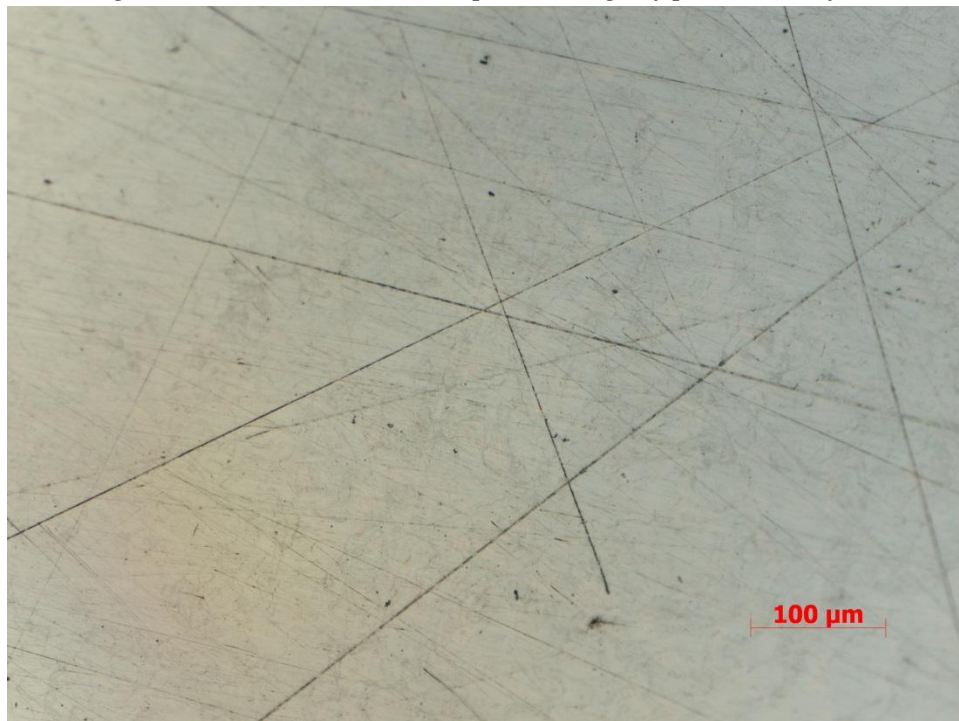


Figure 4.18 (above)- SPS 43 optical image of polished surface

Figure 4.19 (below)- SPS 44 optical image of polished surface



Both disks achieved a high compaction compared with NiCoTa and WCoB based systems, in excess of 98% in the case of SPS 44. This was done while retaining the amorphous natures of the system and a density of 11.05 g/cc with a maximum hardness of 13.7 GPa with an average of 12.9 GPa. While compact and dense the final 1-2% compaction was still desired as the pores present in the system still prevented high compression test results due to fracturing linking the pores and cracking the system. To further increase the compaction powder size optimization coupled with increased pressure during sintering was used. This involved replacement of WC-3Co with WC-10Co to increase the pressure applicable to 1 GPa and an increase in dwell temperature range to 800C before fracturing occurred.

At this point pressure was increased on each run to 1000 MPa with dwell temperature and grain size distribution as independent variables for compaction optimization. Two paths were taken to optimize compaction and retard crystallization, one to manipulate the dwell temperature to control the desired amount of nano-crystal growth within the system and the other being particle size through annealing of the ribbons and milling time. Through dwelling temperature it became possible to partially crystallize the system, increasing the compaction dramatically and allowing for pores to be filled. This is demonstrated through SPS 102 in which the ribbons were milled for a total of 14 hours yielding an Iron contamination level of 33% atomic. Through extension of milling time the average particle size fell to 15 μm allowing for high compaction to occur. This decreased the numerical density to 9.33 g/cc with a hardness of 13.71 GPa but allowed for nearly perfect compaction as shown through images of the SPS disk in Figure 4.20.



Figure 4.20- Optical images of SPS 102 exhibiting nearly perfect compaction. Note: small "pore" on the right is a microscope lens scratch.

This came at the cost of crystallization as SPS 102 was sintered at 690C resulting in 50-50 ratio of nano-crystalline and amorphous NiCoTaNb as shown in Figure 4.21. The peaks present are due to Ni-Fe and Nb-Fe crystallization and sparked interest in minimizing the Iron contamination through reduction of milling time. In order to optimize the compaction the particle size and Iron contamination had to be minimized while remaining below the crystallization temperature and time in order to preserve the amorphous nature of the system. The primary challenge to this optimization was in the decrease in obtained particle size was tied to ball milling time which is directly related to Iron contamination level. In order to accelerate fracturing during the milling process annealing was done on ribbons of NiCoTaNb and XRD performed. Post-annealing and milling the system remained amorphous but when subject to identical SPS conditions crystallization occurred as demonstrated in Figure 4.18 for SPS 131. This demonstrated

the risk of nano-crystallization during the process of annealing, milling, and SPS that remains hidden under XRD until sufficient energy is provided to the system. This nano-crystal growth was countered through combinations of annealed and non-annealed ribbons in an effort to optimize particle size and minimize Iron contamination. This is demonstrated through SPS 133 and 134 which combined 90-10 and 70-30 ratios respectively of non-annealed and annealed ribbons. Within SPS 133 the non-annealed powder used was only the particles that were filtered to below 53 microns in size while in SPS 134 the ratio was 40% 106-74 μm , 30% <53 μm , and 30% <53 μm annealed. This resulted in compactions in excess of 99% with nearly perfect amorphous XRD spectrums as shown in the same Figure 4.21.

To summarize the results shown in Figure 4.21 the crystallization present in SPS systems 101, 102, 103, 106, and 131 are due to all of these systems using high or exclusively powder from annealed ribbon or longer milling time. This decreased size caused crystallization under conditions that previously had yielded XRD amorphous disks. This is indicative that the XRD amorphous systems may not be purely amorphous but consist of large collections of nano-crystals with size below detection by this X-ray system.

In addition to the powder size ratios composite systems were attempted using Ni_8Ta powders obtained through milling. This created strained FCC structure nanoparticles to replace the annealed powder in SPS 133 and 134 systems. This resulted in SPS 145 a $\text{Ni}_{45}\text{Co}_{10}\text{Ta}_{25}\text{Nb}_{20}$ system 6mm thick, 63.5mm² cylinder sample with 60-30-10 ratio of <53 μm , 53-106 μm , and Ni_8Ta powders respectively. High compaction was achieved using this method as shown in Figures 4.22 and 4.23 with the density of 11.26 g/cc.

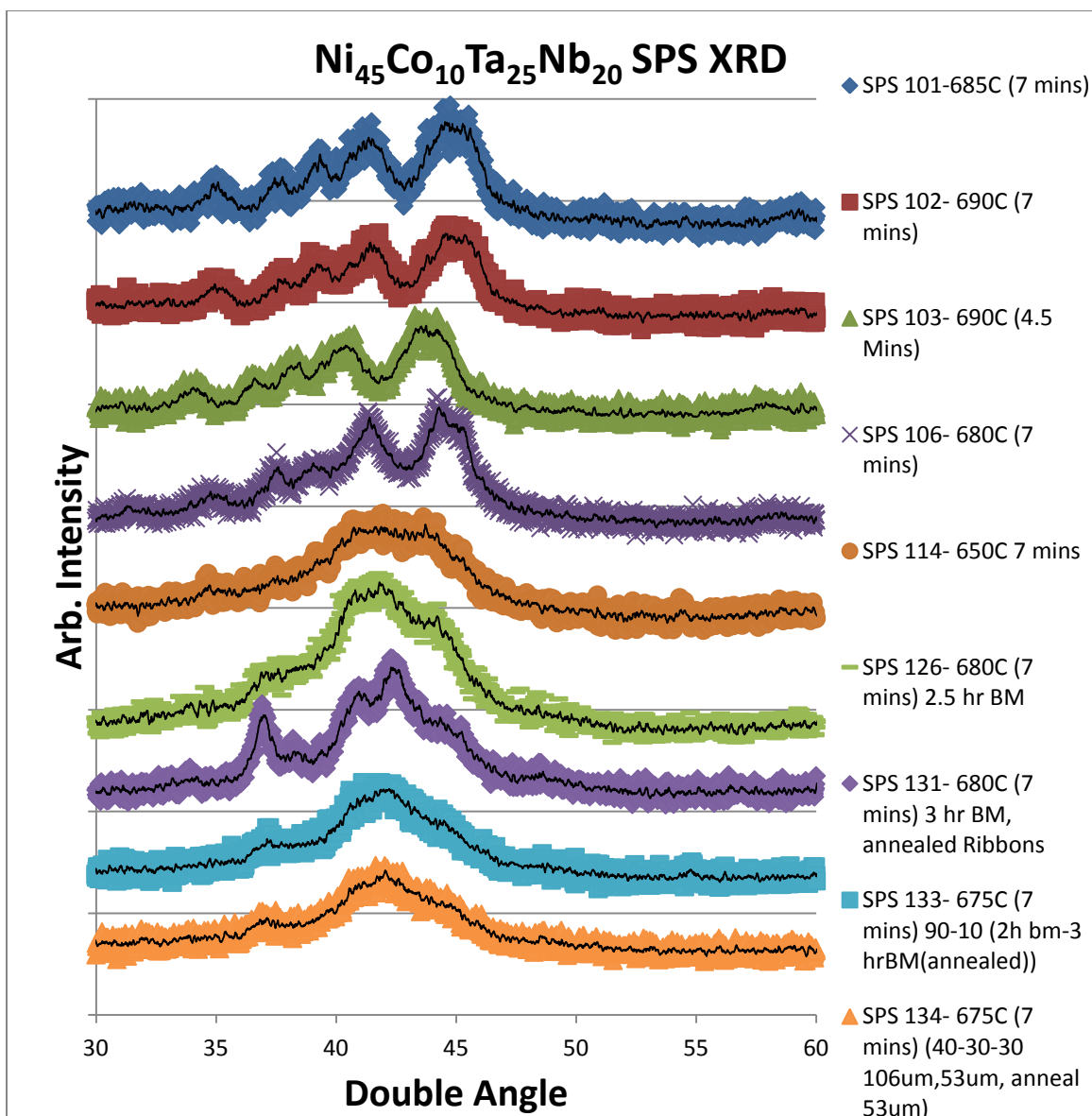


Figure 4.21- X-ray diffraction compilation of $Ni_{45}Co_{10}Ta_{25}Nb_{20}$ systems under distinct creation methods. Impact of particle size demonstrated in SPS 101, 102, 106 and 131 due to crystallization.

Due to the XRD amorphous nature of the SPS 126, 133 and 134 systems further investigation was done into what allowed these systems to remain amorphous when scanned by the system yet reach high levels of compaction as demonstrated by Figures 4.22-4.25. A table summarizing the experimental properties of select samples is shown in Table 4.4.

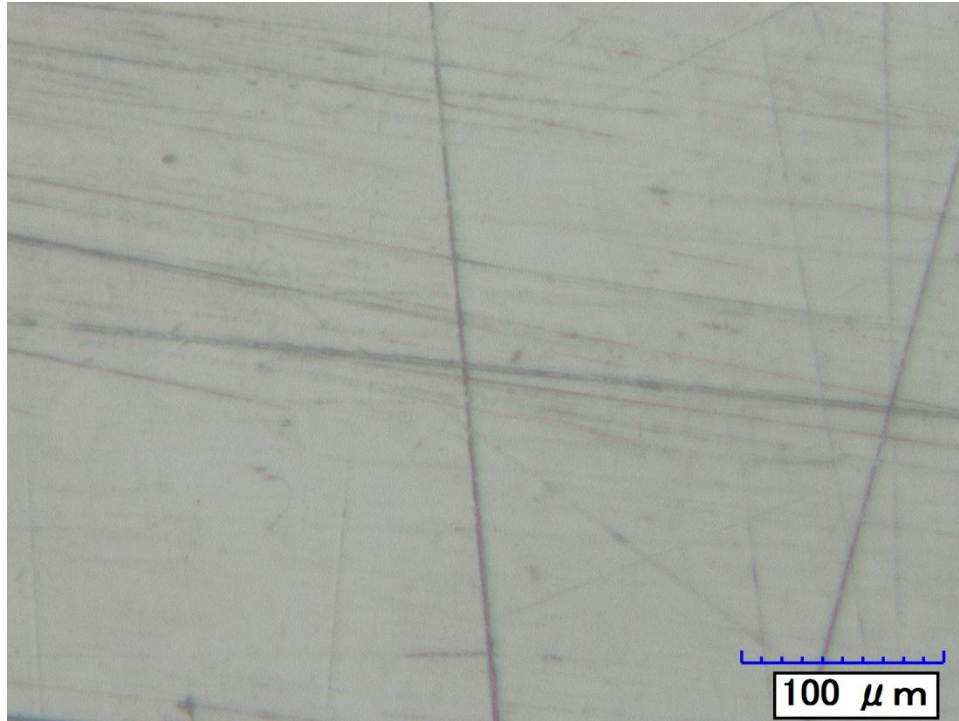
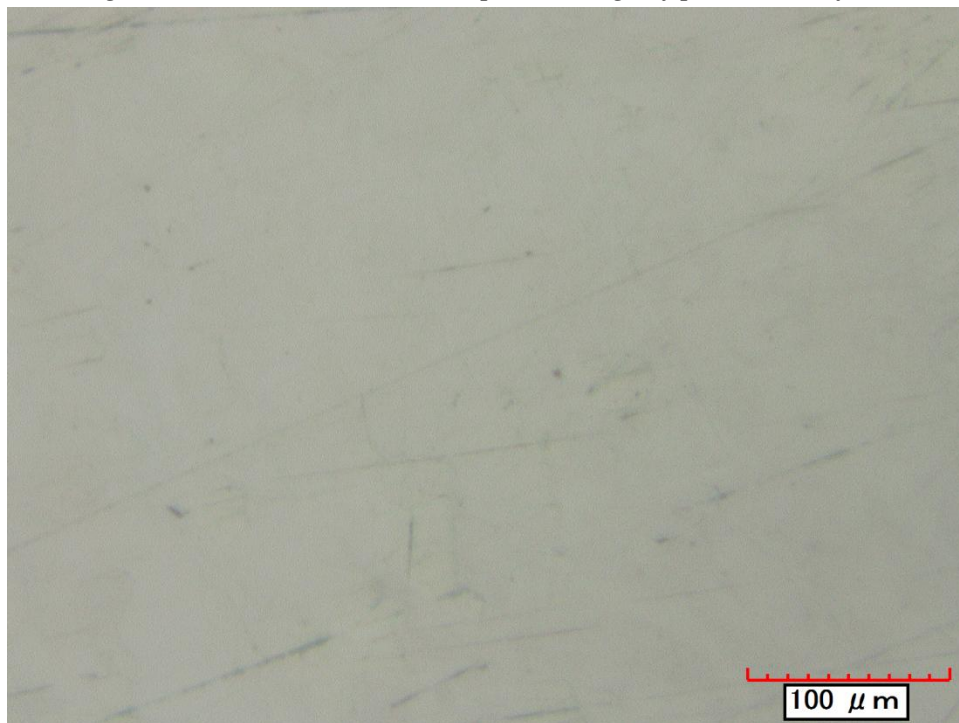


Figure 4.22 (above)- SPS 134 optical image of polished surface

Figure 4.23 (below)- SPS 145 optical image of polished surface



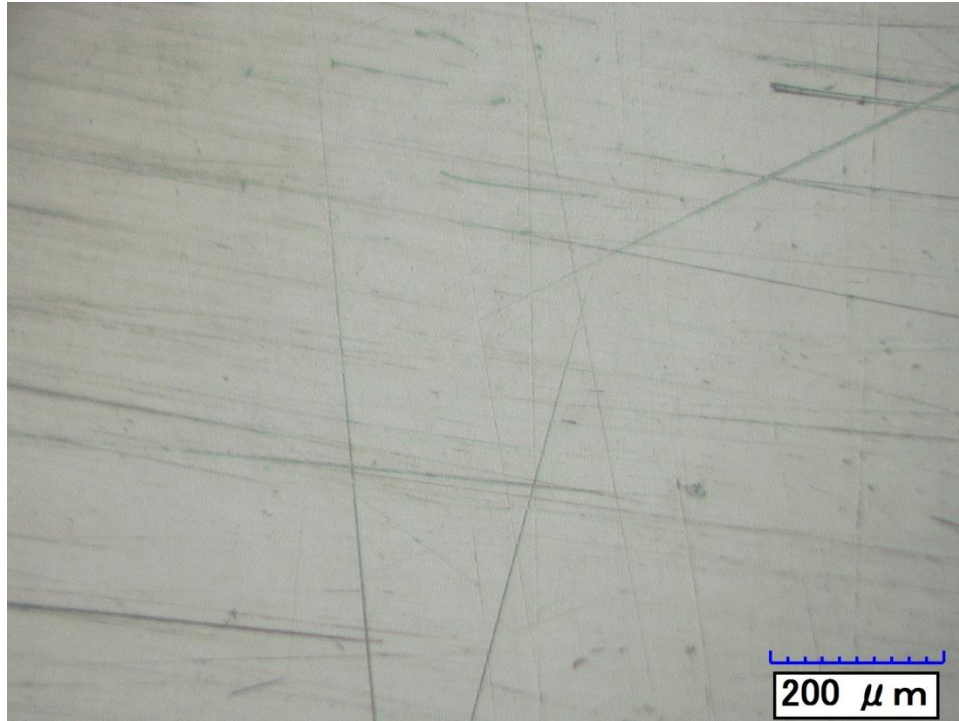


Figure 4.24 (above)- SPS 134 optical image of polished surface

Figure 4.25 (below)- SPS 145 optical image of polished surface



Table 4.4- Select Ni₄₅Co₁₀Ta₂₅Nb₂₀ SPS procedures and experimental results

System	SPS 44	SPS 102	SPS 106	SPS 134
Powders	60% 70-150 μ m 40% <53 μ m	14h BM pwd	10% 70-150 μ m 90% 14 hr BM	40% 70-150 μ m 30% <53 μ m 30% <53 μ m annealed
Dwell Temperature	680C	690C	690C	675C
SPS Pressure	575 MPa	1000 MPa	1000 MPa	1000 MPa
Density	11.00 g/cc	9.33 g/cc	10.42 g/cc	11.20 g/cc
Relative Density	99.0%	99.9%	99.5%	99.1%
Hardness	13.1	13.71	13.85	12.6

In a desire to verify the cause of the high compaction coupled with retention of amorphous nature additional tests were performed on NiCoTa(Nb) systems utilizing distinct methods. When only <53 micron powder were used crystallization occurred under SPS dwell temperatures of as low as 630C. The compaction obtained through the use of highly filtered fine powders remained high, nearly 100%, but at the cost of far more rapid crystallization in the SPS system. To attempt to counter this a Ni₄₅Co₁₀Ta₂₅Nb₂₀ powder set of exclusively sub-53 micron grains was sintered at a dwell temperature of 575C for 10 minutes under 1000 MPa of uniaxial pressure. This yielded a system with relative density of 85.0% at 9.60 g/cc with an XRD of the sample (SPS 150) and 2 hour ball milled ribbons shown in Figure 4.26 on the following page. While retaining the amorphous structure of ribbons and powders the low compaction and dramatically reduced hardness at 7.2 GPa render the sintering below the first DTA crystallization peak non-viable.

When similar methods were applied on Ni₄₅Co₂₀Ta₃₅ ribbons retaining the same powder ratios as SPS 134 mixing larger and smaller powders with small annealed powders crystallization occurred as low as 620C, near the first crystallization peak on the Differential Thermal Analysis results. In order to create compact and dense systems temperatures above the first crystallization peak had to be used, despite potential crystallization risks.

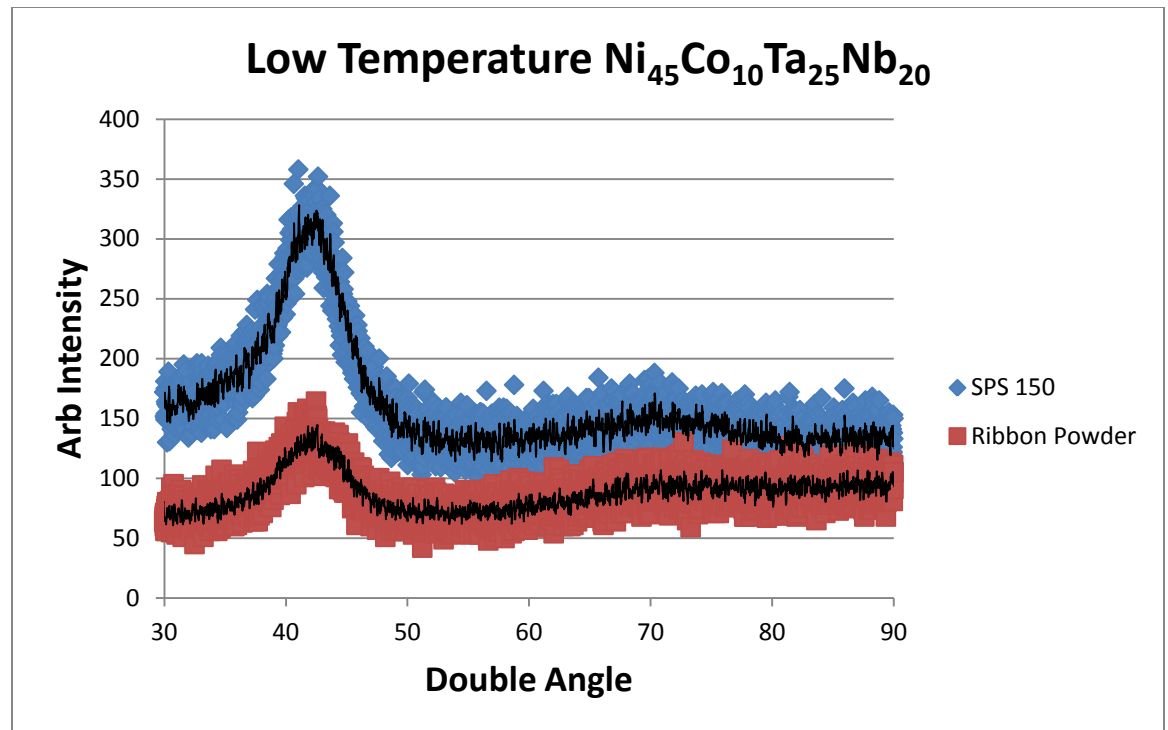


Figure 4.26-XRD on Ni₄₅Co₁₀Ta₂₅Nb₂₀ powders sintered at 575C for 10 minutes.

It is through these tests that the influence of the mixture and size of the powders is demonstrated as a highly influential factor in the crystallization rate of micro and nano sized powders under Spark Plasma Sintering compaction. It is a topic of contention as to the direct cause of the crystallization but current theories are in the current pathway optimization linked with surface area ratios of smaller powders yielding more rapid crystallization due to localized higher energy regions. As the current flows along the surface of the smaller powders higher fractions of the system are subject to high energy conditions allowing for nano-crystallization to occur despite the system temperature remaining far below the crystallization temperature and short exposure time. Due to this the desire for a mixture of large and small particles yielding high disorder is demonstrated through the retention of the XRD amorphous nature and high compaction of highly mixed systems. It is theorized that pure amorphous systems may be created for NiCoTaNb systems with extreme compaction if a reliable method of creating 10-20 μm amorphous powders existed without the contamination risk of ball milling.

To demonstrate the influence of powder size and pressure applied during sintering a combined plot of relative densities for iso-pressure and iso-ratio systems is shown in Figure 4.27. For the iso-pressure (575 MPa) the investigation was done using different ratios of large (greater than 74 micron) and small (below 53 micron) powders. For iso-powder ratio the pressure was varied from 60 MPa to 1000 MPa maintaining a powder ratio of 60-40 percent by mass of large (greater than 74 micron) to small (sub 53 micron) powders. Optimized radii ratio of 60 percent larger than 74 micron and 40 percent smaller than 53 microns was used in later runs when possible, though limited compaction problems were encountered within the $\pm 10\%$ powder radii ratio by mass from the 50-50 ratio. Pressure influence on compaction was clearly demonstrated through comparisons of 575 and 1000 MPa sintering on identical powder radii ratios and system sizes.

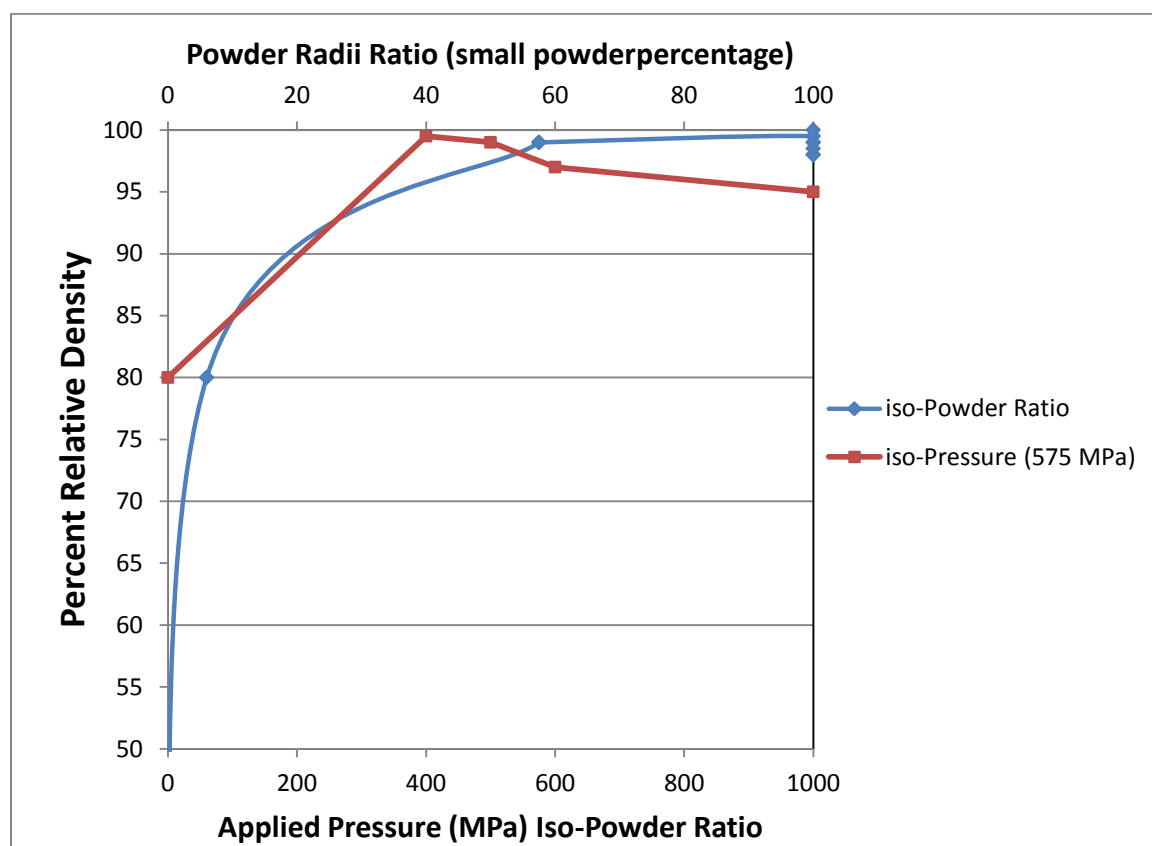


Figure 4.27-Percent relative densities of $Ni_{45}Co_{10}Ta_{25}Nb_{20}$ spark plasma sintered systems for iso-pressure and iso-ratio configurations

At this point SPS 134 and 133 demonstrate the highest combined reproducible compaction, hardness, and density achieved in a system while retaining the amorphous structure. While other systems may achieve higher compaction, hardness, or density no other systems demonstrated optimal results in all desired fields. At this time the optimal BMG systems retaining the amorphous structure maintain a Weibull statistical analysis hardness of 12.6 GPa with a modulus of 35.7 and a density of 11.20 g/cc. A large fraction (in excess of 50%) of the indents created during hardness testing demonstrated shear banding. This suggests that the material remained fairly ductile during compaction. These systems have been reproduced multiple times to demonstrate reliability in creation as well as increased size with cylinders in excess of 5 mm in height and 63.5 mm² in area retaining compaction and amorphous structure.

4.4 Bulk Metallic Glass experimental summary

- Tungsten based amorphous systems when created through powder metallurgy often risk contamination during the ball milling process. This results in non-reproducible systems that often have undesirable chemistry or suboptimal physical properties.
- Powder metallurgy, while viable in creation of certain amorphous systems, often masks multiple phase transformations or highly unstable systems that may be easily crystallized under Spark Plasma Sintering
- Hybridization of rapid quenching through melt spinning and powder metallurgy through milling yields small amorphous powders that may retain the amorphous nature even when rapidly sintered above the crystallization temperature
- Spark Plasma Sintering is a viable pathway for rapid compaction and creation of amorphous bulk metallic systems even when above the crystallization temperature due to ability to finely control Time-Temperature-Transformation window.
- Ni₄₅Co₁₀Ta₂₅Nb₂₀ systems may be compacted to nearly 100% compaction at temperatures in excess of first crystallization peak using Spark Plasma Sintering

due to manipulation of particle size and current flow distribution during compaction process.

- Ability to create highly compact, dense, hard, and semi-ductile bulk amorphous glasses is demonstrated with both reliability and reproducibility when proper sintering conditions and powder properties are selected and maintained.

References

1. Klement, W., Willens, R., & Duwez, P. (1960). Non-crystalline Structure in Solidified Gold–Silicon Alloys. *Nature*, 869-870.
2. Sheng, H., Luo, W., Alamgir, F., Bai, J., & Ma, E. (2006). Atomic packing and short-to-medium-range order in metallic glasses. *Nature*, 419-425.
3. "Crystal." *Wikipedia*. Wikimedia Foundation, 6 June 2014. Web. 26 June 2014. <<http://en.wikipedia.org/wiki/Crystal>>.
4. Schroers, J., & Johnson, W. L. (2004). Ductile bulk metallic glass. *Physical Review Letters*, 93(25), 255506.
5. Das, J., Tang, M. B., Kim, K. B., Theissmann, R., Baier, F., Wang, W. H., & Eckert, J. (2005). "Work-hardenable" ductile bulk metallic glass. *Physical review letters*, 94(20), 205501.
6. Li, Y., Poon, S. J., Shiflet, G. J., Xu, J., Kim, D. H., & Löffler, J. F. (2007). Formation of bulk metallic glasses and their composites. *MRS bulletin*, 32(08), 624-628.
7. Takeuchi, A., & Inoue, A. (2005). Classification of bulk metallic glasses by atomic size difference, heat of mixing and period of constituent elements and its application to characterization of the main alloying element. *Materials Transactions*, 46(12), 2817-2829.
8. Inoue, A., Wang, X. M., & Zhang, W. (2008). Developments and applications of bulk metallic glasses. *Rev. Adv. Mater. Sci*, 18, 1-9.
9. Telford, M. (2004). The case for bulk metallic glass. *Materials today*, 7(3), 36-43.
10. Ma, D., Stoica, A., Wang, X., Lu, Z., Clausen, B., & Brown, D. (2012). Elastic Moduli Inheritance and the Weakest Link in Bulk Metallic Glasses. *Physical Review Letters*.
11. Zhang, B., Wang, R., Zhao, D., Pan, M., & Wang, W. (2004). Properties of Ce-based bulk metallic glass-forming alloys. *Physical Review B*.
12. Wang, W. H. (2006). Correlations between elastic moduli and properties in bulk metallic glasses. *Journal of applied physics*, 99(9), 093506.
13. Wang, J. Q., Wang, W. H., & Bai, H. Y. (2011). Extended elastic model for flow in metallic glasses. *Journal of Non-Crystalline Solids*, 357(1), 223-226.

14. Johnson, W., & Samwer, K. (2005). A Universal Criterion for Plastic Yielding of Metallic Glasses with a $(T/T_g)^{2/3}$ Temperature Dependence. *Physical Review Letters*.
15. Voigt, W. (1889). Ueber die Beziehung zwischen den beiden Elasticitätsconstanten isotroper Körper. *Annalen der Physik*, 274(12), 573-587.
16. Reuss, A. (1929). Berechnung der Fließgrenze von Mischkristallen auf Grund der Plastizitätsbedingung für Einkristalle. *ZAMM-Journal of Applied Mathematics and Mechanics/Zeitschrift für Angewandte Mathematik und Mechanik*, 9(1), 49-58.
17. Hashin, Z., & Shtrikman, S. (1961). Note on a variational approach to the theory of composite elastic materials. *Journal of the Franklin Institute*, 271(4), 336-341.
18. "Kochmann Research Group - California Institute of Technology." *Kochmann Research Group - California Institute of Technology*. N.p., n.d. Web. 3 July 2014. <http://www.kochmann.caltech.edu/research_compositeE.html>.
19. Korringa, J. (1958). Dispersion theory for electrons in a random lattice with applications to the electronic structure of alloys. *Journal of Physics and Chemistry of Solids*, 7(2), 252-258.
20. Beeby, J. L. (1964). Electronic structure of alloys. *Physical Review*, 135(1A), A130.
21. Watson, K. M. (1957). Multiple scattering by quantum-mechanical systems. *Physical Review*, 105(4), 1388.
22. Berryman, J. G. (1980). Long-wavelength propagation in composite elastic media II. Ellipsoidal inclusions. *The Journal of the Acoustical Society of America*, 68(6), 1820-1831.
23. Kumar, A. P., & Baskaran, G. (1973). Coherent potential approximation, averaged T-matrix approximation and Lloyd's model. *Journal of Physics C: Solid State Physics*, 6(21), L399.
24. McLaughlin, R. (1977). A study of the differential scheme for composite materials. *International Journal of Engineering Science*, 237-244.
25. Schuh, C. A., Hufnagel, T. C., & Ramamurty, U. (2007). Mechanical behavior of amorphous alloys. *Acta Materialia*, 55(12), 4067-4109.

26. Künzi, H. U. (1983). Mechanical properties of metallic glasses. In *Glassy Metal II* (pp. 169-216). Springer Berlin Heidelberg.
27. Jovanovic, S., & Smith, C. (1961). Elastic Modulus of Amorphous Nickel Films. *J. Appl. Phys. Journal of Applied Physics*, 121-121.
28. Ashby, M., Nelson, A., & Centamore, R. (1970). The mechanical properties of a glassy metal; Ni₃P. *Scripta Metallurgica*, 715-717.
29. Masumoto, T., & Maddin, R. (1971). The mechanical properties of palladium 20 a/o silicon alloy quenched from the liquid state. *Acta Metallurgica*, 725-741.
30. Golding, B., Bagley, B., & Hsu, F. (1972). Soft Transverse Phonons in a Metallic Glass. *Phys. Rev. Lett. Physical Review Letters*, 68-70.
31. Chen, H. (1978). The influence of structural relaxation on the density and Young's modulus of metallic glasses. *J. Appl. Phys. Journal of Applied Physics*, 3289-3289.
32. Weaire, D., Ashby, M., Logan, J., & Weins, M. (1971). On the use of pair potentials to calculate the properties of amorphous metals. *Acta Metallurgica*, 779-788.
33. Kobayashi, S., Maeda, K., & Takeuchi, S. (1980). Computer simulation of deformation of amorphous Cu₅₇Zr₄₃. *Acta Metallurgica*, 1641-1652.
34. Knuyt, G., De Schepper, L., & Stals, L. M. (1986). Calculation of elastic constants for an amorphous metal and the influence of relaxation. *Journal of Physics F: Metal Physics*, 16(12), 1989.
35. Suzuki, Y., & Egami, T. (1985). Shear deformation of glassy metals: Breakdown of Cauchy relationship and anelasticity. *Journal of Non-Crystalline Solids*, 75(1), 361-366.
36. Teklu, A., Ledbetter, H., Kim, S., Boatner, L. A., McGuire, M., & Keppens, V. (2004). Single-crystal elastic constants of Fe-15Ni-15Cr alloy. *Metallurgical and Materials Transactions A*, 35(10), 3149-3154.
37. Lenkkeri, J. T. (1980). The elastic moduli of some body-centred cubic titanium-vanadium, vanadium-chromium and chromium-iron alloys. *Journal of Physics F: Metal Physics*, 10(4), 611.

38. Miracle, D. B., Sanders, W. S., & Senkov, O. N. (2003). The influence of efficient atomic packing on the constitution of metallic glasses. *Philosophical magazine*, 83(20), 2409-2428.
39. Yavari, A. R., & Inoue, A. (1998, January). Volume effects in bulk metallic glass formation. In *MRS Proceedings* (Vol. 554, p. 21). Cambridge University Press.
40. Miracle, D. B. (2006). The efficient cluster packing model—An atomic structural model for metallic glasses. *Acta materialia*, 54(16), 4317-4336.
41. Miracle, D. B. (2012). A physical model for metallic glass structures: an introduction and update. *JOM*, 64(7), 846-855.
42. Vaidyanathan, R., Dao, M., Ravichandran, G., & Suresh, S. (2001). Study of mechanical deformation in bulk metallic glass through instrumented indentation. *Acta Materialia*, 3781-3789.
43. Schuh, C. A., Hufnagel, T. C., & Ramamurty, U. (2007). Mechanical behavior of amorphous alloys. *Acta Materialia*, 55(12), 4067-4109.
44. Munir, Z. A., Anselmi-Tamburini, U., & Ohyanagi, M. (2006). The effect of electric field and pressure on the synthesis and consolidation of materials: a review of the spark plasma sintering method. *Journal of Materials Science*, 41(3), 763-777.
45. Garay, J. E. (2010). Current-activated, pressure-assisted densification of materials. *Annual review of materials research*, 40, 445-468.
46. Tokita, M. (1999). Mechanism of spark plasma sintering. In *Proceeding of NEDO International Symposium on Functionally Graded Materials* (Vol. 21, p. 22). Japan.
47. Xie, G., Zhang, W., Louzguine-Luzgin, D. V., Kimura, H., & Inoue, A. (2006). Fabrication of porous Zr–Cu–Al–Ni bulk metallic glass by spark plasma sintering process. *Scripta materialia*, 55(8), 687-690.
48. Shin, S., Song, M. S., & Kim, T. S. (2009). Synthesis of diamond-reinforced Zr 65 Al 10 Ni 10 Cu 15 metallic glass composites by pulsed current sintering. *Materials Science and Engineering: A*, 499(1), 525-528.

49. Abdellahi, M., & Bahmanpour, M. (2014). A novel technology for minimizing the synthesis time of nanostructured powders in planetary mills. *Materials Research*, (AHEAD), 0-0.
50. Okamoto, H. (2004). B-Fe (boron-iron). *Journal of Phase Equilibria and Diffusion*, 25(3), 297-298.

Appendix:

Appendix 1: Collection of experimental BMG data [10-13]

Composition	Shear Modulus G (GPa)	Bulk Modulus K (GPa)
Atomic fractions	Experimental	Experimental
Zr ₄₁ Ti ₁₄ Cu _{12.5} Ni ₁₀ Be _{22.5}	37.4	114.8
Zr _{46.75} Ti _{8.25} Cu _{7.5} Ni ₁₀ Be _{27.5}	35.2	113.4
Zr ₅₃ Ti ₅ Cu ₂₀ Ni ₁₂ Al ₁₀	32.1	106.8
Zr ₄₈ Nb ₈ Cu ₁₂ Be ₂₄ Fe ₈	35.2	113.4
Zr ₅₇ Nb ₅ Cu _{15.4} Ni _{12.6} Al ₁₀	32	107.7
Zr ₆₅ Al ₁₀ Ni ₁₀ Cu ₁₅	31	106.7
Zr ₅₀ Cu ₅₀	32	101.2
Zr ₄₈ Cu ₄₈ Al ₄	32.4	113.7
Zr ₄₅ Cu ₄₅ Al ₇ Gd ₃	32.4	117.1
Zr _{64.13} Cu _{15.75} Ni _{10.12} Al ₁₀	28.5	106.6
Zr _{61.88} Cu ₁₈ Ni _{10.12} Al ₁₀	29.1	108.3
Zr ₅₅ Al ₁₉ Co ₁₉ Cu ₇	30.8	114.9
Zr ₅₇ Ti ₅ Cu ₂₀ Ni ₈ Al ₁₀	30.1	99.2
Zr _{50.56} Ti _{5.14} Cu _{18.85} Ni _{11.14} Al _{14.3}	34	112.6
Cu ₆₄ Zr ₃₆	34	104.3
Cu ₅₀ Zr ₅₀	32	103
Cu ₄₈ Zr ₄₈ Al ₄	32.4	113.7
Cu _{47.5} Zr _{47.5} Al ₅	32.3	115.8
Cu ₄₇ Zr ₄₇ Al ₆	33.8	113.8
Cu ₄₆ Zr ₄₆ Al ₈	34.3	116.4
Cu ₄₅ Zr ₄₅ Al ₁₀	36.3	121.4
Zr _{46.25} Cu _{46.25} Al _{7.5}	34.3	116
Zr _{45.25} Cu _{46.25} Al _{7.5} Sn ₁	35.7	118
Zr ₅₉ Ta ₅ Cu ₁₈ Ni ₈ Al ₁₀	30.9	102

Appendix 1: Collection of experimental BMG data [10-13]		
Composition	Shear Modulus G (GPa)	Bulk Modulus K (GPa)
Zr ₄₁ Ti ₁₄ Cu _{12.5} Ni ₁₀ Be _{22.5}	35.9	111.2
Zr ₄₇ Ti _{12.9} Nb _{2.8} Cu ₁₁ Ni _{9.6} Be _{16.7}	32.6	-
Zr ₆₂ Cu _{15.5} Ni _{12.5} Al ₁₀	28.89	109.03
Zr ₆₁ Cu _{17.3} Ni _{12.8} Al _{7.9} Sn ₁	28.2	101.05
Zr ₅₇ Nb ₅ Cu _{15.4} Ni _{12.6} Al ₁₀	31.9	110.5107
Zr ₃₅ Ti ₃₀ Cu _{8.25} Be _{26.75}	31.8	108.3694
Zr ₅₀ Cu ₂₅ Be ₂₅	35.8	108.9761
Nd ₆₀ Al ₁₀ Fe ₂₀ Co ₁₀	19.4	46.5
La ₅₅ Al ₂₅ Cu ₁₀ Ni ₅ Co ₅	15.6	44.1
La ₆₆ Al ₁₄ Cu ₁₀ Ni ₁₀	13.4	34.9
Cu ₆₀ Zr ₂₀ Hf ₁₀ Ti ₁₀	36.9	128.2
Pr ₅₅ Al ₁₂ Fe ₃₀ Cu ₃	18.2	41.4
Mg ₆₅ Cu ₂₅ Tb ₁₀	19.6	44.7
Gd ₄₀ Y ₁₆ Al ₂₄ Co ₂₀	23.5	58
Dy ₄₆ Y ₁₀ Al ₂₄ Co ₁₈ Fe ₂	24.4	58.5
Nb ₅₀ Ni ₅₀	48.2	168.3
Ce ₆₈ Al ₁₀ Cu ₂₀ Fe ₂	11.8	31
Er ₅₀ Al ₂₄ Co ₂₀ Y ₆	27	65.1
Ca ₆₅ Mg _{8.54} Li _{9.96} Zn _{16.5}	8.9	20.1
Ca ₆₅ Mg _{8.31} Li _{9.69} Zn ₁₇	9	18.4
Yb _{62.5} Zn ₁₅ Mg _{17.5} Cu ₅	10.4	19.8
Ce ₇₀ Al ₁₀ Ni ₁₀ Cu ₁₀	13.5	27
La _{54.4} Ce _{13.6} Al ₁₀ Cu ₂₀ Co ₂	11.9	32.6
Ce ₆₈ Al ₁₀ Cu ₂₀ Nb ₂	11.7	31
Ce ₆₈ Al ₁₀ Cu ₂₀ Co ₂	11.8	30.3
Ce ₆₈ Al ₁₀ Cu ₂₀ Ni ₂	12	31.8
La ₆₀ Al ₂₀ Co ₂₀	14.5	39.2

Appendix 1: Collection of experimental BMG data [10-13]		
Composition	Shear Modulus G (GPa)	Bulk Modulus K (GPa)
Pr55Al25Co20	15.4	43.5
Dy55Al25Co20	23.5	52.2
Tb55Al25Co20	22.9	50.2
Ho55Al25Co20	25.4	58.8
Er55Al25Co20	27.1	60.7
Tm39Y16Al25Co20	29.7	66.1
Tm55Al25Co20	25.6	62
Lu39Y16Al25Co20	30	71.3
Lu45Y10Al25Co20	31.1	70.2
Lu55Al25Co20	30.6	69.2
Mg65Cu25Gd10	19.3	45.1
Mg65Cu25Y9Gd1	20.4	39
Mg65Cu25Y10	18.9	41.4
Mg65Cu25Y8Gd2	20.1	39.9
Mg65Cu25Y5Gd5	19.7	39.1
Ni45Ti20Zr25Al10	40.2	129.6
Ni50Co10Ta30Nb10	62	185
Mg65Cu25Gd10	19.3	45.1
Ce70Al10Ni10Cu10	11.5	27
La66Al14Cu10Ni10	13.44	34.91
Nd60Fe20Co10Al10	19.44	46.54
Ni40Cu5Ti17Zr28Al10	47.3	140.7
Ni40Cu5Ti16.5Zr28.5Al10	45.2	-
Ni45Ti20Zr25Al10	40.2	129.6
Ni40Cu6Ti16Zr28Al10	40.9	-
Cu60Zr20Hf10Ti10	36.9	128.2
Ti45Zr20Be35	35.7	111.8369

Appendix 1: Collection of experimental BMG data [10-13]		
Composition	Shear Modulus G (GPa)	Bulk Modulus K (GPa)
Ti45Zr20Be30Cr5	39.2	114.9867
Cu50Zr45Al5	33.3	-
Mg65Cu25Tb10	19.6	44.688
Gd36Y20Al24Co20	23.6	56.89612
Ho39Al25Co20Y16	26.2	63.52351
Fe65Mo14C15B6	73	195
(Fe90Co10)64.875Mo14C15B6Er0.125	73	178
(Fe90Co10)64.75Mo14C15B6Er0.25	73	175
(Fe90Co10)64.5Mo14C15B6Er0.5	73	175
(Fe90Co10)64.25Mo14C15B6Er0.75	73	176
(Fe90Co10)64Mo14C15B6Er1	73	177
Fe59Cr6Mo14C15B6	77.4	188
Fe50Cr15Mo14C15B6	82	204
Fe60.5Cr4Mo14C15B6Er.5	76.6	184
Fe63Mo14C15B6Er2	77.8	178
Fe55Cr8Mo14C15B6Er2	80	180
Fe48Cr15Mo14C15B6Er2	81	195
Fe63Mo14C15B6Er2	77	177
Fe63.5Mo14C15B6Er1.5	77	177
Fe64Mo14C15B6Er1	73.8	177
Fe64.25Mo14C15B6Er.75	73	178
Fe64.5Mo14C15B6Er.5	73.3	179
Fe64.75Mo14C15B6Er.25	73	179
Fe64.85Mo14C15B6Er.15	73	181
Fe66Mo10P12C10B2	66.1	176
Fe64Cr3Mo10P10C10B3	66	174
Fe63Cr2Mo10P12C10B2	65.3	178

Appendix 1: Collection of experimental BMG data [10-13]		
Composition	Shear Modulus G (GPa)	Bulk Modulus K (GPa)
Fe62Cr3Mo12P10C7B5	68.8	179
Fe65Cr2Mo12P10C8B6	66.8	174
Pd77.5Cu6Si16.5	34.8	174.7
Pd64Ni16P20	32.7	166
Pd40Cu40P20	33.2	158
Pd39Ni10Cu30P21	35.1	159.1
Pt57.5Cu14.7Ni5.3P22.5	33.3	198.7
Pd40Ni40P20	38.6	178.1538
Pd64Fe16P20	33.1	-
Pd80P20	27	-
Co56Ta9B35	91.5	216.469
W46Ru37B17	150	260

Appendix 2: Collection of experimental Crystalline System data [36-37]		
Composition	Shear Modulus G (GPa)	Bulk Modulus K (GPa)
Fe ₇₆ Cr ₁₂ Ni ₁₂	75.73	163.8
Fe ₇₀ Cr ₁₂ Ni ₁₈	75.89	186.2
Fe ₇₀ Cr ₁₅ Ni ₁₅	78.9	158.5
Fe ₇₄ Cr ₁₈ Ni ₈	77.15	158.3
Fe ₇₀ Cr ₁₈ Ni ₁₂	82.65	142.3
Fe ₇₀ Cr ₁₈ Ni ₁₂	78.48	168.4
Fe ₆₈ Cr ₁₈ Ni ₁₄	76.34	149.3
Fe ₆₃ Cr ₁₈ Ni ₁₉	76.66	143
Fe ₇₁ Cr ₁₉ Ni ₁₀	75.61	160.3
Fe ₇₁ Cr ₁₉ Ni ₁₀	77.55	157
Fe ₆₇ Cr ₁₉ Ni ₁₄	77.94	157
Fe ₆₂ Cr ₁₉ Ni ₁₉	77.16	156.7
Fe ₅₇ Cr ₁₉ Ni ₂₄	77.26	167.7
Ti _{42.2} V _{57.8}	34.37	129.35
Ti _{19.8} V _{80.2}	40.67	138.12
Cr _{89.2} Fe _{10.8}	105.04	193.59
Cr _{77.8} Fe _{22.2}	100.02	186.81